学位論文

Search for Axion-like Particles using Strong Pulsed Magnets at SPring-8

(SPring-8における強パルス磁石を用いたアクシオン様粒子の探索)

平成27年12月博士（理学）申請

東京大学大学院理学系研究科
物理学専攻
稲田　聡明

Abstract

This thesis reports the first X-ray light shining through a wall (LSW) search for axion-like particles (ALPs) using strong pulsed magnets. Using the LSW method, photons are converted to ALPs in magnetic field and then re-converted from the ALPs. The magnet system is a key technology in this search. A transportable magnet system for high-repetition use has dedicatedly been developed. The experiment has been carried out at the BL19LXU beamline of SPring-8, which produces the world's strongest X-ray beams. During two days of net run time, four magnets are operated at a mean peak field of 8.3 T and 5.7 T (the first and the second pulse, respectively) with a pulse repetition of about 0.2 Hz. After a total of 27,676 pulses, no signal events are observed. A new limit on ALP-two-photon coupling constant $g_{a\gamma\gamma}$ is obtained as

$$g_{a\gamma\gamma} < 2.51 \times 10^{-4}\ \mathrm{GeV}^{-1}$$

below$\sim$ 0.1 eV at 95% C.L. This is the most stringent LSW limit around 0.1 eV and rules out the possibility of ALP re-absorption in the Sun.

Contents

List of Figures

List of Tables

Chapter 1

Introduction

This thesis describes a search for axion-like particles (ALPs). ALPs have a similar property to that of axions. Axions are therefore introduced in the first place. Then ALPs and their history of search using LSW method is described. The motivation of the experiment is then presented. After that, features of the experiment are described. Among them, the use of pulsed magnets is a key technology, and they are introduced in the following section. Finally the structure of this thesis is described.

1.1 Axions

The axion is one of the best motivated particles. It was conceived to solve a long standing issue of the standard model, known as the "strong CP problem". This section briefly describes its origin and property.

1.1.1 Origin: the strong CP problem

In the QCD Lagrangian, there is an explicitly CP violating term,

$$L_\theta = \overline{\theta}\,\frac{g_s^2}{32\pi^2}\,G_a^{\mu\nu}\,\tilde{G}_{a\mu\nu}, \tag{1.1}$$

where g_s the strong coupling constant, $G^a_{\mu\nu}$ the gluon field strength tensor. and its dual of $\tilde{G}_{a\mu\nu} = \frac{1}{2}\,\epsilon_{\mu\nu\alpha\beta}\,G_a^{\alpha\beta}$. $\overline{\theta}$ is a CP violating parameter. There are no theoretical preference to it; it can take any value of 0–2π. It is therefore natural to expect it to be of order unity.

This parameter also gives neutrons a measurable value of its electric dipole moment d_n (nEDM). Experimentally, however, the nEDM is bounded to $|d_n| < 2.9 \times 10^{-26}$ e cm (90% C.L.) using polarized ultra-cold neutrons [1]. It corresponds to

$$\overline{\theta} = \frac{|d_n|}{5.2 \times 10^{-16}\ \text{e cm}} < 5.6 \times 10^{-11}. \tag{1.2}$$

This difference from the expected value of $\sim$1 is referred to as the strong CP problem [2, 3].

$\overline{\theta}$ consists of two parameters,

$$\overline{\theta} = \theta + \arg\det M, \tag{1.3}$$

where θ an angle decided by the QCD vacuum and M the quark mass matrix accounting the weak interaction. Eq. (1.3) hence means that strong CP problem also requires a fine-tuning of more than 10^{10} for the two independent interactions of the strong and the weak force. A solution to this problem is therefore considered to expand the standard model naturally.

The simplest extension of the standard model, providing a solution to the problem was first given by R. Peccei and H. Quinn [4, 5]. They proposed an additional global chiral symmetry $\mathrm{U}(1)_{\mathrm{PQ}}$, which is spontaneously broken in the early universe. The breaking of $\mathrm{U}(1)_{\mathrm{PQ}}$ at the energy scale f_a generate a pseudo Nambu-Goldstone boson, the axion. To make the standard model Lagrangian invariant under $\mathrm{U}(1)_{\mathrm{PQ}}$ symmetry, the new axion field a gives an additional term to the Lagrangian,

$$L_a = -\frac{1}{2}\,\partial_\mu a\,\partial^\mu a \;+\; L_{\mathrm{int}} \;+\; \xi\,\frac{a}{f_a}\,\frac{g_s^2}{32\pi^2}\,G_a^{\mu\nu}\,\tilde{G}_{a\mu\nu}. \tag{1.4}$$

The first and the second term account the kinetic energy of axions and their interactions, respectively. The third term describes a coupling of axions and gluons. ξ is anomaly coefficient and a model dependent parameter. The third term also represents an effective potential for the axion field. Its minimum occurs at the vacuum expectation value $\langle a\rangle = -\overline{\theta}\,f_a/\xi$ and is written as

$$\left\langle \frac{\partial V_{\mathrm{eff}}}{\partial a} \right\rangle = -\frac{\xi}{f_a}\,\frac{g_s^2}{32\pi^2}\,\left\langle G_a^{\mu\nu}\,\tilde{G}_{a\mu\nu} \right\rangle \Big|_{\langle a\rangle = -\overline{\theta}\,f_a/\xi}. \tag{1.5}$$

Thus $\langle a\rangle$ dynamically cancels out the $\overline{\theta}$-term at the minimum and therefore provides a solution to the strong CP problem.

1.1.2 Property

The second expansion of V_{eff} around its minimum gives the axion a mass

$$m_a^2 = \left\langle \frac{\partial^2 V_{\mathrm{eff}}}{\partial a^2} \right\rangle = -\frac{\xi}{f_a}\,\frac{g_s^2}{32\pi^2}\,\frac{\partial}{\partial a}\,\left\langle G_a^{\mu\nu}\,\tilde{G}_{a\mu\nu} \right\rangle \Big|_{\langle a\rangle = -\overline{\theta}\,f_a/\xi}. \tag{1.6}$$

The mass is thus given by its gluon coupling. This calculation gives [6, 7]

$$m_a = \frac{m_\pi\,f_\pi}{f_a}\,\frac{\sqrt{z}}{1+z} = 6.3\ \mathrm{eV}\,\frac{10^6\ \mathrm{GeV}}{f_a}, \tag{1.7}$$

where m_π the pion mass, f_π its decay constant, and $z = m_u/m_d$ the quark mass ratio between u and d. The axion thus directly acquires its mass by mixing with π^0, which occurs with the gluon coupling.

The π^0-mixing then induces another coupling of the axion to two photons

$$L_{a\gamma\gamma} = -\frac{1}{4}\, g_{a\gamma\gamma}\, F_{\mu\nu}\, \tilde{F}^{\mu\nu}\, a = g_{a\gamma\gamma} \mathbf{E} \cdot \mathbf{B}\, a, \tag{1.8}$$

where $F_{\mu\nu}$ is the electromagnetic field strength tensor, $\tilde{F}^{\mu\nu}$ its dual, $\mathbf{E} \cdot \mathbf{B}$ the product of the electric and the magnetic field. $g_{a\gamma\gamma}$ is the axion-two-photon coupling constant and is written as

$$g_{a\gamma\gamma} = \frac{\alpha}{2\pi f_a}\, C_\gamma, \tag{1.9}$$

where α the fine structure constant. C_γ is a model dependent parameter is written as

$$C_\gamma = \left| \frac{E}{N} - \frac{2}{3}\, \frac{4+z}{1+z} \right| = \left| \frac{E}{N} - 1.95 \right|, \tag{1.10}$$

where E the electromagnetic anomaly and N the color anomaly.

1.1.3 Invisible axion model

Invisible axion models take f_a larger than the electroweak scale. The axion hence becomes lighter and interacts weakly with matter. There are two typical invisible axion models.

KSVZ model

The Kim-Shfman-Vainshtein-Zakharov (KSVZ) model [8, 9] postulates that no leptons carry PQ charge. The charge is instead assigned to an exotic heavy quark. The axion interacts with matter only through the gluon coupling and is therefore referred to as "hadronic axion". When the electric charge of this new quark is taken to be zero, the model gives $E/N = 0$.

DFSZ model

The Dine-Fischles-Srednicki-Zhitnitskii (DFSZ)) model [10, 11] postulates that electrons carry PQ charge. Since many grand unification theories (GUT) introduce this model, this model is referred to as a "GUT-embedded model". The model does not require any exotic quarks and takes $E/N = 8/3$.

The mass of the axion and its coupling to two photons are related by Eq. (1.7) and Eq. (1.9) and are shown in Fig. 1.1. The two solid lines are the bounds of the typical invisible models. As can be seen in Eq. (1.10), C_γ varies from its center value of 1.95. The value expresses a model independent contribution, which comes from the π^0-mixing. It is possible to cancel out C_γ by some artificial fine-tune of E/N, however, it is natural to take C_γ as order unity. Typical invisible models take C_γ as 0.07–7. This region is referred to as the "invisible band" and is also shown in the figure with broken lines.

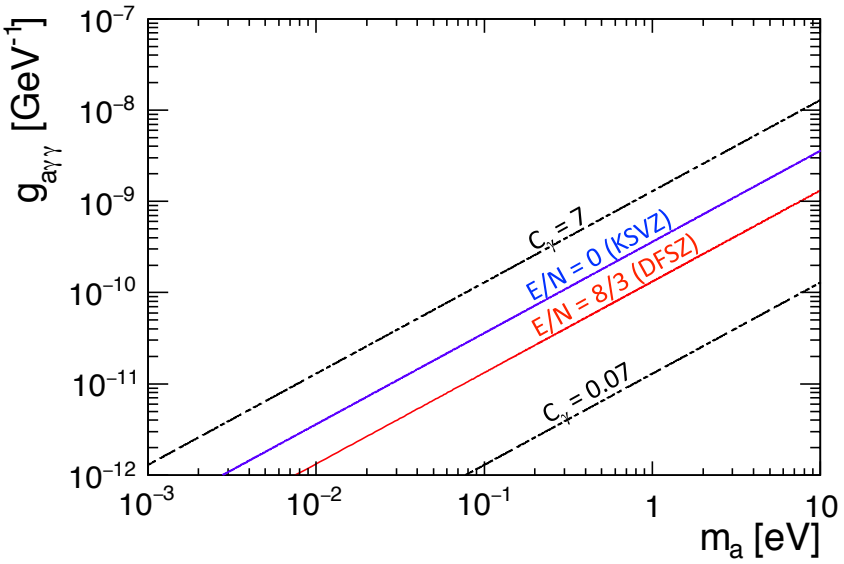

Figure 1.1: Bounds of invisible axion models between the axion-two-photon coupling constant and the axion mass. The blue line is standard KSVZ model ($E/N = 0$), and the red line is DFSZ model ($E/N = 8/3$). The broken lines show the region of typical invisible models with C_γ of 0.07–7, which is referred to as the "invisible band".

1.2 ALPs

Despite of its strong theoretical motivation, the axion has not been observed up to now. Therefore relatives of the axion have also intensively been searched in the mass-coupling plane other than the typical invisible band; the mass and the coupling are no longer bound. They are referred to as axion-like particles (ALPs). This section describes its origin and reviews the history of ALP search.

1.2.1 Origin

ALPs arise from a general consideration of the physics beyond the standard model. Most theories which go beyond the standard model have new symmetries, some of which are global. Any time such global symmetry is spontaneously broken, a Nambu-Goldstone or a pseudo Nambu-Goldstone boson appears. Corresponding scalar or pseudoscalar particles are referred to as ALPs. As examples of such general consideration, ALPs are predicted in supersymmetric theories [12], in string theory [13, 14], and in conformal standard model [15]. ALPs thus originally include both scalar and pseudoscalar cases, however, only the latter one is considered in this thesis.

Quite generally, the new particle couples to two photons. The coupling is written as the same expression of Eq. (1.8) for the pseudoscalar case. Some literatures

distinctively use $g_{A\gamma\gamma}$ as the ALP-two-photon coupling constant. Most of axion searches, however, are also sensitive to ALPs. Thus sometimes the same notation $g_{a\gamma\gamma}$ is also used for ALPs, and it is followed here. Their mass and their coupling to two photons are not related as it is in the case of the axion. They are hence searched in a plane of the two independent parameters.

1.2.2 Searching for ALPs

There are two methods to seach ALPs experimentally. Both apply the same mechanism. The last expression of Eq. (1.8) induces photon-ALP conversion in an external field. Here **E** is the incident photon field, and **B** is an external magnetic field. This conversion is referred to as the Primakoff effect. The inverse process also occurs and converts ALPs to outgoing photons in an external field. The two methods are distinguished whether the $\gamma \to a$ conversion takes place on the earth or not.

Astrophysical observations

Astrophysical observations have searched axions and ALPs from the Sun or in our galactic halo. Their techniques are referred to as helioscope or haloscope, respectively, both of which were proposed by *Sikivie* [16] in 1983. The helioscope technique is applied to detect solar axions or ALPs with masses below 0.1–1 eV [17, 18, 19, 20]. Crystal detectors are also used to search for solar axions and ALPs. The $a \to \gamma$ conversion occurs in the electric field of the crystal lattice with the Bragg condition [21, 22, 23, 24, 25] The haloscope technique is, on the other hand, applied to detect cold dark matter (CDM) axions or ALPs with masses around 1–10 μeV [26, 27, 28, 29].

Terrestrial experiments

Although a helioscope is not purely a laboratory experiment since they assume ALP flux from the Sun. There seems to be nothing wrong with it. After all solar neutrinos, which have also produced in the core of the Sun, are detected with its measured number consistent with the solar model, However it is desirable to have experiments in which both the production and the detection of ALPs are carried out on the earth. An experiment on this scheme was first proposed in 1982 [30] in the context of a search for hidden photons. It is now referred to as the "Light Shining through a Wall" (LSW) [31]. In the LSW experiment, a terrestrial *light* source is prepared, which is an alternative to the Sun or the galactic halo.

1.2.3 LSW experiment and its history

Principle

Here the principle of the LSW method is described (for detailed theoretical discussions, see Ref. [32, 33]). Figure 1.2 shows principle of the LSW experiment. A high-flux beam from a light source goes through an external field of a magnet. The region works as $\gamma \to a$ conversion region. Here only pseudoscalar particles are considered as ALPs. From Eq. (1.8) the external field needs to be parallel to the electric field, or polarization, of the photon. Most of the unconverted photons are dumped at a shield placed downstream of the magnet. Only ALPs pass through the shield due to their weak coupling to the matter. Behind the shield, the inverse process re-converts the ALPs to photons in the second field of another magnet. There is no energy loss in these conversions, and the regenerated photons have the same energy of the incident photons. Detection of ALPs is claimed whether the events of the regenerated photons surpass the background counts at a detector placed downstream of the second magnet.

The expected signal count N is expressed as [34]

$$N = \eta \, P_{a\to\gamma} \, P_{\gamma\to a} \, F \, t_{\rm tot}, \tag{1.11}$$

where η the detector efficiency, F the photon flux in time, and $t_{\rm tot}$ the total livetime of measurement. The probability of Primakoff conversion is written as

$$P_{a\to\gamma} = P_{\gamma\to a} = \left(\frac{g_{a\gamma\gamma}}{2}\right)^2 \frac{\omega}{\sqrt{\omega^2 - m_a^2}} \left| \int_0^L B(z) \, e^{iqz} \, dz \right|^2, \tag{1.12}$$

where ω the photon energy, $B(z)$ the field map along the beam direction of z, and L the field length. q is the momentum transfer to the magnetic field and is written as

$$q = \left| \frac{m_\gamma^2 - m_a^2}{2\omega} \right| \tag{1.13}$$

with the effective photon mass of

$$m_\gamma \simeq \sqrt{\frac{4\pi\alpha n_e}{m_e}} = 28.9\sqrt{\frac{Z}{A}\rho}, \tag{1.14}$$

where α the fine structure constant, n_e the number density of electrons in the gas, and m_e the electron mass. The second expression is more convenient for the calculation of m_γ with Z the atomic number of the gas, A its atomic mass, and ρ the gas density in g cm^{-3}.

The approximation of uniform field ($B(z) = B$) makes Eq. (1.12) to

$$\left(\frac{g_{a\gamma\gamma} BL}{2}\right)^2 \frac{\omega}{\sqrt{\omega^2 - m_a^2}} \left| \frac{\sin\frac{qL}{2}}{\frac{qL}{2}} \right|^2. \tag{1.15}$$

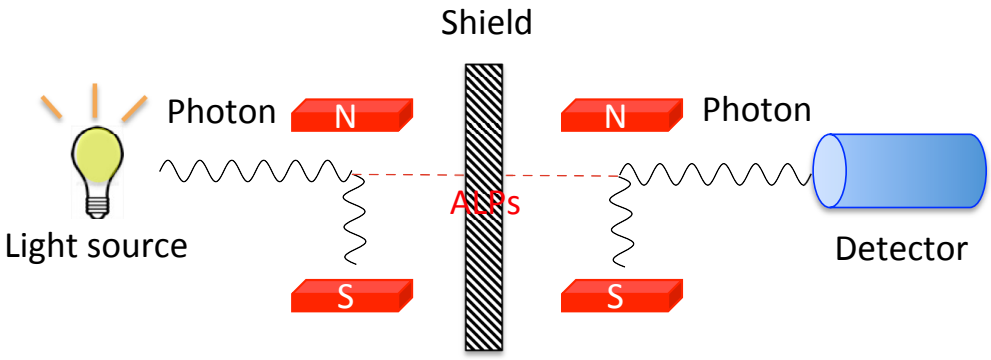

Figure 1.2: Principal of LSW search.

If q is small so that the oscillation length q^{-1} becomes sufficiently larger than L ($qL/2 \ll 1$), $\sin(qL/2)/(qL/2)$ becomes unity. In vacuum, where $m_\gamma \simeq 0$, this corresponds to a low mass region of m_a. As can be seen in Eq. (1.15), $g_{a\gamma\gamma}$ dependence on m_a vanishes for the mass region.

Parameter dependence of $g_{a\gamma\gamma}$ for the low mass region is summarized in Tab. 1.1. A major contribution comes from the performance of magnets, which is expressed as the product of their field and their length. The magnet needs to produce a transverse field along the polarization of the incident photon. This means that it is not useful to apply a conventional solenoid placed with its axis along the direction of the beam. Thus dipole magnets are typically used in LSW search. To obtain a larger field-length product, racetrack dipoles are usually selected.

Compared with its strong dependence on the magnet performance, $g_{a\gamma\gamma}$ weakly depends on the other parameters. These contributions are at most fourth root of the magnet performance. This feature comes from the fact that the LSW method uses the two Primakoff conversions on the earth; before and after the shield. The probability of each conversion is proportional to the square of $(g_{a\gamma\gamma}\, B\, L)$.

Parameter	$g_{a\gamma\gamma}$ dependence (factorial)
Magnets (field-length product)	-1
Photon flux	$-1/4$
Detector efficiency	$-1/4$
Background count rate	$+1/8$
Measurement time	$-1/8$ $(-1/4)$

Table 1.1: $g_{a\gamma\gamma}$ dependence on experimental parameters for the low ALP mass. The bracketed value of measurement time corresponds to the case of observing a null count.

History

The first LSW experiment to search for ALPs was proposed in 1985 [35, 36]. In early 1990s, this was realized by BFRT collaboration using an optical laser with a Fabry Perot cavity and superconducting dipoles of Brookhaven National Laboratory. Since then many experiments have been carried out to detect any signal of ALPs with every occasion of upgrades in the performance of optics or magnets. They are summarized in Tab. 1.2. All of them use a laser as their light source. Optical lasers can easily produce large photon flux by itself or using a Fabry Perot cavity. Pulsed lasers can also produce high intensity photons and are used in the experiments. In terms of magnets, which is the key factor of the LSW experiments, racetrack dipoles are typically used. They are commonly used as bending magnets in a circular accelerator. Due to the availability of spare or decommissioned magnets and the convenience of their transportation, most experiments have been carried out in the site of an accelerator. Their best limits are obtained by the ALPS and the OSQAR experiment using a HERA magnet at DESY [37] and two LHC magnets at CERN [38]. respectively. They now can be seen as two benchmarks of the LSW limits.

In addition to these optical searches, experiments with other light sources have recently been carried out to cover the wider range of the ALP mass. The first implementation of ALP search using a microwave cavity can be found in Ref. [39]. Another pioneering search using X-ray beams is performed by *Battesti et al.* [40] as the BMV project. They used 50.2 keV and 90.7 keV X-ray beams of synchrotron radiation at ESRF (European Synchrotron Radiation Facility). These energies are more than 10^4 higher than the energy of the previous laser experiments. Their limit on $g_{a\gamma\gamma}$ has thus extended the previous limits to higher mass region, and is shown in Fig. 1.3.

Experiment	Site	Year	ω [eV]	β	F [photon/s]	B [T]	L [m]
BFRT	Brookhaven	1992 [41], 1993 [42]	2.5	100	7.6×10^{20}	3.7	4.4
BMV	LULI	2007 [43], 2008 [44]	1.2	1	8×10^{21} (14 shots)	12.3	0.4
GammeV	Fermilab	2008 [45]	2.3	1	4×10^{17} (3600 shots)	5	3
LIPSS	JLab	2008 [46], 2009 [47]	1.0	1	1.1×10^{21}	1.7	1
ALPS	DESY	2009 [48], 2010 [37]	2.3	300	3.2×10^{21}	5	4.2
OSQAR	CERN	2008 [49], 2015 [38]	2.3	1	5.0×10^{19}	9	14.3

Table 1.2: Previous laser-LSW experiments, where ω the photon energy, β the building-up factor of a Fabry Perot cavity, F the photon flux taking β into account, B the field, and L its length of one side. The number in the bracket shows the total shots of a pulsed light source.

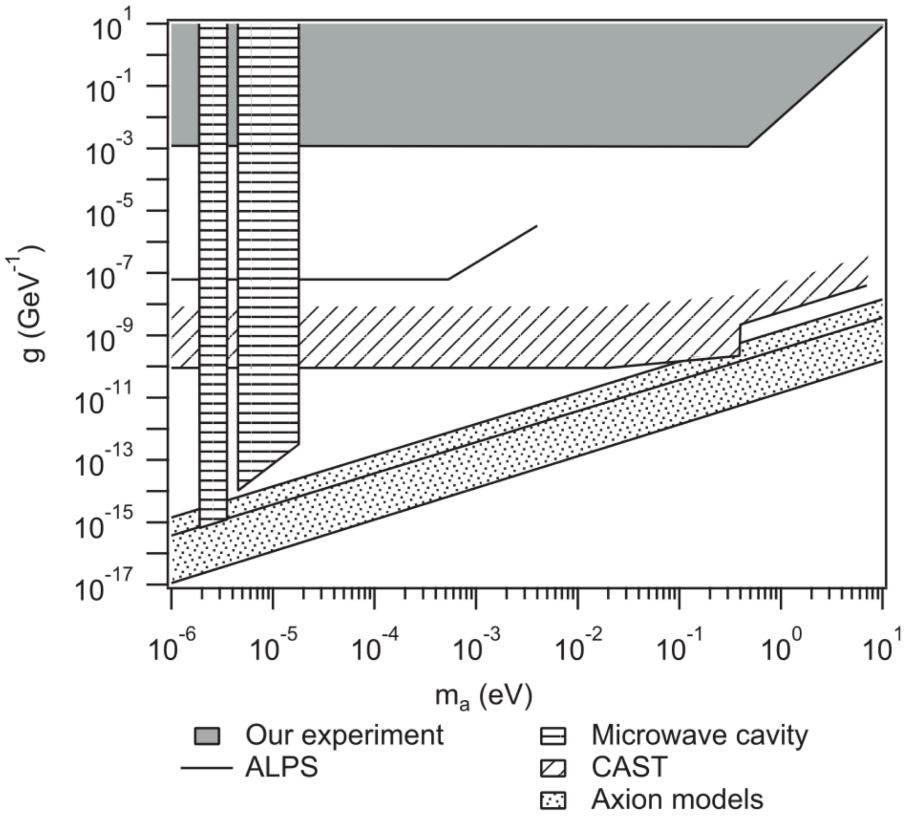

Figure 1.3: Limits on the ALPtwo-photon coupling constant as a function of the particle mass obtained by experimental searches (the figure is from Ref. [40]). In the legend, "Our experiment" is the previous X-ray LSW search at ESRF [40], "ALPS" is a laser LSW search at DESY [37], "Microwave cavity" is searches for cold dark matter axions [26, 27, 28, 29], "CAST" is a search for solar axions [20], and "Axion models" are described in Sec. 1.1.3.

1.3 Motivation of the terrestrial ALP search

This experiment is the second LSW search carried out at a synchrotron radiation facility. Using the world's strongest X-ray beams and multiple pulsed magnets with a racetrack shape provides a better sensitivity for the ALP mass region below $\sim 10^{-1}$ eV. Figure 1.3 [40] shows previous limits on $g_{a\gamma\gamma}$ as a function of m_a. X-ray source is suited to search for this mass region. This region also corresponds to an extremely-higher mass region of the laser-LSW limits, where dumping oscillation of the limit dominates. Therefore the result obtained by X-ray experiments is also considered to have significant information around 10^{-2} eV.

This section describes the motivation for the ALP search. First, motivations which are common to all ALP searches are described. Then a couple of interests

which are peculiar to X-ray terrestrial experiments are pointed out.

1.3.1 General motivations

Since the mass and the coupling of ALPs are not bound to the invisible band, they can be applied to explain long standing puzzles of cosmology and astrophysics. For example, they might become alternative candidates for dark matter [50, 51], explain the universe transparency to very high energy photons (>100 GeV) [52], the anomalous white dwarf cooling [53], or the recent excess of a 3.6 keV line from galaxy clusters [54]. These are the common motivations of all the terrestrial or extraterrestrial ALP searches. They push experiments to an unsearched parameter space in the mass-coupling plane.

There is also one remark that it is better not to stick too much to the mass relation of Eq. (1.7). As pointed out in many literatures [55, 56, 57], it could no longer be valid even in an axion model where the axion mass has other exotic contributions, such as gravity.

1.3.2 Interests of X-ray terrestrial experiments

Another X-ray search other than astrophysical observations

In the ALP mass-coupling plane, there are stringent bounds obtained by the astrophysical observations [17, 18, 19]. There have been so much arguments about the possibility of evading these astrophysical bounds. Most of them postulate some models and new physics at low energies [58, 59, 60, 61, 62]. Some of them were, however, conceived to evade the contrary between these bounds and the PVLAS result [63]. The PVLAS result was ruled out later on by other LSW experiments and its signal was found to be an artifact of the instruments.

Although evading these astrophysical bounds are not an easy task, it is clear that they inevitably have some model dependencies. Apart from those previous arguments, it seems to be desirable from the scientific point of view to have other X-ray searches using a different method. They are considered to have a good complementary relation with the astrophysical observations.

Possible solutions to some solar problems

The standard solar model seems to be reliable and agrees with helioseismological and neutrino observations. However there are still many problems with the Sun. One of them is the well-known "solar coronal heating problem"; the outer layer or the solar surface is hotter than its inner layer. As the world's consensus, this anomalous heat transportation is considered to be connected with solar magnetic activity.

Recently a striking possibility is pointed out by *Zioutas et al.* [64] proposing an ALP with its mass of 10–20 meV. A rapid change of the solar plasma density in its radial direction satisfies the resonance condition of $m_a = \omega_{\rm pl}$ ($\omega_{\rm pl}$ the plasma

frequency) at a depth of ∼400 km from its surface. The solar axions are re-converted to X rays with the resonance in the strong solar magnetism. The re-converted X rays go through down-comptonization and deposit their energy while propagating to the surface. If the ALP mass is taken as 10–20 meV, the $a \to \gamma$ conversion restores the coherence inside $\lesssim$400 km, and thus the anomalous heat transportation could become possible. Furthermore, this mechanism could also explain another problem with the Sun. Expected X-ray spectra reconstructed with this ALP contribution agree with the measured spectra.

In this case, the ALP flux from the Sun could become smaller and they could escape from the detection of the astrophysical observations. This intriguing scenario gives another interest to terrestrial X-ray searches.

Re-absorption in the Sun

Apart from the previous argument, which assumes some models and the ALP mass, re-absorption of the solar ALPs in the Sun was considered long time ago (see like [65]). This possibility seems to take place with a very strong ALP coupling to two photons of $g_{a\gamma\gamma} \sim 9 \times 10^{-4}$ GeV^{-1}. It is more than 10^7 times larger than the astrophysical bounds, and such a large $g_{a\gamma\gamma}$ is not preferred by considerations of the solar age and the helioseismology [66]. These observations and considerations are quite reliable, and therefore the possibility of the re-absorption has been naturally excluded.

On the other hand, one question still remains; has it been ruled out *experimentally*? The previous X-ray LSW search has not ruled out $g_{a\gamma\gamma} \sim 9 \times 10^{-4}$ GeV^{-1}, and strictly speaking, any terrestrial experiment has not excluded this extraordinary possibility yet. The reason is quite simple since there are only two powerful X-ray sources available to us. One is the Sun, and the other is synchrotron light. The experimental exclusion of this possibility is hence possible only by using a strong X-ray source and strong magnets.

The X-ray LSW experiment using synchrotron light was first proposed in 2006 [67, 68] and was realized in 2010 [40]. Although its photon flux is smaller than that of optical lasers, using X rays is one of the best way to increase the parameter space in the ALP mass-coupling plane. As described above, it also helps and compensates the astrophysical observations.

1.4 Features of the experiment

Significance of this experiment

In this thesis, another X-ray LSW experiment is described. An X-ray LSW experiment is carried out in a synchrotron radiation facility. As radiation control, setup of the experiment has to be contained in an experimental hutch, and human bodies are kept out from the hutch while the beam is on. A hutch typically has an

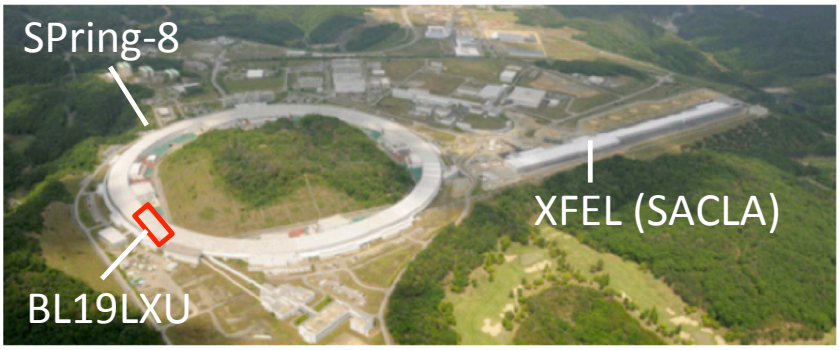

Figure 1.4: SPring-8 and SACLA

inner width of 3–4 m along the beam axis, and this restricts the space available to magnets. Large bending magnets used in previous LSW experiments are therefore not usable, and small magnets are required.

Recently, a new X-ray source, an Free Electron Laser (FEL), has become available. The world's second XFEL, SACLA (SPring-8 Angstrom Compact Free Electron Laser), has started its operation since 2013. It is located next to SPring-8 (Fig.1.4). It outputs pulsed X rays with one of the world's strongest peak intensities. If pulsed beam is used as light source of an LSW experiment, DC magnets are not necessarily required. Instead, strong pulsed-field which coincides with the X ray gives better sensitivity to $g_{a\gamma\gamma}$. This pulsed field is generated by a pulsed magnet. It has a typical size of 0.1–1 m and satisfies the restriction of hutch space. A long field is obtained by placing many magnets along the beam axis. In this thesis, combination of pulsed magnets and pulsed beam from SACLA is considered as the final goal of X-ray LSW experiments.

A typical beamtime assigned at SACLA is 2.5 days. This includes a time for setup and carry-out of the system from a hutch. They have to be minimized to obtain a sufficient time for measurement, Moreover, since SACLA is a new device, there are many applications of experiments, and obtaining a beamtime is highly competitive. Therefore, feasibility of the experiment has to be shown in advance to the one at SACLA. This demonstration is the theme of this thesis and is carried out using DC beam from SPring-8. Although DC beam gives a better sensitivity to $g_{a\gamma\gamma}$ when it is used with DC magnets, pulsed magnets are used with DC beam in this thesis for this demonstration. Nevertheless, this experiment has the best sensitivity ever to $g_{a\gamma\gamma}$ around 0.1 eV as an LSW experiment.

Features

The system used in this experiment has totally different features from the previous searches:

- strong pulsed magnets with:

  - unique design
  - high field efficiency
  - high repetition
  - high durability

- transportable capacitor bank with high repetition use
- the world's strongest DC X-ray beam from a long undulator
- the first LSW search using multiple magnets for each side of the shield

Among them, the pulsed magnets play a key role in the experiment. The use of pulsed magnets has not been decided from the beginning. In fact it has been taken about a year for the selection of the magnet. Careful investigations have been carried out for each possibility from water-cooling iron core dipoles to superconducting ones. Then a conclusion has been reached that only pulsed magnets have a potential of producing stronger field *by far* than that of magnets used in previous LSW searches. As an example, peak field of 85.8 T has been obtained by *Kindo et al.* [69] with simple structure of single solenoid.

On the other hand, length of the field is also an important factor. Previous searches used bending magnets of an accelerator with a length of ∼10 m. There are many proposals for the "next generation" LSW search [34, 70]. If the previous LSW searches are referred to as the first generation, the key feature of the second generation setup is to use multiple magnets to obtain the long field. As an example, 21 magnets of 5 T×8.8 m each are planned to be used in the ALPSII experiment [70] The total length of the setup is expected to be ∼200 m. Up to now, any LSW experiments have not used multiple magnets for each side of the shield to obtain a large length, though it is a key feature of the next generation LSW experiment. In this thesis, it is tried to demonstrate the use of multiple magnets for each side of the shield, which is the first great step toward the future LSW searches.

1.5 Pulsed magnets

1.5.1 Conventional magnets and banks

Pulsed magnets [71] are used to produce stronger field which cannot be obtained by DC magnets. They are divided into two categories. One is non-destructive magnets producing field below 100 T with pulse duration in the range of 1 ms–1 s. The other one produces field above 100 T with pulse duration of order microsecond due to self-destruction of its coil. The magnet concerned in this experiment is non-destructive type.

During the field generation, magnets are adiabatically heated up by strong pulsed current. The pulse width is determined by the inductance of a magnet and capacitance of a bank, which stores electric energy. To increase the heat capacity and reduce the resistance, magnets are cooled down with liquid nitrogen.

Figure 1.5: Left: A picture of a conventional pulsed magnet [72]. The inner coil is backuped with a maraging steel ring, and its outer diameter is typically ~200 mm. Right: a picture of a conventional capacitor bank of 500 kJ at SPring-8 BL19LXU.

Figure 1.5 shows pictures of a conventional pulsed magnet with solenoid structure and of a capacitor bank. High-density fluxes generated in the bore repulse with each other and cause outgoing pressure to the coil. This stress is referred to as the "Maxwell stress" and is proportional to the square of the field. It becomes 4 GPa at 100 T. The maximum field, or destruction field, is determined by the mechanical strength of the wire and the backup metal used to reinforce the bare coil.

The bank shown in the right picture is a typical capacitor bank of 500 kJ located outside of SPring-8 BL19LXU. Although most pulsed magnets are portable since they are not so large, a bank is generally fixed in a site of experiment or in a laboratory. This limits the possibility of using pulsed magnets in many experiments.

One of the key works is to make a transportable bank. If a field generation system is fixed, a light source must be portable to realize the LSW setup. This is one of main reasons why many previous searches have used a laser as a light source. On the other hand, if the field generation system becomes transportable, it widens the possibility of many experiments. In the case of LSW searches, it becomes possible to use various types of light sources, which are fixed in a facility or in a laboratory. As the first example, an LSW search using an X-ray source is demonstrated in this thesis.

1.5.2 Pulsed magnets with a long field region

The length of the field is another key factor of LSW searches. A unique design which produces transverse pulsed field over a long range can be found in Ref. [73]. This dipole magnet has a structure with two racetrack coils crossing at its body center. It produces peak field of 14 T with the body length of 480 mm.

1.6 Organization of the thesis

This thesis is organized as follows.

Chaper 2 describes the design and the study of the magnets in detail. The transportable capacitor bank is also explained there. Then the setup and devices used in the experiment is written in Chapter 3. In Chapter 4, data acquisition runs and the analysis are described. The results and future prospects are discussed in Chapter 5. Finally this thesis is concluded in Chapter 6.

Chapter 2

Magnets and bank

Magnets play a key role in LSW experiments. The largest contribution to the sensitivity on $g_{a\gamma\gamma}$ comes from the field-length product of the magnet. Strong and long fields are hence required to improve the sensitivity. To achieve this, pulsed magnets are selected from many other types of magnets. The magnets used in this search are dedicatedly developed for the X-ray LSW experiment.

In this chapter, definitions of words are shown in the first place. The design and the performance of the magnets are then described in detail. In order to provide pulsed current to the magnet, a capacitor bank is also needed. The rest of this chapter explains the design and the operation sequence of the bank. It is also dedicatedly developed along with the magnets.

2.1 Usage of words

First, usage of words from this chapter is mentioned:

- field: always means *magnetic* field, and also means *peak* field of a pulse except as otherwise noted. Moreover, it represents the field at the *center* of the magnet for the most cases.
- pulse: unit of a pulsed field with a shape of *half*-sinusoidal wave.
- shot: unit cycle of a bank operation; a shot contains one pulse in the "single pulse mode", whereas it contains *two* pulses in the "repetition mode".
- heat loss: energy loss of a shot, expressed in Joule
- heating: heat loss $\times$ shot repetition, expressed in W

2.2 Design of the magnets

2.2.1 Specification

Table 2.1 shows specification of the magnet. The coil is wound with a wire, which has a cross section of 1 mm×3 mm rectangle. Copper is selected as the material of the wire since it has a small resistance at a temperature of 77 K. The coil has a shape of single racetrack. The straight section of the racetrack has a length of 200 mm. The length is decided from the feasibility of coil winding. A beam pipe diagonally passes through the center of the magnet with an angle of 2.75°. A small diameter of the pipe contributes to the decrease of the field volume and thus increases the field efficiency characterized by field-current ratio. On the other hand, too small diameter requires a technique of precise alignment. A pipe with an outer diameter of 1/4 inch and a thickness of 0.5 mm is used for the beam path. Body length of the magnet becomes 350 mm after enclosing the coil with backup metals. Its weight is 16 kg. 15 turns of the wire gives its inductance and resistance of 40 μH and 23 mΩ, respectively at 750 Hz.

Parameter	Value
Wire	Cu (1 mm×3 mm)
Coil shape	single racetrack
Length of straight section	200 mm
Number of turns	15
Pipe	ϕ1/4 inch (=6.4 mm), t0.5 mm
Pipe tilting angle	2.75°
Body length	∼350 mm
Weight	16 kg
Resistance	9 mΩ @ DC
	23 mΩ @ 750 Hz
Inductance	40 μH @ 750 Hz

Table 2.1: Specification of the magnet

Development of magnets is a series of production and destruction. It has taken nearly two years to fix the design of the magnet suited to the high-repetition use. So far a total of about 30 magnets have been produced and tested. Although their design are not still completely optimized and are still on the way of optimization, seven magnets have been produced with the same structure for this experiment. The first produced magnet, referred to as magnet1, is used to test its durability for many shots before the experiment. Four of them, magnet2-magnet5, are used in the experiment. The rest two, magnet6 and magnet7, are reserved as spares in case of destruction.

2.2.2 Coil structure and the Maxwell stress

Figure 2.1 shows a schematic view of the magnet. It has a simple structure of single coil. X-ray beams diagonally pass through the center of the magnet. They are polarized along the horizontal direction. The magnet therefore stands at right angles so as to produce parallel field to the polarization of the X rays.

The reason of using the single-coil structure comes from the Maxwell stress. Some early prototypes have a typical dipole structure. In terms of field uniformity, the dipole structure is more preferred than the single-coil one. Moreover, racetrack dipoles are commonly used as bending magnets in a circular accelerator. Miniature version of such a magnet is thus easily conceivable from a sense of particle physics. There is however critical defect in this dipole structure. To improve the field efficiency, compactification of the field volume is necessary. The beam path, on the other hand, requires a sufficient diameter by taking into account the beam size and margin of arraignment. When the thickness of the support material is not enough, mechanical strength around the hole becomes weaker. The Maxwell stress causes an attracting force between the dipole coils. It acts as a collapsing force to the beam hole. As an example, one prototype has a hole diameter of 3 mm. Both the inner width of the coil and the distance between the poles are taken to be 4.5 mm. The hole has been collapsed with 9 T at the center of the magnet. The Maxwell stress scales to the square of the field. Field generation of, for example, 20 T hence requires more than 4 times larger mechanical strength. Thickness around the hole contributes to an increase of this strength. This however severely degrades the field efficiency. As a countermeasure, the single-coil structure is selected. This structure avoids the attracting force which appears in the dipole structure. In exchange, this structure has bad uniformity and symmetry due to the diagonal beam pipe crossing the center of the coil.

2.2.3 Eddy current and divided backups

Figure 2.2 shows pictures of the magnet. The top figure is the bare coil wound around a bobbin. The straight section of the coil has a length of 200 mm. Cu wire with cross section of 1 mm$\times$3 mm is used for the coil winding. The resistance of Cu becomes 1/8 when it is cooled with liquid nitrogen. Cu wire therefore has a good property of small heat loss. The wire is coated with a half-wrapped dielectric tape of polyimide. It is tightly wound around the GFRP (glass-fiber reinforced plastics) bobbin with 15 turns. The GFRP material is commonly used as a coil bobbin of a pulsed magnet. The bobbin has a diagonal hole with a crossing angle of 2.75°. The hole diameter is 1/4 inch (6.4 mm). A stainless-steel pipe with a thickness of 0.5 mm passes through the hole.

The bottom figure shows the fully backuped magnet. The bare coil is backuped with 20 divisions of stainless-steel metal. It is then compressed in the longitudinal direction by two thick plates with M20 bolts and nuts. The total body length is about 350 mm. Its weight is 16 kg.

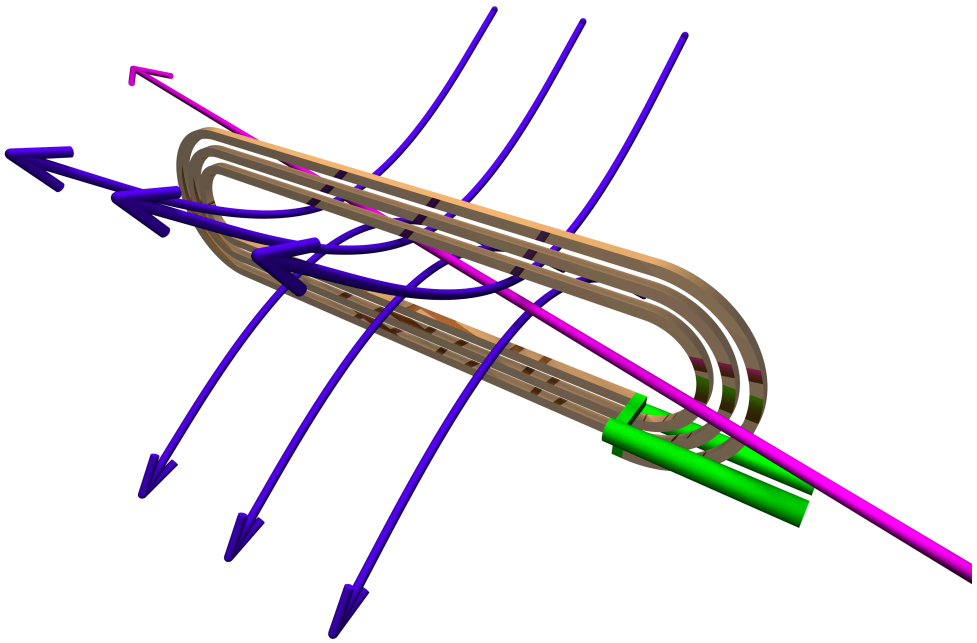

Figure 2.1: Schematic view of the magnet with simple structure of a single coil. X-ray beams diagonally pass through the center of the magnet. They are polarized along horizontal direction. The magnet therefore stands at right angles so as to produce parallel field to the polarization of the X rays.

The use of the divided backups comes from two reasons. One is eddy current which runs in the backup metal. For some early prototypes, a single backup which also has a racetrack shape and fits to the outer surface of the bare coil is used. The field efficiency of these magnets was measured to be significantly smaller by ∼15% than that without the backup. The reason has been found to be the cancellation of field by eddy current running in the backup metal. As a countermeasure, the backup is divided into pieces of metals. They are separated with each other using dielectric sheets to reduce the volume of a single metal. Figure 2.3 shows field efficiency along with the beam path calculated with 3D finite element simulation. The colored lines show the number of divisions: three (red), seven (blue), 19 (black) and 41 (magenta). Increasing the number of divisions clearly contributes to the decrease of the field cancellation from eddy current.

The second reason is the mechanical strength of the backup. The single backup of this prototype is deformed by expansion of the coil at ∼10 T due to the Maxwell stress. This deformation comes from the fact that straight section of the backup receives all of the coil expansion pressure. The resulting stress concentrates on the corner sections of the backup, which connect the straight and the round sections. This problem is also avoided by changing the single metal into pieces. The expansion pressure of the coil is distributed to each division. The local concentration of the whole stress thus does not occur.

2.3 Basic performance

This section describes basic performance of the magnet. The performance is characterized by the following items:

- field efficiency
- field map along the beam path
- heat loss
- thermal time constant
- leakage field
- destruction field
- repetition field

Before the description of each items, the way of measuring of the field and the current, which are common to all measurements, is explained. In the following measurements, capacitance of the bank is set to 1.5 mF except as otherwise noted.

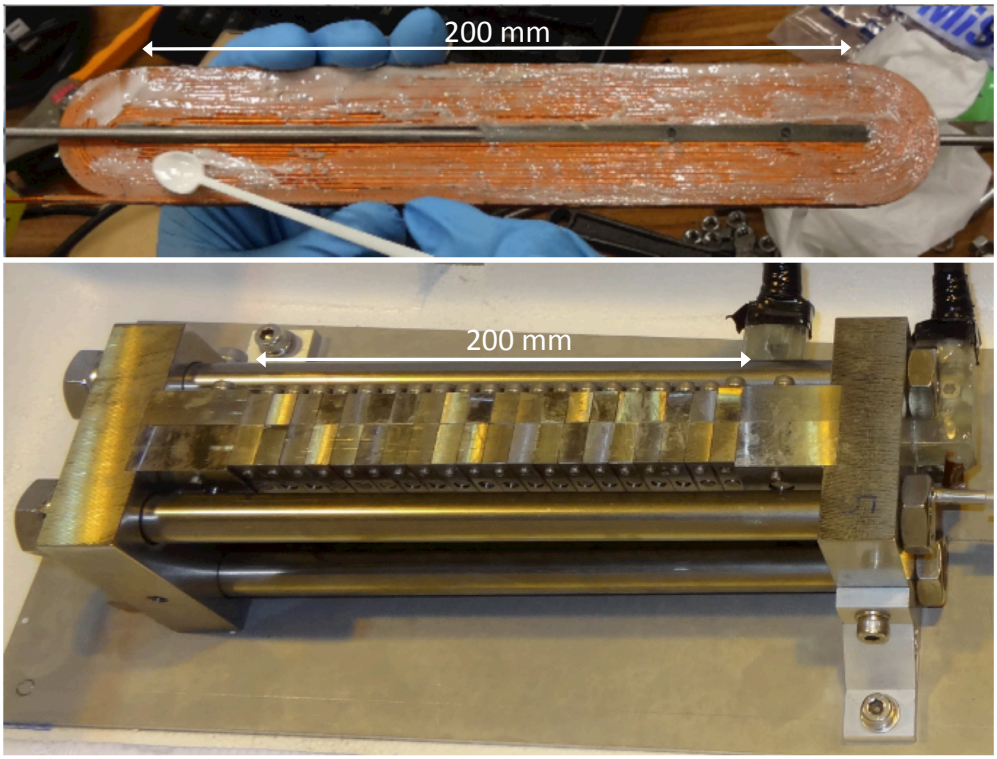

Figure 2.2: Pictures of the magnet. Top: a bare coil of Cu wire wound around a GFRP bobbin. Its straight section has a length of 200 mm. The beam pipe diagonally passes through the center of the coil. Bottom: the fully backuped magnet. The bare coil is backuped with 20 divisions of stainless-steel metal and is compressed in the longitudinal direction by two thick plates with M20 bolts and nuts.

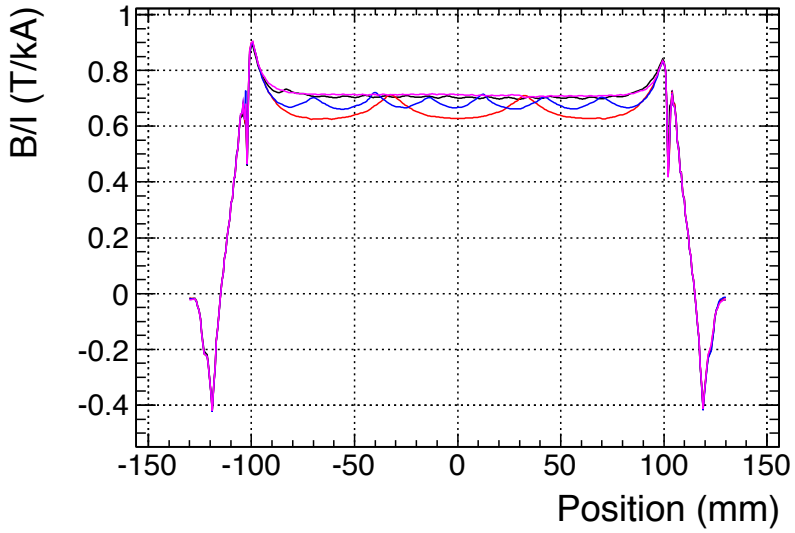

Figure 2.3: Field efficiency with divided backup along with the beam path calculated with 3D finite element simulation. The colored lines show the number of divisions: three (red), seven (blue), 19 (black) and 41 (magenta). The increase of the divisions clearly contributes to the decrease of the field cancellation from eddy current.

2.3.1 Measurement of the field and the current

Field

The field is measured with a pickup coil. Figure 2.4 shows a picture and a schematic view of the pickup coil. The field is measured by inserting the small coil along the beam path. The wire is made of Cu core (ϕ0.1 mm) coated with enamel (t150 μm) and is wound around a GFRP rod (ϕ1.5 mm) with five turns. The read line is twisted to cancel out an induced voltage from the field. In order to detect transverse field, its head is cut off and is glued at right angles to the rod.

The pickup coil is produced and calibrated with the following procedure. First, a coil before the cut-off, which is just wound around a rod, is calibrated using a solenoid pulsed magnet with a large bore diameter of $\sim$10 cm. The large-bore magnet is used due to its good uniformity of the field. The absolute value of the field generated in the magnet is obtained by using another well-calibrated pickup coil, a master coil, at the same time. Precise calibration of the master coil has been carried out by measuring field from spin-flip transition of an anti-ferromagnetism. In order to know the individual difference, two coils have been calibrated in the large-bore magnet with the mater coil. The difference is 0.6% and is relatively a good result for such a small structure This calibration procedure using the large-bore solenoid has been carried out at IMSL, Kashiwa.

After that, one of the calibrated small coils is cut off at its head and is glued at right angles to the previous rod. This picture is shown at the top of Fig. 2.4. Misalignment of the gluing angle gives a measured field reduced by a cosine factor. This means that if accuracy of the gluing is ten degrees, the field is conservatively measured to be less by only 1.5%.

To measure the field at the center of the pipe, the head of the pickup coil is embedded into a GFRP centering. The bottom of Fig. 2.4 shows its schematic view as well as its picture. Measured field changes with a rotation of the coil around its long GFRP rod. The rotation is therefore always adjusted to the angle, which maximize the measured field.

Current

Current is measured with a commercial current transformer (CT, Pearson Model 14239). Figure 2.5) shows its picture. It outputs a voltage proportional to the current passing through the hole. The input current and the output voltage are electrically isolated. Its sensitivity is 1 V/kA, and the maximum peak current is 500 kA. Cut-off frequencies are 1.0 Hz and 1.2 MHz. Its specification is summarized in Tab. 2.2.

Shapes of field and current

Figure 2.6 shows a typical shape of the field and of the current with a charged voltage of 2.75 kV. A raw signal of a pickup coil is the induced voltage of $\mathrm{d}\Phi/\mathrm{d}t$.

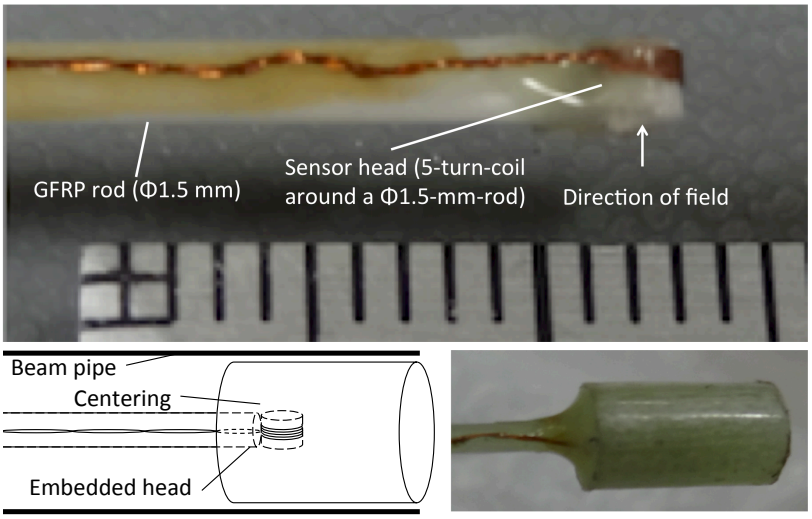

Figure 2.4: Pickup coil. Top: Cu wire (ϕ0.1 mm) coated with enamel (t150 μm) is wound around a GFRP rod (ϕ1.5 mm) with five turns. Bottom: a centering used to measure the field at the center of the pipe. The head of the pickup coil is embedded into the GFRP centering.

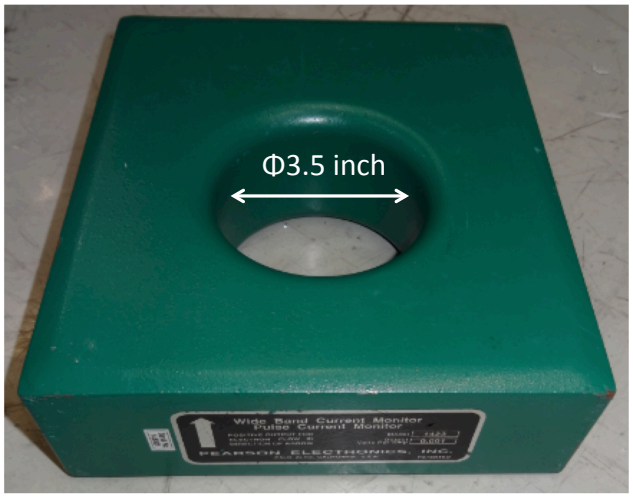

Figure 2.5: Current transformer (Pearson Model 14239). It outputs a voltage proportional to the current passing through the hole. The input current and the output voltage are electrically isolated.

Parameter	Value
Sensitivity	1 V/kA
Output resistance	50 Ω
Maximum peak current	500 kA
Maximum rms current	2.5 kA
Current-rise product	75 A·s
Low frequency 3 dB cut-off	1.0 Hz
High frequency 3 dB cut-off	1.2 MHz

Table 2.2: Specification of Pearson Model 1439

The field shape is obtained by integrating the the raw signal. Absolute value of the field is scaled with the calibration coefficient described above. Current shape is also measured with the CT and it agrees with the field shape. The current shape is a half sinusoidal pulse with its frequency determined by the LC resonance of the coil inductance L and the bank capacitance C. The frequency becomes about 750 Hz, which corresponds to a pulse width of 0.67 ms. If the two magnets are serially connected, the total inductance doubles, and the pulse width becomes about 1 ms.

2.3.2 Field efficiency

Field efficiency is expressed by field-current ratio. The peak values of the field and current are used for this ratio. Figure 2.7 shows measured field and the field-current ratio of four magnets at the center of their beam path. All the magnets reach around 9 T with a charged voltage of 2.75 kV. The red line shows a mean value of four measurements from 1.5 kV to 2.75 kV, which correspond to the field range of ∼5–9 T. This region covers the most of the field produced in the run (see Fig. 4.1). Note that during the run, $\sqrt{2}$-time-higher voltages around 3.5–4.00 kV are applied to two magnets, which are serially connected (Fig. 3.10). Their total inductance becomes twice as much as that of each. From the relation of $LI^2/2 = CV^2/2$, the measurements for single magnet in Fig. 2.7 provides the same range of current as the run. The field therefore reaches 9 T with a $\sqrt{2}$-time-smaller voltage than 3.5–4.00 kV. The mean values are used in the analysis in Chapter 4.

2.3.3 Field map

Field map is measured along the beam path. Figure 2.8 shows a schematic view of the measurement. The map is measured with both the position and the direction of the magnet unchanged. The field direction is shown with a black arrow. There are two directions to insert a pickup coil into the pipe. Here the the electrode side is defined as “back”, and the other as “front”. The beam direction is taken as z axis with its origin at the center of the magnet. The $z < 0$ region corresponds to the front side and $z > 0$ to the back side. When a positive field is detected by

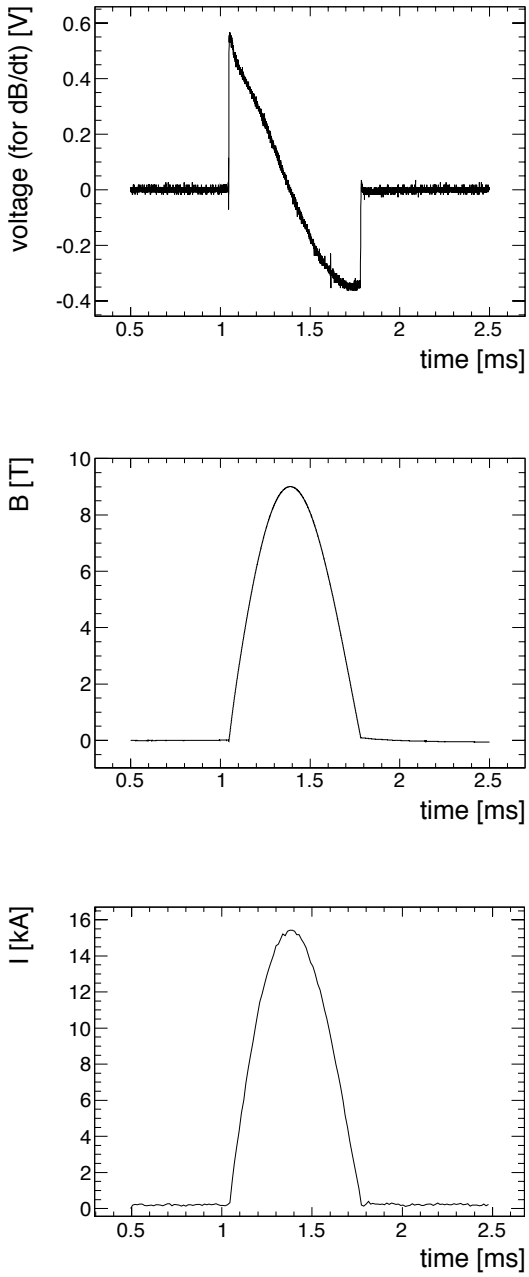

Figure 2.6: Typical shapes of the measured field and current with 2.75 kV. Top: a raw signal of the pickup coil, which is an induced voltage of $d\Phi/dt$. Middle: the field shape obtained by an integral of the raw signal. Bottom: the current shape measured with the CT.

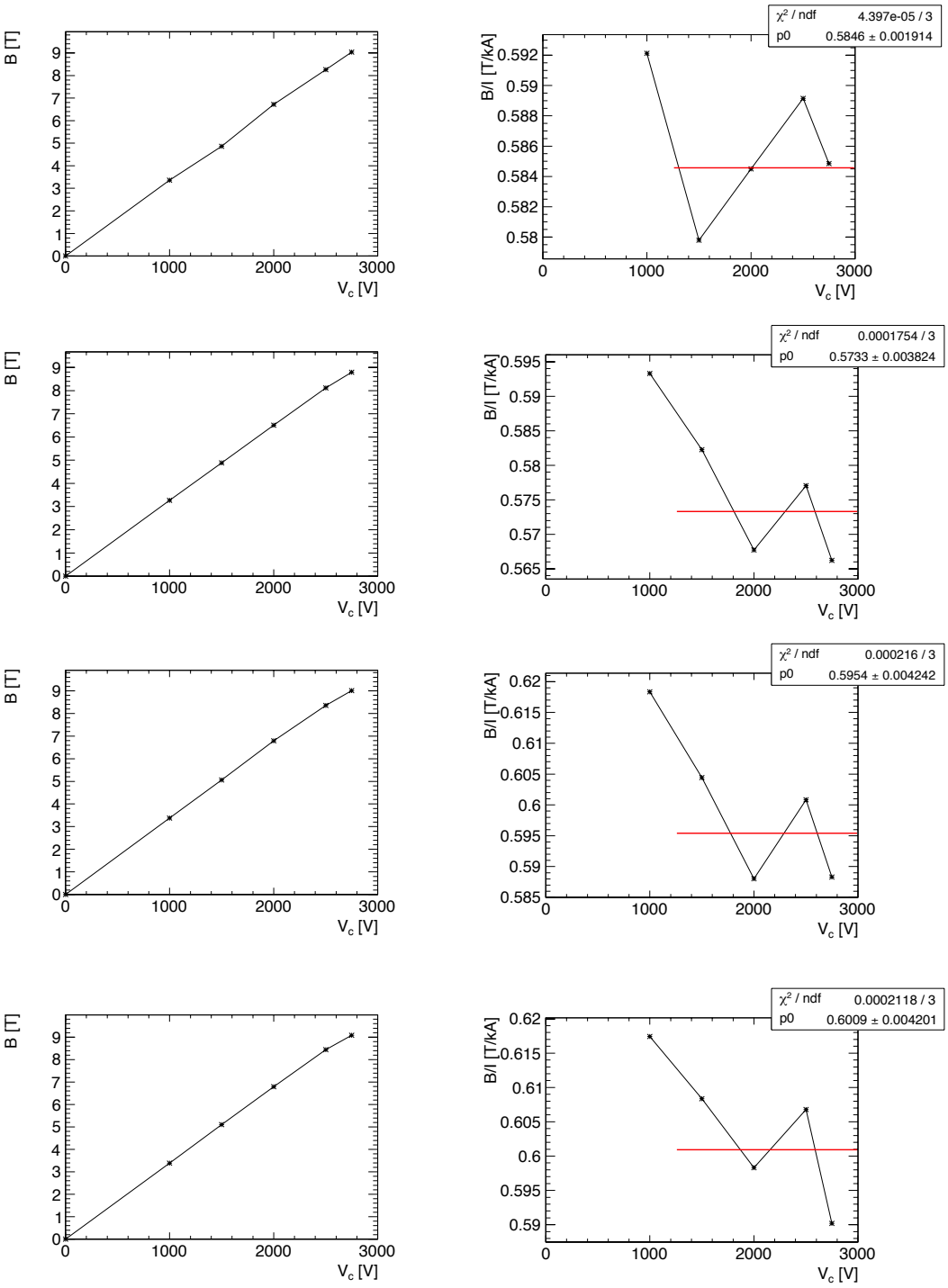

Figure 2.7: Field-current ratio of the four magnets. Left: the measured fields at the center of the magnets. Right: the measured field-current ratios.

the pickup coil, rotating it by 180° gives a negative field. Hence there are also two directions of the pickup coil, which is shown with a white arrow. The direction, which detects a positive field by inserting the coil from the front, is defined as "0°". Rotation of 180° from the 0°, which detect a negative field by inserting t from the front, is defined as "180°". There are thus four ways to measure the map.

Left of Fig. 2.9 shows a measured map with a charged voltage of 0.2 kV with different configurations. The black line shows back-0° data and the red one shows front-180° data. Their negative field is inversed for the visibility. The two measurements give the same deviation of the coil head from the center of the beam path, which may have occurred at gluing of the coil head to the GFRP rod (see Fig. 2.4). The blue data is the mean of the two measurements from the different directions. This mean cancels out the contribution from axial component of the field, which is not detected by an ideal pickup coil.

Right of Fig. 2.9 compares the difference between the pervious measurement of back-0° and front-180° (black), and the other measurement of back-180° and front-0° (red). Difference of the two measurements show two contributions. The first one is the deviation of the coil head from the center of the beam path (gluing). This gives the difference of the two maps so that its sign changes for $z > 0$ and $z < 0$ regions. Such an alternating difference is not seen in the figure and therefore the deviation of the coil head from the pipe center is considered to be negligibly small. The other contribution is an accuracy of the map measurement since they measure the same map with a different way. Its major difference comes from reproducibility of the rotation angle of the coil. This gives a uniformly lower map than the other. The observed difference is seem to be more likely for this case. The difference between the areas of the two maps is 0.9%. The result is taken as a systematic error, which is described again in the analysis.

Figure 2.10 shows a comparison of the measured map (the black line in the right of Fig.2.9) and the calculation of finite element simulation (ANSYS). The simulation includes all the 3D geometrical information. Unsmooth structure at the edges of the simulation reflects the finite size of the mesh. Although non-magnetic metal (stainless-steel 304) is used for the backup material, small magnetization appears at low temperature on its surface after the machining. This inhomogeneous distribution of permeability in the backup metal, which is not reproduced in the simulation, is considered to cause the difference from the measurement. The difference of the area between the two maps is 0.2%.

Figure 2.11 shows measured maps of the four magnet used in the experiment. Slight asymmetric structure can be seen in the figure; the half region of $z < 0$ is slightly small when compared with the other half region of $z > 0$. This feature comes from the fact that the coil structure is not symmetrical due to the existence of a pair of electrodes. They break the geometrical symmetry.

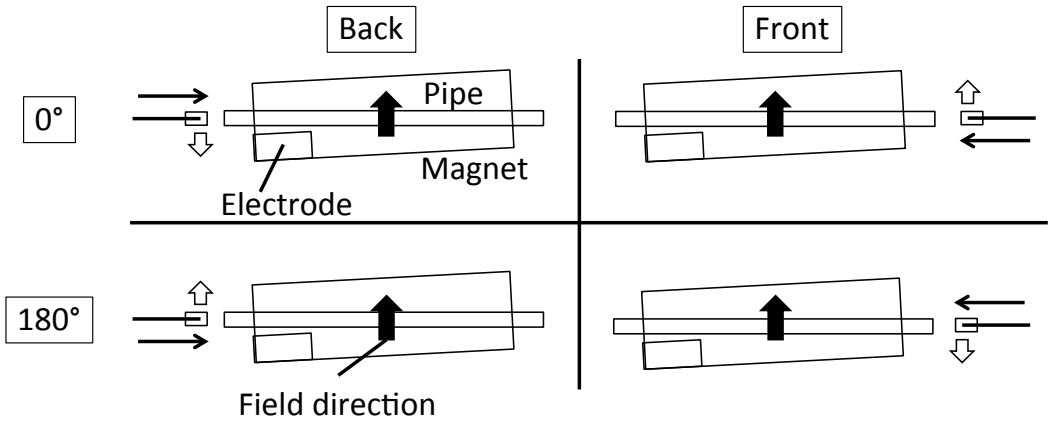

Figure 2.8: Configuration of the map measurement. The field direction of the magnet is shown with a black arrow. The direction of the pickup coil is shown with a white arrow. If the two arrows are in the same direction, a positive field is measured by the pickup coil. For the definition of "front" and "back", or "0°" and "180°", see the text.

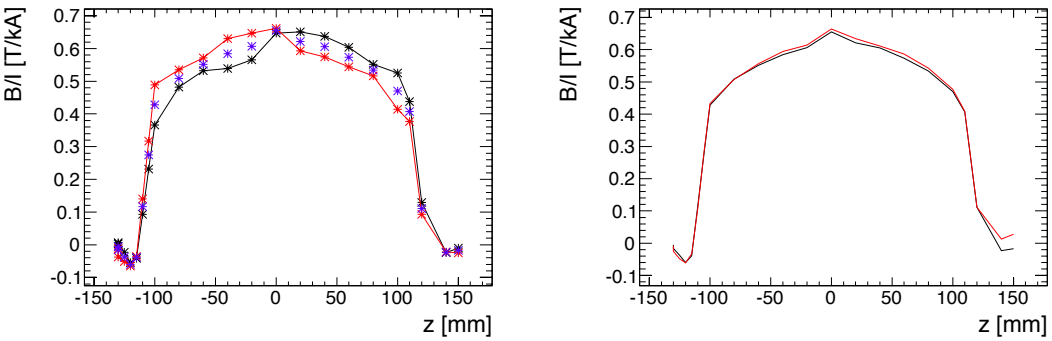

Figure 2.9: Measured map with a charged voltage of 0.2 kV with different configurations. Left: comparison of the back-0° data (black) and the front-180° data (red). Their negative field is inversed for the visibility. The blue points show the means of them. Right: comparison of the mean maps measured with the different configurations. The black line is the mean of back-0° and front-180° measurements, and the red line is the mean of back-180° and front-0° measurements.

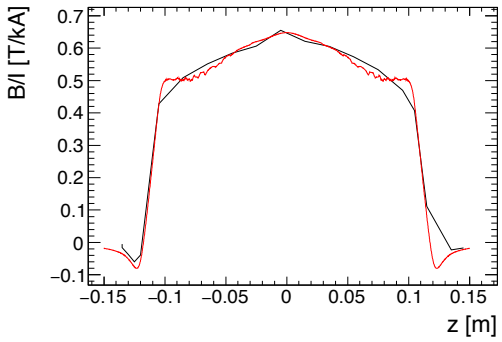

Figure 2.10: Comparison of the measured map (the black line in the right of Fig.2.9) and the calculation of finite element simulation (ANSYS). The simulation includes all the 3D geometrical information. Unsmooth structure at the edges of the simulation reflects the finite size of the mesh. Inhomogeneous distribution of permeability in the backup metal is considered to cause the difference from the measurement. The difference of the area between the two maps is 0.2%.

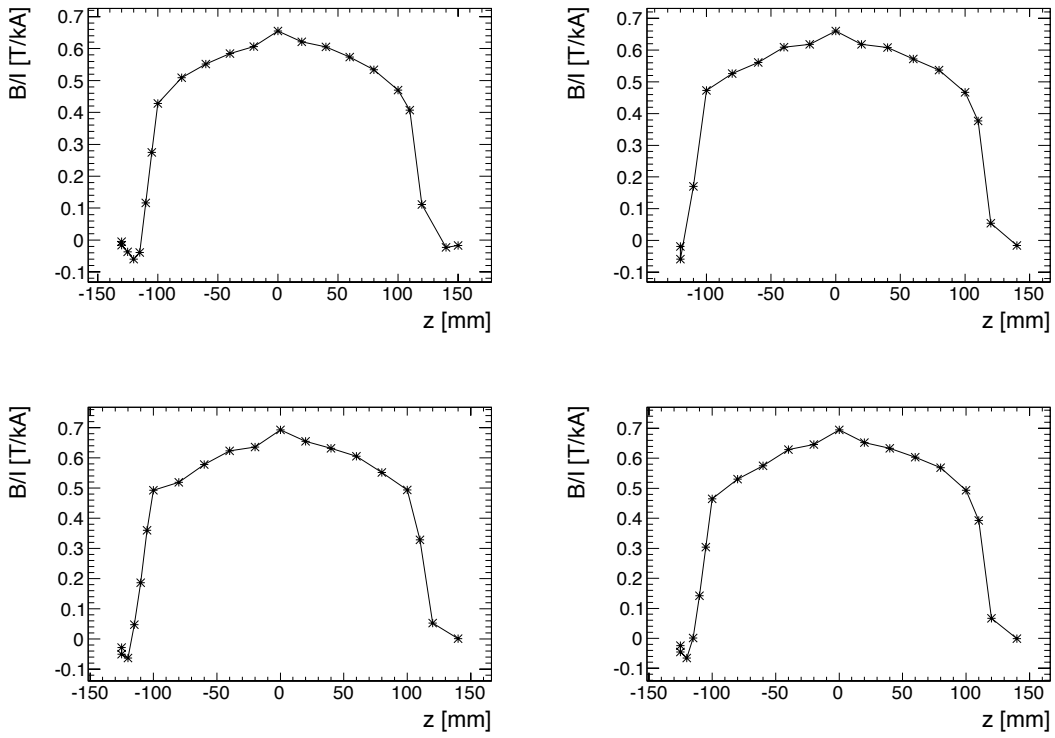

Figure 2.11: Measured map of the four magnet with a charged voltage of 0.2 kV

2.3.4 Heat loss and thermal time constant

Heat loss of a magnet is expressed from its resistance and current as $\int_0^{t_1} I^2 R dt$, where t_1 a period of one shot. Since resistance is a function of temperature, heat loss gives information of the coil temperature. The thermal time constant, on the other hand, is a time for the magnet to reach a thermal equilibrium with a given heating. Therefore it shows an efficiency of cooling with liquid nitrogen. This subsection first summarizes the relation between these parameters and the repetition or the field. Measurements of heat loss and thermal time constant are then described. Factors of the achieved repetition are finally considered.

Benefits from a small thermal time constant

The key point of repetition operation is to reduce the heat loss of the magnet. This reduction also results in a reduction of the charging time and thus speeds up the repetition. On the other hand, the time constant of the magnet to reach a thermal equilibrium represents an accumulation of heat inside the magnet. A large time constant means a large amount of heat is stuffed inside the magnet, which results in an increase of the temperature of the coil. Since the coil resistance increases with the increase of its temperature, it causes a large heat loss and lowers the repetition. This relation is schematically shown in Fig. 2.12 in case of a small time constant. Another benefit from the small time constant is an increase of the field. The decrease of the resistance gives a larger current. Field linearly scales to the current and is thus increased by the reduction of the thermal time constant.

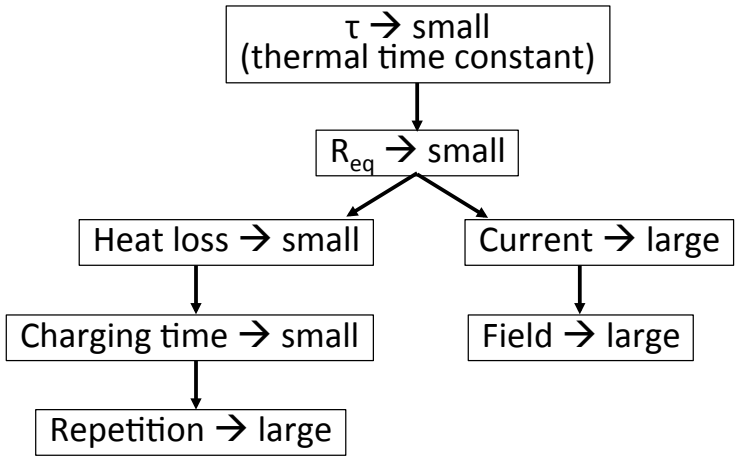

Figure 2.12: Relation among the thermal time constant τ, the resistance at thermal equilibrium R_{eq}, the heat loss , the charging time, repetition, current, and field

Measurements

Heat loss of a shot is measured by the difference of a charged voltage before and after the shot. Since the charged voltage is several kV, the read out voltage is divided by 1/1000 using a pair of 1 MΩ and 1 kΩ resistance. The heat loss is directly calculated by $CV_0^2/2 - CV_1^2/2$.

On the other hand, thermal time constant is measured in several ways. The most direct way is to measure time development of the resistance of the coil after a shot. The decay curve of the resistance is exponentially extrapolated to one right after the shot. The resistance is measured by connecting an LCR meter to the electrodes of the magnet. The measurements are carried out by changing duration of the repetition. In terms of security, however, it is sometimes dangerous for a person to wait near the magnet during the shot and to connect it by hand right after the shot.

Although time constant of some prototypes have been measured in this way, the magnets used in this experiment are measured in other ways. Since the time constant is measured with a time change of any parameter, which reflects the thermal equilibrium of the magnet. There are many ways to measure the time constant other than the direct measurement of the coil resistance. The easiest way is again to measure the voltage; the heat loss. Figure 2.13 shows time development of the heat loss measured by changing a duration of the repetition. The top left shows heat loss of serially connected two magnets of magnet2 and magnet3 with a shot repetition of ∼0.12 Hz and a charged voltage of 4 kV, corresponding to heat loss of ∼1.2 kW. The voltage is assumed to be the same for the experiment at SPring-8. The top right shows heat loss with the same condition of magnet4 and magnet5. Both time constant agree with 13–14 s. Finally, the bottom shows heat loss with operation of the two pairs simultaneously, which is the same condition of the experiment. Its total heating with a shot repetition of ∼0.12 Hz is therefore ∼2.5 kW. The capacitor bank has an electric power capacity of 20 kVA. The half of it is consumed as heat loss of charging resistances, and the rest half can be consumed as heat loss of magnets and other resistance components like, for example, cables. The shot repetition is assumed to be ∼0.1 Hz at the experiment, which corresponds to be less than one fourth of the full power capacity of the bank.

Although measurement of the time constant from voltage is easy, the read line contains a spike noise from switching a large current. As an alternative parameter, a peak value of current is used for the measurement of the time constant during the experiment. The pulsed current is read out with the CT, which line is electrically isolated.

Factors of high repetition

The measured thermal time constant τ is 13-14 s with a heating of each magnet with ∼0.6 kW. This value is so small at an unprecedented level from the sense of pulsed magnets. A typical shot repetition of a conventional magnet is ∼1 mHz. The shot

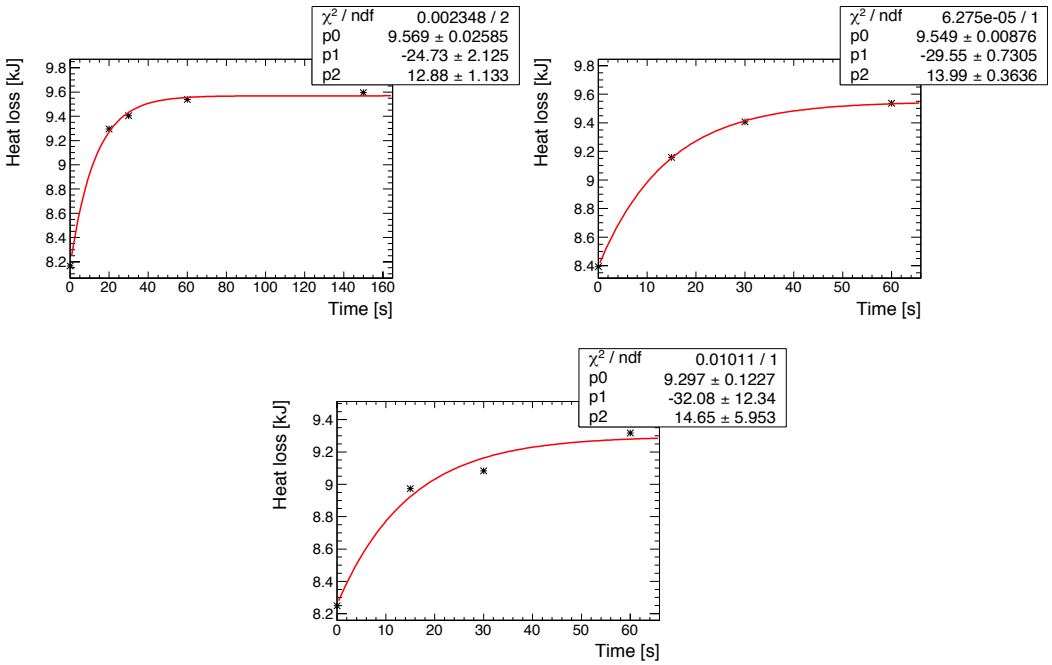

Figure 2.13: Time development of the heat loss measured by changing duration of the repetition. Top left: heat loss of serially connected two magnets (magnet2 and magnet3) with a shot repetition of ∼0.12 Hz and a charged voltage of 4 kV. Top right: heat loss with the same condition of the other set (magnet4 and magnet5) used in the experiment. Both time constants agree with 13–14 s. Bottom: heat loss with a simultaneous operation of the two pairs with shot repetition of ∼0.12 Hz, which assumes the same condition of the experiment at SPring-8.

repetition is given as $1/\tau$ for the most part and can be somewhat changed from this value, depending on huw much temperature increase is allowed to the coil. In this experiment, the heat loss at thermal equilibrium can be read from Fig. 2.13 as 9.6 kJ. Dividing it by $\int I^2 \mathrm{dt}$ gives resistance at the equilibrium. From the resistivity of copper as a function of temperature, the coil temperature is obtained as 215 K. This corresponds to an increase of the temperature from 77 K by 138 K, which is quite large though it is still well below the room temperature of ∼300 K. The repetition of 0.12 Hz is hence larger than the inverse of the 13-14 s, which is around 0.08 Hz.

The feature of high repetition mainly comes from the three factors. One is to use Cu wire, which has the best thermal conductivity among all wires. The second factor is to reduce materials with poor thermal conductivity such as GFRP as much as possible. As can be seen in Fig. 2.2, the magnet consists of metals for the most part. The use of metal near the field volume causes an increase of field cancellation from eddy current, which runs in the metal. Thus it requires divided backups at the same time. The third factor is the flat structure of the magnet to improve the cooling efficiency.

2.3.5 Destruction and repetition field

Field of repetition is decided from the maximum field, or destruction field, by taking a sufficient safety margin. The destruction field is decided by the mechanical strength of the wire and the backup. Left of Fig. 2.14 shows measured field of a prototype magnet with an increase of charged voltage. Both ends of the magnet are not enough backuped with M20 bolts and nuts as they are with the present magnet (see Fig. 2.2). Here it is referred to as a “weakly-backuped” magnet.

Linearity of the field increase changes at around 3 kV. The right figure shows a corresponding measurement of its inductance at 750 Hz. The measurement is carried out with an LCR meter after each shot. Since the Maxwell stress affects in the way to increase the field volume, its deformation also increases the inductance. About 1%-increase of inductance is generally said to be a sign of deformation. In this case, the increase of the inductance reaches 1% at 3 kV. Increase of the field volume causes a decrease of the field efficiency. This corresponds to the observed change of linearity at 3 kV. After that, the plastic deformation continues to occur along with the increase of the inductance. The magnet finally destroys at 4 kV with 14.4 T with an increase of the inductance of about 10%.

The destruction has occurred at both ends of the racetrack. Contact areas between the coil and the backup at these end-sections become half-circle shape and thus become larger than areas of straight section backuped with divided metals for each 10 mm. This causes a larger force against the backups of both ends and hence they needs to be backuped with extra metals. After this prototype, two thick plates are added to compress the weakly-backuped magnet at both ends. The destruction field of the present magnets used in the experiment is therefore considered to be larger than 14.4 T.

The field at 3 kV gives an elastic limit of the weakly-backuped magnet, and it is 12.5 T. Repetition field should be in the elastic region. Moreover, the high-repetition use requires a high durability of more than $> 10^4$ shots. Thus it also requires a sufficiently-lower repetition-field than the field at the elastic limit. Here about 30% of safety is taken from the elastic limit and it becomes 9.5 T. The Maxwell stress scales to the square of the field, and hence it corresponds to a safety factor of two for the force.

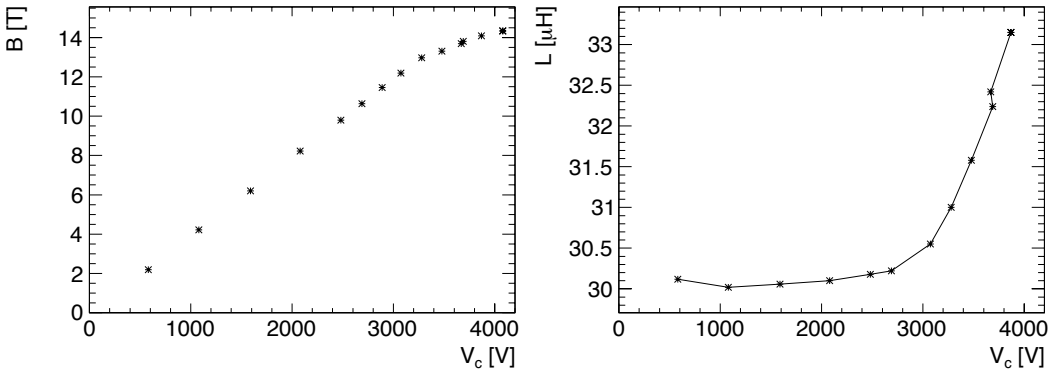

Figure 2.14: Measured field and inductance of a weakly-backuped magnet with an increase of the charged voltage.

2.3.6 Durability test

Even if the repetition field is decided by taking a safety margin into account, there are still some other destruction modes which appear during the repetition:

- friction of dielectric coating between the wires
- deterioration of wire strength due to repetitive high-density current
- fatigue failure of backup metals

The durability test is therefore necessary before the experiment.

The first magnet (maget1) is produced for the test of durability and repetition. 11.5 T has been confirmed to be within the elastic region of the magnet. After the shot of 11.5 T, the same magnet is tested its durability before the experiment. A total of 2,700 pulses at 9.5 T are generated. Deformation of the coil appears as the increase of the inductance. The test has thus been carried out checking its inductance many times during the repetition. Since a significant change of the inductance is not observed after the test ($\Delta L < 0.2\%$), the repetition field of 9.5 T has been confirmed to be safe.

2.3.7 Leakage field

Leakage of the field is measured to evaluate the field at the SPring-8 storage ring. The experimental hutches of BL19LXU are, as most of the other beamlines, located next to the electron ring. The electron orbit is well-tuned against the geomagnetic field, and thus, existence of other field of ∼10 μT could disturb the orbit. Deviation from the stabilized electron orbit causes a severe problem to other users.

Figure 2.15 shows a measured magnitude of leakage field in three directions from the center of a prototype magnet. The magnets used in this experiment almost has the same structure of this prototype and is therefore considered to have the same property foe the leakage field. The measurement is carried out with a charged voltage of 1.0 kV and capacitance of 1.6 mF. The data points are measured with another pickup coil, which is wound around 10 turns with a diameter of 100 mm. The leakage field is measured in the three directions for each data point, and the magnitude at the position is calculated. There are many obstacles in the way from the center of the magnet to the measurement positions such as a liquid nitrogen container and a safety barrier. The uncertainty of the length is therefore shown as a horizontal error. The lines show the result of 3D finite element simulation and agree with the data. The leakage can be seen to decay in inversely proportional to the cube of the length. This is a character of dipole radiation. The deviation from the decay law of simulation can be seen for the length over 1 m. It is an edge effect of the volume input to the simulation. Even if field of 10 T is generated at the magnet center, the leakage field decays to ∼100 μT (=1 G) at a length of 1 m. The length from the experimental hutch to the electron ring is 5.5 m and corresponding decay factor is $\sim 6 \times 10^{-3}$. There is also an hutch wall of steel with a thickness of 12 mm, resulting a shielding effect of 1/10. There is also another wall, which separates the experimental hall and the electron ring. The leakage field at the electron ring with 10 T at the magnet center is thus estimated as less than 60 nT for each magnet. Moreover, the two pairs of magnets are placed in a direction so as to cancel the field from each pair at the electron ring. Since the effect of the magnets on the electron orbit is estimated to be negligible, pre-study of the magnets before the experiment is exempted.

2.3.8 Oscillation test

As supplemental information, oscillation of the magnet during the pulse is described here. The peak current at a field of 9.5 T becomes 16 kA. Due to the Lorentz force, this large current oscillates the cables, which connect the magnets with electrodes. If the magnet also oscillates during the pulse, the motion would cut the beam path. In order to test this oscillation, a test measurement has been carried out with the same setup used in the experiment. The magnets are operated with 9.5 T and a shot repetition of 0.1 Hz. Laser light with the center wavelength of 650 nm passes through the pipe. Its power is measured with a laser power meter. The gain of its amplifier is adjusted to output 10 V for an input laser power of about 1 mW.

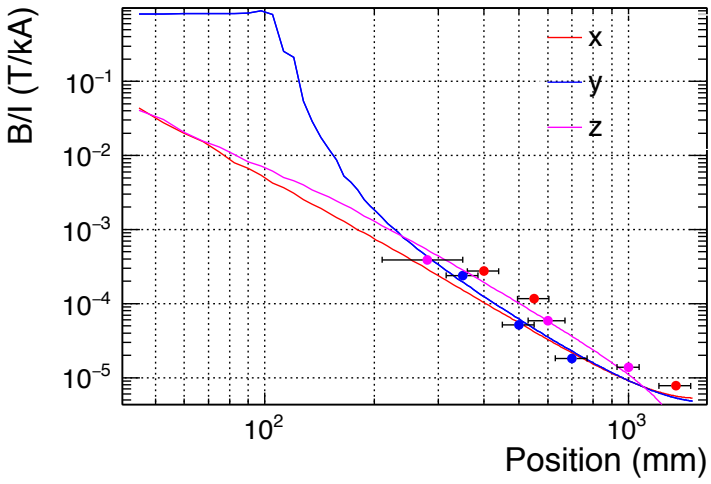

Figure 2.15: Measured magnitude of leakage field in three directions from the center of the prototype magnet. The measurement is carried out with a charged voltage of 1.0 kV and capacitance of 1.6 mF. Results of 3D finite element simulation is also shown with the corresponding line color.

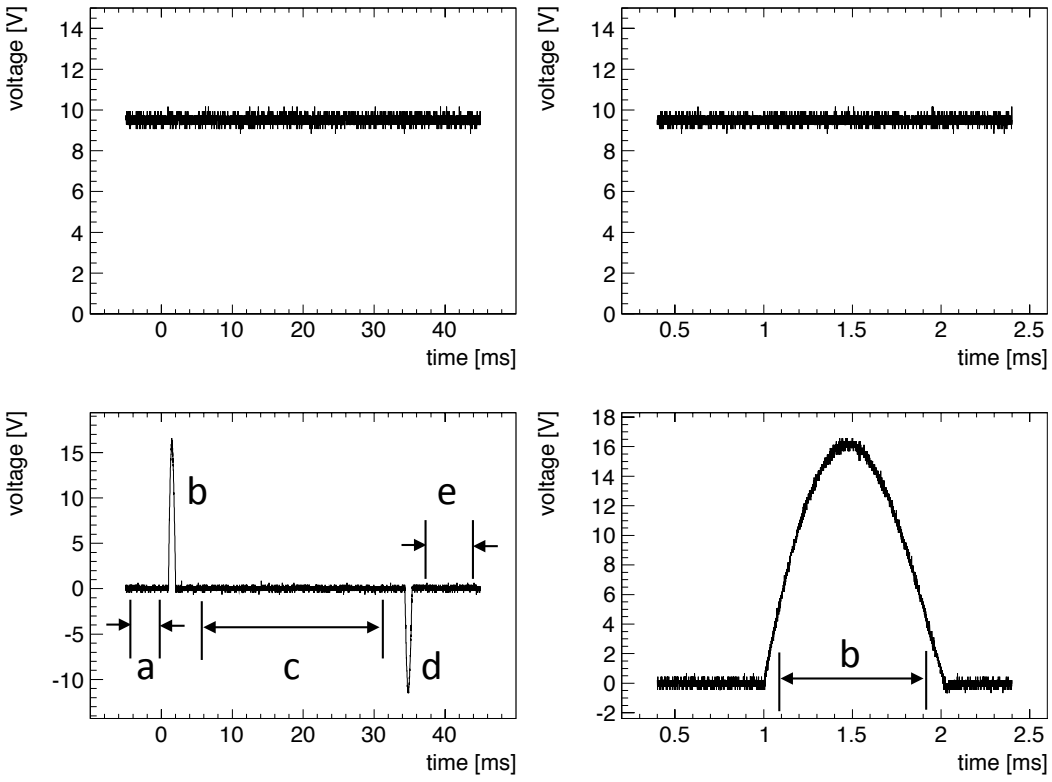

Figure 2.16: Output of the laser power meter during the oscillation test. The gain of its amplifier is adjusted to output 10 V for an input laser power of about 1 mW. The top left figure is its output, and the bottom left figure shows the corresponding current. The pulse interval is set to 33 ms. The top right figure is the magnified view around the first pulse, and the bottom-right figure shows the corresponding current. Significant change is not measured.

The diameter of the laser beam is about 4 mm and almost the same of the inner diameter of the pipe (5.4 mm).

Figure 2.16 shows the output of the power meter. The top left figure is its output, and the bottom left figure shows the corresponding current. In this case, the pulse interval is set to 33 ms. The top right figure is the magnified view around the first pulse, and the bottom right figure shows the corresponding current. Time regions before the first pulse (a), in the first pulse (b), between the pulses (c), in the second pulse (d), and after the second pulse (e) are shown in the figure. The mean power for these regions is 9.51 V (a), 9.52 V (b), 9.52 V(c), 9.51 V (d), and 9.52 V (e). All changes of the power is less than 0.1%. From Tab. 1.1, its contribution to the ALP-two-photon coupling constant becomes less than 0.025% and is thus negligible.

2.3.9 Summary of the basic performance

Table 2.3 summarizes the basic performance described in the previous sub-sections. The field efficiency is a mean of the four magnets. The thermal time constant is 15 s at the heating of 2.5 kW for four magnets, which is the same condition of the experiment. In this case, the total heat loss becomes 21 kJ at a shot repetition of 0.12 Hz. The leakage field decays to 10^{-5} at a distance of 1 m from the center of the magnet. The durability is tested with 2,700 pulses of 9.5 T.

Parameter	Value
Field efficiency	0.59 T/kA (center)
Field-length product	1.12×10^{-1} T m/A
Thermal time constant	15 s (2.5 kW)
Heat loss	21 kJ (2.5 kW)
Destruction field	>14.4 T
Durability / repetition field	>2700 pulses / 9.5 T
Leakage field	10^{-5} (1 m)

Table 2.3: Basic performance described in the previous sub-sections The field efficiency is a mean of the four magnets. The thermal time constant is 15 s at the heating of 2.5 kW, which is the same condition of the experiment. In this case, the heat loss becomes 21 kJ at a shot repetition of 0.12 Hz. The leakage field decays to 10^{-5} at a distance of 1 m from the center of the magnet. The durability is tested with 2700 pulses of 9.5 T.

2.4 Capacitor bank

A capacitor bank is used to provide pulsed current to magnets. As well as the magnets, a transportable bank is newly designed and constructed. This section describes the design and the operation sequence of the bank.

2.4.1 Principle of the capacitor bank

Although most of the circuit components are custom-made, and some of them are so expensive, basic circuit of the bank is represented as a simple LCR discharge circuit. Figure 2.17 shows a schematic diagram of the basic circuit. The left is a conventional type of the LCR discharge circuit. First, a capacitor (C) is charged from a voltage supply through a charging resistor (R_c). After the charging, the capacitor is disconnected from the supply by a switch. A trigger pulse is then sent to a cathode of a thyristor (SCR). The thyristor works as a switch which rectifies the current in one direction. Electric energy stored in the capacitor is discharged to a magnet. The magnet can be seen as a pair of serially connected inductance and resistance. The frequency of the pulse is decided from the capacitance C and the magnet inductance L as $1/2\pi\sqrt{LC}$. After a quarter cycle, the magnetic energy (i.e. the current) generated by the magnet maximizes. The energy then returns to the capacitor as electric energy at half cycle. The thyristor automatically turns off at this time since the current becomes zero. The thyristor works as a rectifier, and the LC oscillation also stops at this time. The pulse shape thus becomes a half sinusoidal wave, shown in the bottom left figure. The capacitor is then grounded, and the residual energy inversely stored in the capacitor is released. This conventional operation sequence is used in the bank as a "single pulse mode".

The right figure shows a circuit of a "repetition mode", which produces two pulses in a shot. The difference from the single pulse mode is an additional thyristor installed in anti-parallel to the original one. The energy which returns to the capacitor by the first thyristor, is not grounded but discharged again with the second thyristor. The time interval between the turn-on of the two thyristors is adjustable. If the second thyristor is turned on right after the turn-off of the first one, the two half sinusoidal waves are generated without a break, shown in the bottom right figure. The return energy of the capacitor is positively charged and has been decreased by the two times of heat losses at the magnet. The decrease of the energy is additionally charged from the supply. This repetition mode reduces the charging time compared with the single pulse mode, where the charging starts from 0 V every time.

2.4.2 Circuit and operation sequence

Figure 2.18 shows the circuit diagram of the capacitor bank. A charging section, which provides a high voltage, is commonly used for the succeeding discharge section. The discharge section consists of two parallel components, and each drives two magnets. They have the same structure and therefore only one of them is described here.

A commercial AC 200V line is input to the bank. The bank is turned on by a circuit breaker (CB) of 75 A, which protects the line from overcurrent. The mechanical contactor (MC) is a large relay with a thermal fuse (TH). By closing the MC, the AC 200 V is applied to a primary side of a slidac (SL), which is

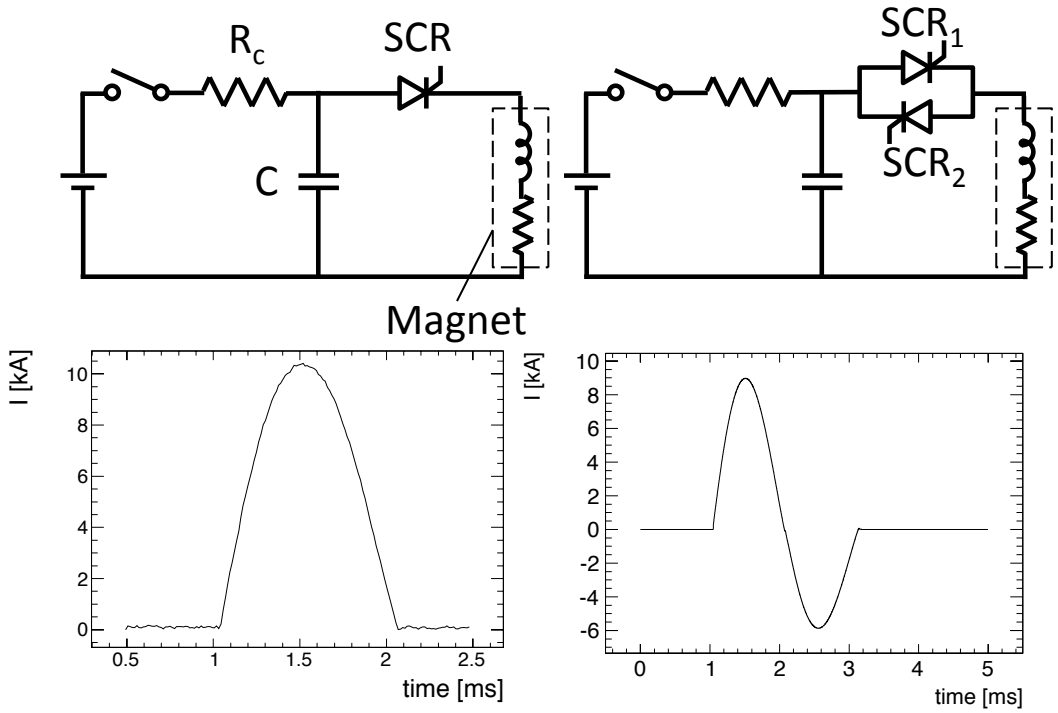

Figure 2.17: Basic circuit of the capacitor bank. Left: a conventional LCR circuit used for "single pulse mode". Right: a circuit of the "repetition mode". Anti-parallel thyristors are triggered to produce a shot with two pulses.

an adjustable voltage transformer. The secondary side of the SL is connected to a primary side of a step-up transformer (TR) with a voltage ratio of 30. The output high voltage from the TR is rectified by a diode bridge (DB) with full wave rectification. By closing a charging relay (CR), the capacitor (C) is charged through a charging resistor (R_C). The time constant of the charging is given as the product of C and R_C. In case of charging from 0 V, the initial high voltage causes a large current at the beginning of the charging and heats up the R_C. Since a fast charging is not required for the initial charging, the capacitor is charged slowly through R_{CL} with 6 kΩ. In case of the additional charging, on the other hand, the voltage drops by only the heat loss, and the fast charging is required for the repetition. The capacitor is therefore charged rapidly through R_{CH} with 900 Ω. The fast or slow charging is selected by a resistor relay (RR). The voltage of the capacitor is divided by a pair of resistors (R_{m1} and R_{m2}). The 1/1000-divided voltage is read out by a digital meter relay (DMR), which turns on or off with a preset voltage. It is used for the control of the operation sequence.

After the capacitor is charged up, the upstream charging section is disconnected by opening the charging relay. The first trigger is then sent to the SCR1 and the first pulse is generated. Due to impedance mismatch between the output cable and the magnet, a reflected voltage returns to the SCR. Since the voltage can cause destruction of the SCR, it is absorbed by a pair of a terminal resistor (R_t) and capacitor (C_t) inserted in parallel to the output terminal.

In case of a single pulse mode, the returned voltage is grounded through an earth resistor (R_e) by closing an earth relay (ER). In case of a repetition mode, on the other hand, the second trigger is sent to SCR2 and the returned voltage positively charges the C. The amount of the energy loss is additionally charged through the R_{CH} by closing the CR. Due to the current capacity of the SCRs, the same discharge section is connected in parallel to lower the current running to each SCR by half. Each drives two magnets placed either upstream or downstream side of an LSW shield.

Figure 2.19 shows a measured time variation of the capacitor voltage with a shot repetition of 0.5 Hz at 1 kV. The voltage is reversed after the first pulse, and then reversed again after the succeeding second pulse. Right after that, an additional charging starts until the voltage returns to its original value.

Figure 2.20 shows a whole picture of the bank. Four units of capacitors are seen in the front. Each unit has three capacitors and each of them is 0.25 mF. Unit1 and unit2 are connected in parallel and used as 1.5 mF. Similarly, the pair of unit3 and unit4 are used as another 1.5 mF. Behind these, the main body of the bank is seen. It has a four-story structure and its height is 2 m.

Figure 2.21 shows a picture of the inside. The transformer (6 kV, 20 kVA) is seen in front of the left picture. Behind it is the slidac with 20 kVA. The charging resistors are shown in the right picture. R_{CL} is composed of 6 kΩ resistors connected with 2p2s (two-parallel of two-serial). R_{CH} is, on the other hand, composed of 16 resistors of 900 Ω and 700 W each, connected with 4p4s.

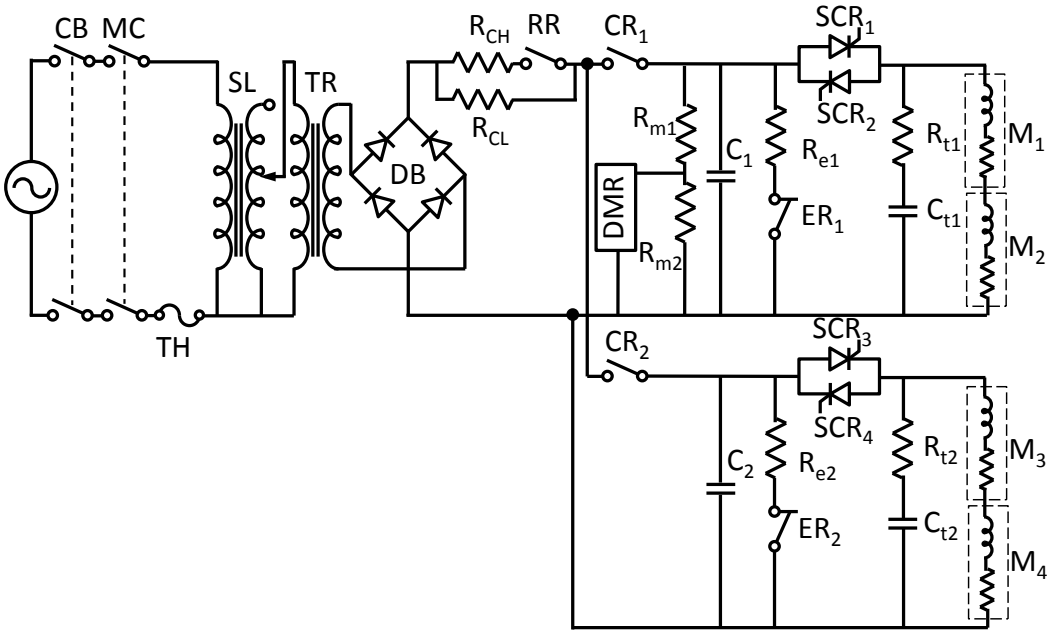

Figure 2.18: Circuit diagram of the capacitor bank with an additional charging system. The left half is the charging section, and the right half is the discharge section. The discharge section consists of two parallel components constructed with the same structure. Each drives two magnets.

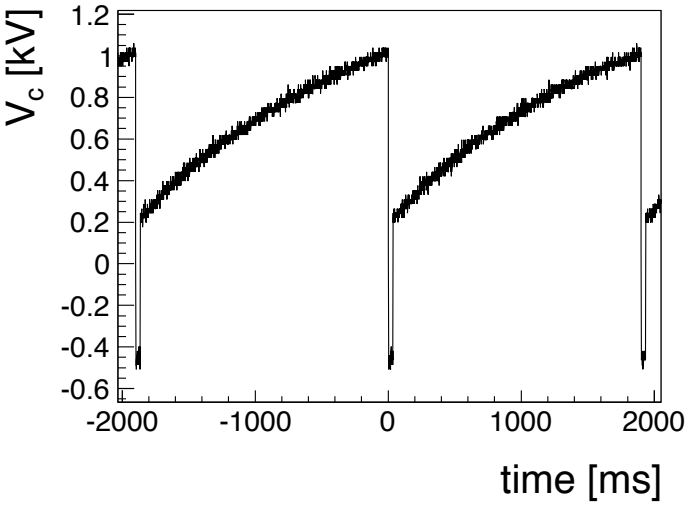

Figure 2.19: Measured time variation of the capacitor voltage with a shot repetition of 0.5 Hz at 1 kV. The voltage is reversed after the first pulse, and then reversed again after the succeeding second pulse. Right after that, an additional charging starts until the voltage returns to its original value.

Figure 2.22 shows a picture of the upper floors. The top picture shows the third floor. It consists of high-voltage components including thyristors (SCR1 and SCR2). Coaxial cables connecting the capacitor and magnets are seen on the right. Another set of components are symmetrically placed behind them. The bottom shows the fourth floor. The trigger boards (TB1, TB2) receive optical signals from a control panel through optical fibers, and drive pulse transformers. There can be seen four sets of the pulse transformers. Each consists of a two-stage structure and drives one thyristor. The dividing resistors (R_{m1} and R_{m2}) are shown on the left. Its lower voltage is read out by DMR.

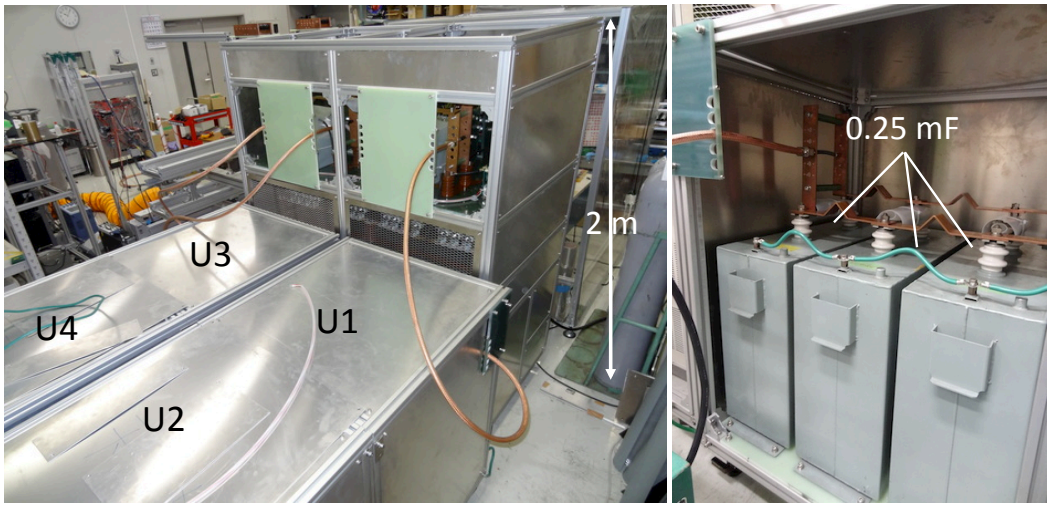

Figure 2.20: Whole picture of the bank. Four units of capacitors are seen in the front (left). Each unit has three capacitors and each of them is 0.25 mF (right). Behind these, the main body of the bank is seen. It has a four-story structure and its height is 2 m.

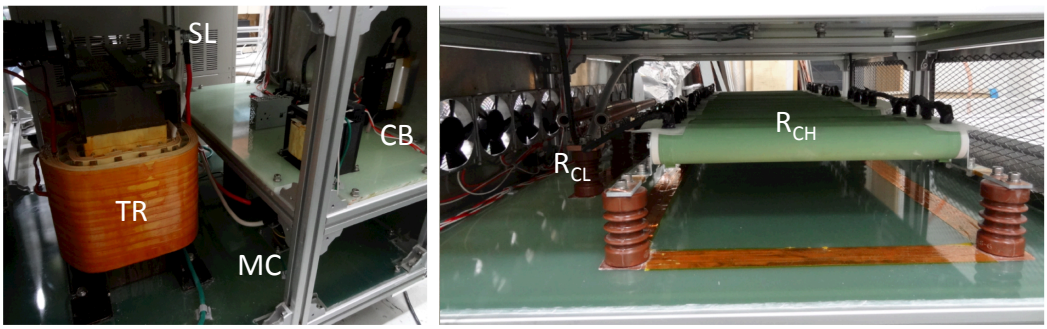

Figure 2.21: Lower floors. Left: the first floor. The transformer (6 kV, 20 kVA) is seen in front of the left picture. Behind it is the slidac with 20 kVA. Right: the second floor. R_{CL} is composed of 6 kΩ resistors connected with 2p2s. R_{CH} is, on the other hand, composed of 16 resistors of 900 Ω and 700 W each, connected with 4p4s.

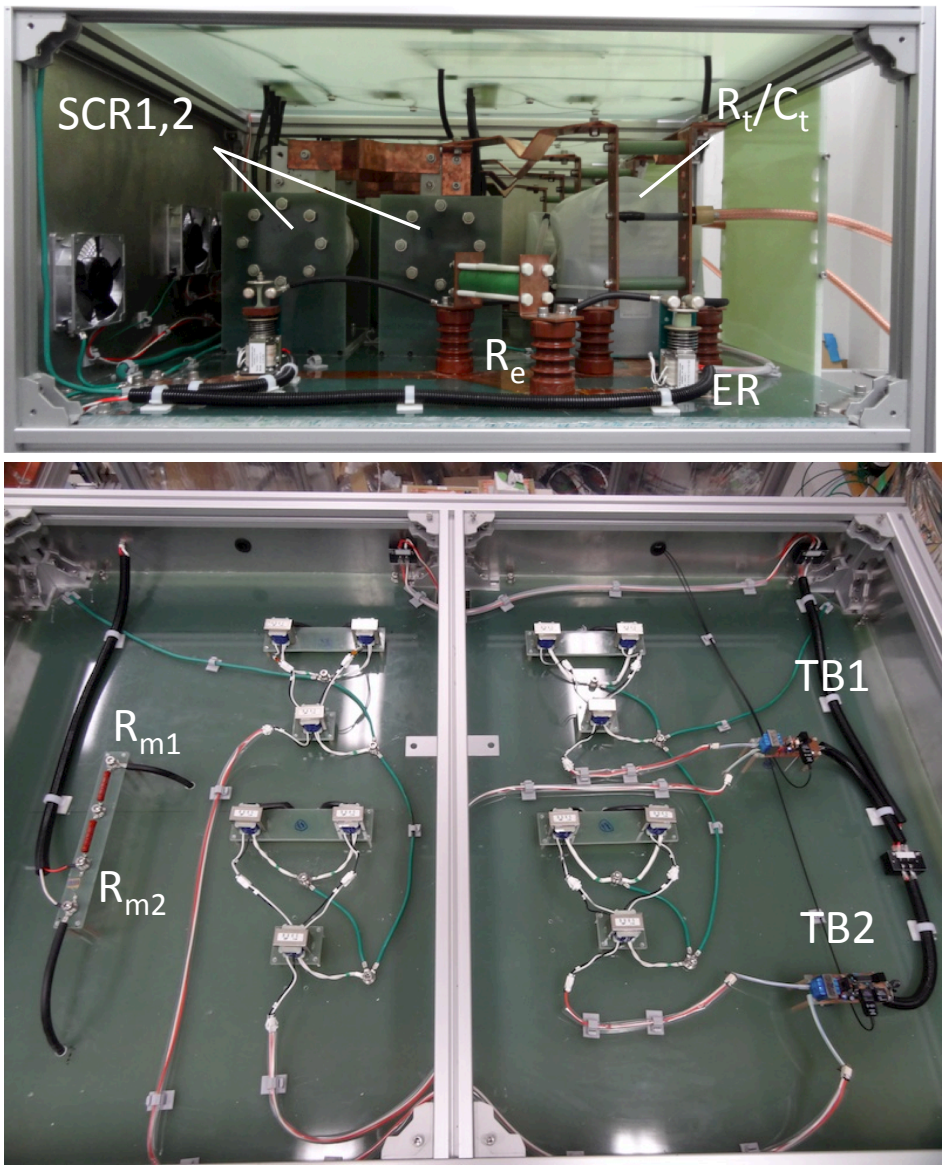

Figure 2.22: Upper floors. Top: the third floor. Another set of components are symmetrically placed behind them. Bottom: the fourth floor. The trigger boards (TB1, TB2) drive pulse transformers. There can be seen four sets of the pulse transformers. The dividing resistors (R_{m1} and R_{m2}) are shown on the left, and its lower voltage is read out by DMR.

Chapter 3

Setup and devices

This chapter describes the setup of the X-ray LSW search. The whole system is explained in the first section. The setup spreads to three hutches. The following section describes the devices of each hutch in detail.

3.1 Whole setup

The top view of the whole system is schematically shown in Fig. 3.1. The experiment has been carried out at BL19LXU in SPring-8. Three hutches of the beamline are used in this experiment. The role of each hutch is as follows:

- optics hutch (OH): beamline components for the processing of direct beam from the undulator,
- the first experimental hutch (EH1): a main hutch where the field generation system is placed,
- the second experimental hutch (EH2): detection of signal X rays and electronics of NIM and CAMAC.

Direct beams from the undulator goes to OH. In order to obtain a desired beam quality, several fixed components in the hutch are used. The beam then goes to EH1. It is a main hutch where the field generation system composed of the magnets and the bank is placed. Four magnets are used for the LSW conversion regions. They are placed in liquid-nitrogen containers and are cooled down to 77K. The beam passes through the upstream conversion region ($a \to \gamma$) and is dumped into a hole of a lead shield. A silicon PIN photodiode (PIN B) is embedded in the shield and monitors the beam intensity. The ALP components pass through the shield and are re-converted in the downstream conversion region ($\gamma \to a$). The regenerated photons go to EH2, where a low-energy germanium detector is placed. It detects the regenerated photons. All the conversion regions are evacuated. The other beam paths are also evacuated to reduce air-attenuation of the X rays.

Due to the safety from radiation, human bodies are kept out from these hutches during the beam is on. The bank is therefore controlled from the outside of the hutch. There is a duct hole in each hutch, which leads to the outside. Signal or control cables go through the duct. The liquid nitrogen is also filled from the outside. The hose goes through the duct and reaches the containers.

The magnets and the bank are contained in the same hutch. This has two reasons. First, the bank itself is a high-voltage and a large-current device. If there is some problem, it might become dangerous in the worst case. Therefore they are confined in the hutch and the door is closed. In this way, human bodies cannot be harmed. The other reason is noisy environment. During the operation of the magnets, the hutch is filled with EMI (electromagnetic interference) noise. The ground potential also becomes unstable during shots. If the operation-control system or the data-acquisition electronics are placed in the same environment, the noise causes malfunction of these devices or severely spoils the analog data. Thus the hutch wall also works as a separator of the environment.

3.2 OH: beamline components

This section describes the beamline components. The beamline used in this experiment is BL19LXU (BeamLine 19 Long X-ray Undulator), which is located at the west of SPring-8. First, property of the X-ray beam is summarized. The BL19LXU undulator is then described. The X-ray beam from the undulator has the world's strongest intensity. Direct beam from the undulator goes to OH, where fixed components are placed. They are used to process the direct beam and to obtain a desired beam quality. Principle of these components is described in the following sub-sections.

3.2.1 Summary of the beam property

Table 3.1 shows a summary of the beam property, which will be described in the following sub-sections. The energy of the beam is selected to 9.5 keV. This energy is decided from the efficiency of the detector, the energy spectrum of the undulator, and the energy spectrum of the background spectrum. Intensity of the beam is measured in front of the detector (PIN A), and its mean value is about 3×10^{13} photon/s (Tab. 4.1). Since the undulator bends electron bunches in the horizontal plane, the beam is polarized to the horizontal direction. Higher-order radiations from the undulator are cut to be less than $\sim$1% by using a pair of total reflection mirrors. The beam size has been measured in the previous beamtime, and it is 1.0 mm (H)$\times$0.5 mm (V). The X-ray beam has the same time structure of electron bunches. The bunch interval is 23.6 ns and is much smaller than a pulse width of field of $\sim$1 ms. The X-ray beam therefore is regarded as a DC X-ray source.

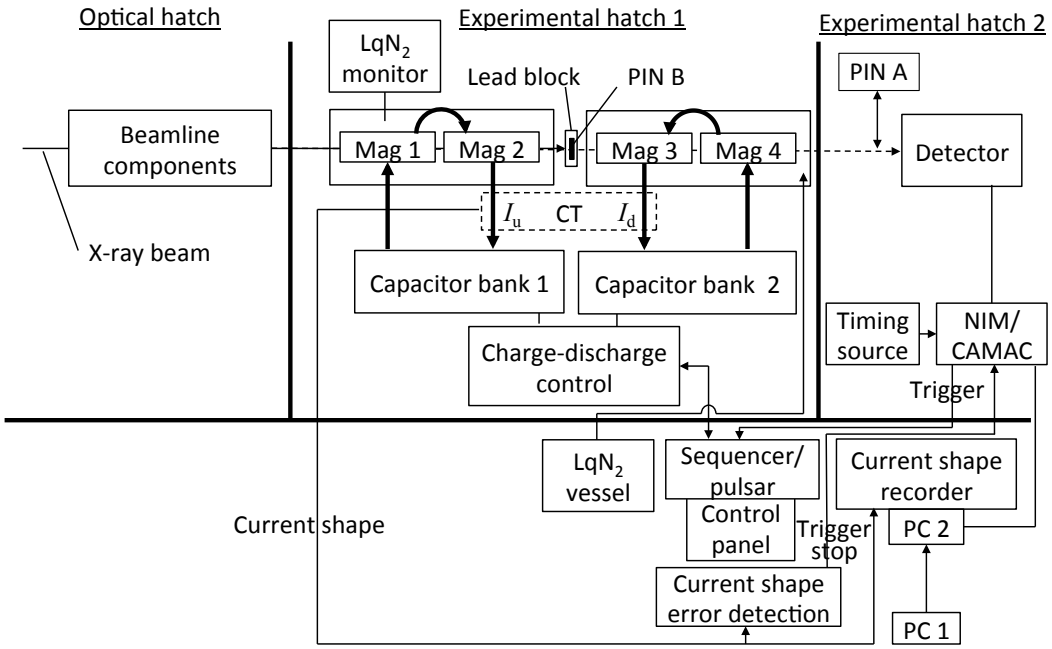

Figure 3.1: Top view of the whole system. The beamline components of the optics hutch are used to obtain a good beam quality. The first experimental hutch is a main hutch of the experiment, where the field generation system is placed. The bank is operated from the outside of the hutch. A detector and DAQ electronics are placed in the next hutch. The upstream current I_{u} serially runs through Mag1 and Mag2, and the downstream one I_{d} through Mag3 and Mag4. Although the sum of the two currents is read out with the CT during the run, their ratio is also measured in additional measurements by passing each cable one by one to evaluate their difference (Sec. 4.7).

Parameter	Value
Photon energy	9.5 keV
Intensity (in front of the detector)	$\sim 3 \times 10^{13}$ photon/s
Polarization	horizontal
Higher-order radiation	cut by the double mirrors
Beam size (prev.)	1.0 mm (H)×0.5 mm (V)
Electron bunch interval	23.6 ns (∼DC)

Table 3.1: Beam property from the BL19LXU undulator after beamline components in OH.

3.2.2 BL19LXU undulator

An undulator is an important device since it works as a light source in this experiment and provides intense X-ray beams to the magnets. Electron bunches

circulating in the storage ring go through the undulator. Their orbits are bent by periodically aligned magnets. Synchrotron radiations are emitted at each bending. They interfere with each other and generate phase-matched beams with a small band width of about $\Delta\omega/\omega = 10^{-2}$.

Undulators are characterized with field strength (B_u), periodic length (λ_u), periodicity (N), and gap distance between the two arrays of permanent magnets. Undulator radiations are, on the other hand, characterized with wavelength (λ_n), band width, and intensity. Wavelength of undulator radiation is written as

$$\lambda_n = \frac{\lambda_u}{2n\gamma^2}\left(1 + \frac{K^2}{2}\right), \tag{3.1}$$

where n is degree of higher-order radiation, γ the Lorentz factor of 8 GeV/511 keV$= 1.5 \times 10^4$. λ_u is a common value of 32 mm for standard undulators in SPring-8. K is a parameter proportional to the product of B_u and λ_u, and is written as

$$K = \frac{eB_u\lambda_u}{2\pi m_e c} = 0.934 B_u[\mathrm{T}]\ \lambda_u[\mathrm{cm}]. \tag{3.2}$$

If the magnet is divided in two to reduce λ_u, B_u is also reduced in accordance with its size. This gives K to be unchanged. On the other hand, B_u can be increased by closing the gap distance between the arrays of magnets. Hence K can be seen as a parameter of the gap distance. In Eq. (3.1), both λ_u and γ are fixed values. The wavelength is then changed by varying the gap distance. It can be closed 12 mm at the minimum, which corresponds to a 0.57 T and $K = 1.70$. From Eq. (3.1), this defines the maximum wavelength of 1.6 $\mathring{A}$ or 7.8 keV for the fundamental wavelength. On the other hand, the limit of $K = 0$, which corresponds to a sufficiently widened gap, defines the minimum wavelength of 0.65 $\mathring{A}$ or 19 keV for the fundamental.

Large length of an undulator increases the beam intensity. Practically, however, it is not so for the most cases. Since it is hard to produce a long undulator as one body, it is divided into several segments when they are manufactured. If they are simply connected, the expected intensity will not be obtained due to the distortion of phase-matching condition of the X rays, which occurs at the connections. This limits the intensity of a long undulator.

The left of Fig 3.2 shows a picture of the BL19LXU undulator. It is composed of five segments and each segment has a length is 5 m. The right figure shows a cross section at the connection between the segments. The magnets (and of course the path of the electrons) are contained in a cylindrical vacuum chamber. It is referred to as an "in-vacuum undulator". The in-vacuum undulator was used for the first time in SPring-8 and then spread to world's synchrotron radiation facilities. In a conventional undulator, magnets are placed at outside of the vacuum. This inevitably requires space for the connection. On the other hand, the in-vacuum undulators are connected without such space, keeping the phase-matching condition. Among all the beamlines in the world, the BL19LXU undulator has the

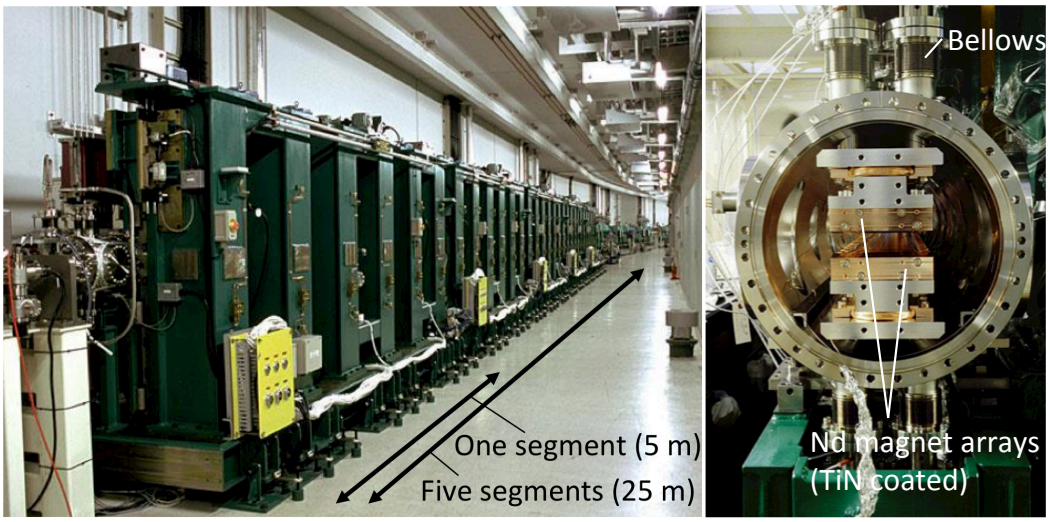

Figure 3.2: BL19LXU undulator. Left: the undulator is composed of five segments, and has a total length of 25 m. Right: a cross section at the connection. The magnets are contained in a cylindrical vacuum chamber, and it is referred to as an "in-vacuum undulator". The length and the in-vacuum technology used in the undulator make its intensity uniquely strong.

longest length of 25 m whereas the length of a standard undulator in SPring-8 is 4.5 m. This length and the in-vacuum technology used in the undulator make its intensity uniquely strong. Without any losses in the air or in widows, its maximum output reaches 2×10^{14} photon/s around 10 keV.

3.2.3 Double crystal monochromator

The off-axis components of the direct beam from the undulator is cut at the front end. The beam then goes to a monochromator and is monochromated with Bragg reflection at a silicon crystal. The beam is reflected again by the second crystal to restore its horizontal direction. This type of monochromator is referred to as a DCM (double crystal monochromator). Figure 3.3 shows a picture and a schematic view of the DCM. The inside of the DCM is evacuated, and the crystals are cooled with liquid nitrogen due to heat load of the beam. The two metal hoses, in which the liquid nitrogen flows, are shown in front of the left figure.

Figure 3.4 shows the Bragg angle as a function of X-ray energy, calculated with the Bragg condition of

$$2d \sin \theta_{\mathrm{B}} = \lambda, \tag{3.3}$$

where d the lattice spacing of silicon ($d_{111} = 3.14$ Å and $d_{311} = 1.64$ Å). Brass angles of the two crystals are tuned to pick up the peak intensity of the energy spectrum of undulator radiation. If both of their positions are fixed, however, the height of the outgoing beam is also changed. This requires height adjustments of all

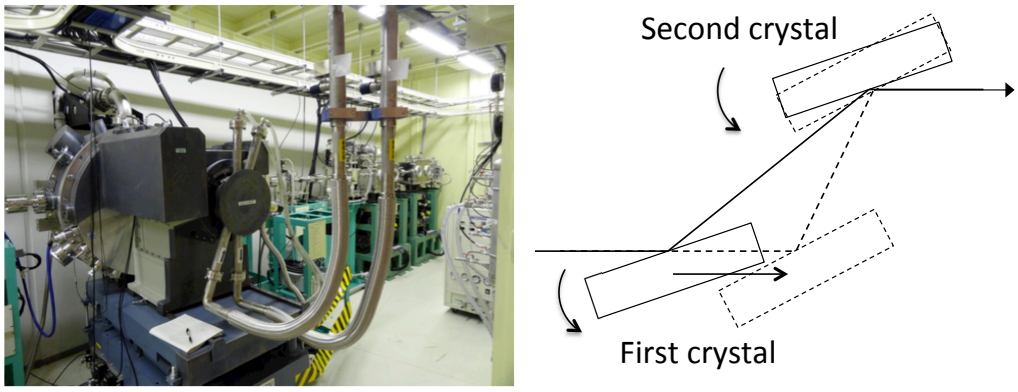

Figure 3.3: Double crystal monochromator (DCM). Left: inside of the DCM is evacuated, and the crystals are cooled with liquid nitrogen due to heat load of the beam. The two metal hoses, in which the liquid nitrogen flows, are shown in front of the left figure. Right: translation movement of the first crystal as well as rotations of the both. In this way, height of the outgoing beam does not change with the energy.

the downstream devices for different energies. To avoid this, translation movement is attached to the first crystal. Thus the first crystal moves with the change of the energy to keep the height of the outgoing beam constant.

There is one remark about the DMC. The outgoing beams are monochromated with the level of $\Delta\omega/\omega = 10^{-4}$ whereas the direct beams from the undulator have $\Delta\omega/\omega = 10^{-2}$. A good monochromaticity is not required for this experiment since the energy resolution of the detector is about 100 eV (σ). Intensity loss at the DCM is quite large and reduces the intensity to about 1% of the original one. In terms of the sensitivity, it is thus desirable not to use the DCM. It is, however, a fixed component, and removing it requires many applications and tests for the safety.

3.2.4 Double mirror

In order to cut higher-order radiations from the undulator, a pair of total reflection mirrors is used. Figure 3.5 shows a picture and a schematic view of the mirrors. They are used as a pair to restore the horizontal direction. Since Eq. (3.3) is also satisfied for the higher-order wavelengths, they are contained in the beams from the DCM. Refractive index of X rays for materials is slightly smaller than unity and is written as

$$n(\lambda) = 1 - \delta = 1 - \frac{2n_e\alpha\lambda^2}{m_e c^2}, \tag{3.4}$$

where n_e the electron number density, α the fine structure constant. From this equation, high-energy X rays have a larger $n(\lambda)$. Since the condition of total reflection is expressed as $n(\lambda) = \cos\theta_c$, high-energy X rays have a shallow critical

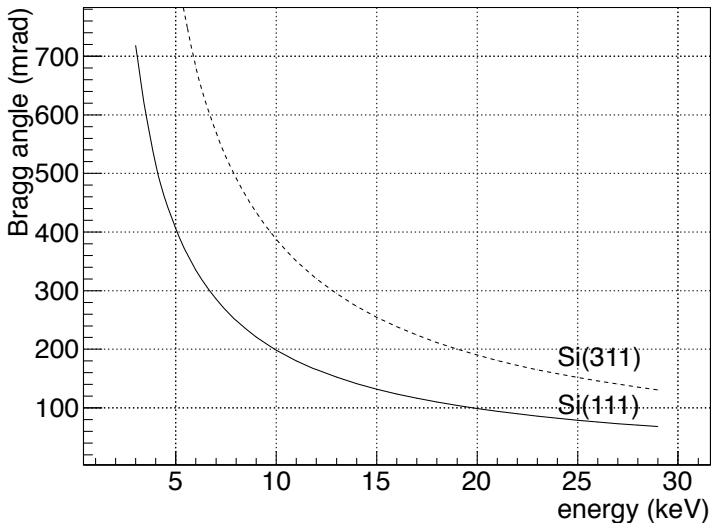

Figure 3.4: Bragg angle as a function of the X-ray energy, calculated with the Bragg condition of $2d \sin\theta_B = \lambda$, where d the lattice spacing of silicon ($d_{111} = 3.14$ Å and $d_{311} = 1.64$ Å).

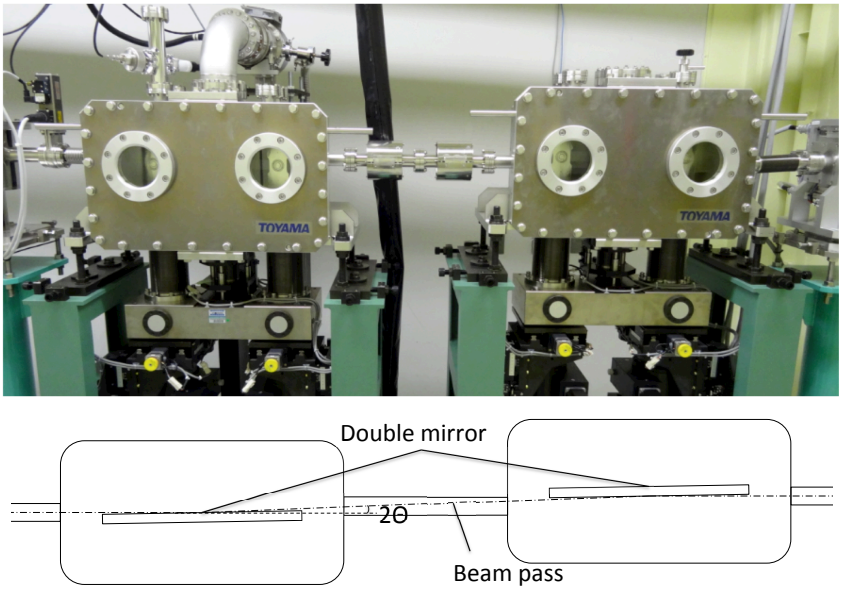

Figure 3.5: Total reflection mirrors. Two mirrors are used torestore the horizontal axis. They cut higher components of X rays, which have a shallow critical angle.

nagle θ_c. In this experiment, both angles of the mirrors are set to 4.5 mrad to cut the higher components of the 9.5-keV X rays.

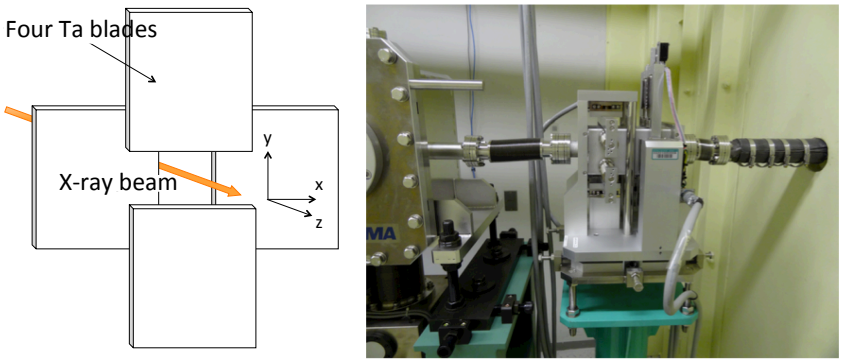

Figure 3.6: Four-jaw slits. Left: a schematic view. Right: a picture. Beam profile is measured by scanning the blades along the horizontal or the vertical directions.

3.2.5 Slits

The beam size is measured in the previous beamtime using four blades of tantalum slits. Figure 3.6 shows a schematic view and a picture. Beam profile is measured by scanning the blades along the horizontal or the vertical directions. Figure 3.7 shows the measured profiles. The horizontal full width is about 1.0 mm and the vertical one is about 0.5 mm. Since the undulator bends electron bunches in the horizontal plane, the horizontal width becomes larger than the vertical one. During the run, the slit is loosely closed so as to cut only off-axis components.

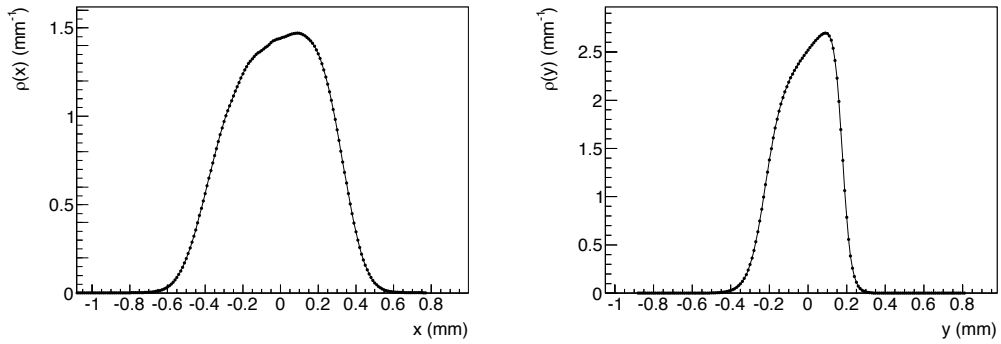

Figure 3.7: Measured width of the beam. The horizontal full width is about 1.0 mm and the vertical one is about 0.5 mm. Since the undulator bends electron bunches in the horizontal plane, the horizontal width becomes larger than the vertical one.

3.3 EH1: field generation system

Left of Fig. 3.8 shows a picture of the first experimental hutch in BL19LXU. The hutch width is about 4 m along the beam axis. First, magnets on a base table are

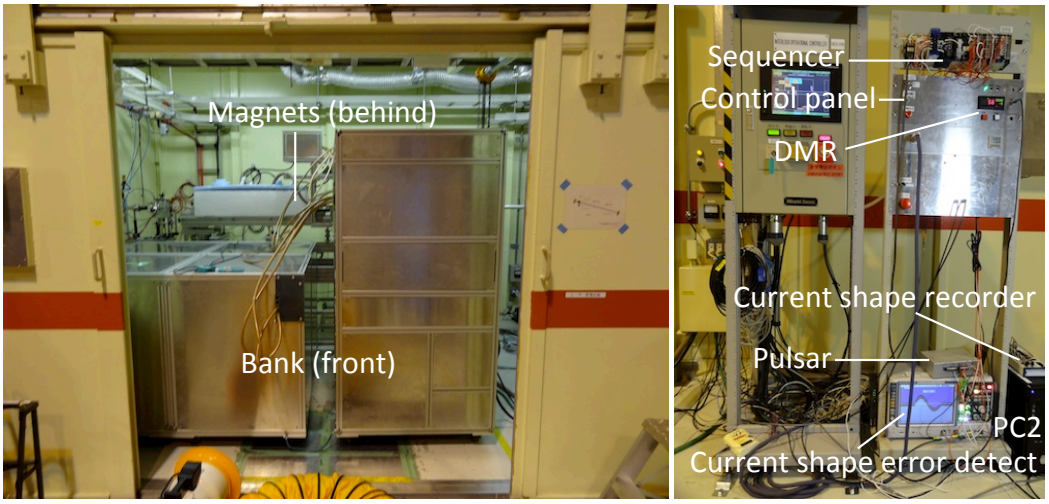

Figure 3.8: The first experimental hutch and the control panel. Left: the hutch width is about 4 m along the beam axis. First, magnets are installed into the back of the hutch. The capacitor bank is then installed at their front. Right: the control system composed of the sequencer, the pulser, the current shape error detection, the current shape recorder, and the control panel.

installed into the back of the hutch. After their alignment on the beam axis, the capacitor bank is installed at their front. The magnets and the bank are contained in the hutch so as not to harm the human body in the worst case.

3.3.1 Control system

Right of Fig. 3.8 shows a picture of the control system. It consists of the following items:

- sequencer
- pulser
- current shape error detection
- current shape recorder
- control panel with a DMR (digital meter relay), which shows a charged voltage

The sequencer is placed on top of the system. It consists of PLC (programmable logic controller) modules of Omron. It exchanges signals with contact relays in a control section of the bank (the charge-discharge control).

The pulser is used to send signals to the trigger boards placed on top of the bank. A high voltage appears at the pulse transformers on the board. The pulser

is therefore electrically disconnected from the boards by sending signals through an optical fiber. The optical signal is sent and received by photo-couplers. Since one shot contains two pulses, the pulser sends two independent signals for each shot. The time interval between the two signals is adjustable and has been written into an FPGA board with a 50-MHz clock. In this experiment, it is set to generate continuous pulses without their time interval.

The control panel is operated by hand at the initial charging. The operation sequence is as follows; first, a charging voltage is input to preset the DMR. Charging is started by a push button and stops at the preset voltage. A charging resistance is switched from 6 kΩ to 900 Ω by turning a toggle switch. Operation mode is then switched by turning another toggle switch from the single pulse mode to the repetition mode.

3.3.2 Safety measures

The field generation system is composed of the magnets and the bank described in the previous chapter. It also includes the control system of operation sequence. During the run, inside of the hutch becomes dangerous environment, which is listed as;

- X-ray radiation
- high-voltage and large-current devices (the magnets and the bank)
- low temperature of liquid nitrogen
- low oxygen density
- EMI noise

The environment is monitored from the outside with two web cameras. Some measured quantities are also monitored from the outside to check safety and stability. They are listed as below:

- peak current and current shape of each shot using the CT
- temperature of the charging resistance and the thyristor using non-contact (i.e. radiation) thermometers
- surface level of the liquid nitrogen in a container using thermometers with different heights
- oxygen density of the atmosphere using oxygen density monitors
- vacuum pressure using a vacuum gauge
- beam intensity at the central shield

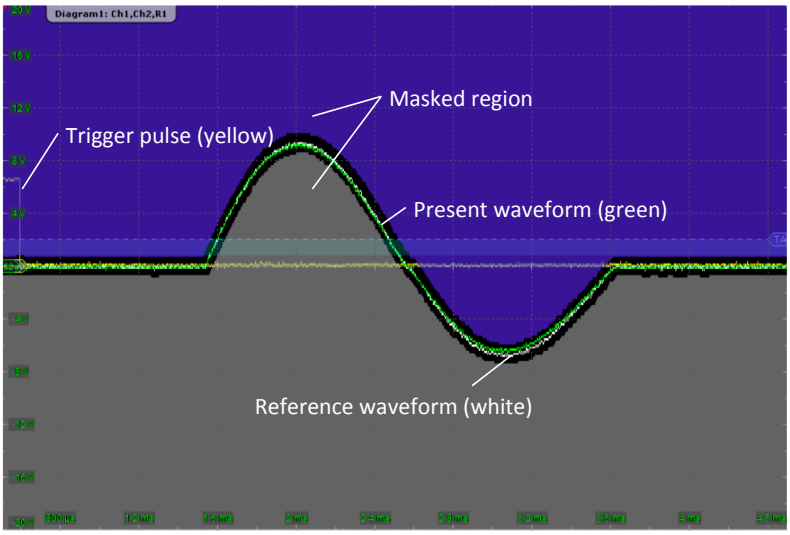

Figure 3.9: Mask test in a repetition mode with a charged voltage of 3.75 kV. The vertical scale of voltage is converted to the current by a coefficient of the CT, which is 1 V/kA. A trigger TTL pulse is shown with yellow. A reference current shape is shown with white. The green is a current shape of the present shot. Margin from the reference shape is set to ±0.2 div for the vertical scale, which corresponds to ±0.8 V. For the horizontal scale, it is set to ±0.05 div corresponding to 20 μs.

Since the current shape directly reflects an anomalous behavior of the magnets and the bank, It is compared with a reference shape with each shot at online. In case of the detection of shape error, a signal is fed back to the sequencer and stops the next shot. To do this, a "mask test" function of a digital oscilloscope (Rohde & Schwarz, RTO1044) is used. Figure 3.9 shows a display of the mask test in 3.75 kV repetition. The vertical scale of voltage is converted to the current by a coefficient of the CT, which is 1 V/kA. A trigger TTL pulse is shown with yellow. A reference current shape is shown with white. The green is a current shape of the present shot. Margin from the reference shape is set to ±0.2 div for the vertical scale, which corresponds to ±0.8 V. For the horizontal scale, it is set to ±0.05 div corresponding to 20 μs. Sign of magnet destruction appears as a spike or deformation of current shape. When it occurs, the current shape deviates from the reference one and enters the masked region. An error signal is then sent from the oscilloscope to the sequencer and stops the next shot.

3.3.3 Base table and electrodes

Figure 3.10 shows a picture of the base table. It is moved to the hutch with its casters. It has five-axis alignment mechanism other than the translation along the beam direction. Three of them including the height is realized using level adjusters on its foot. Linear guide rails are used for another translation, which transversely

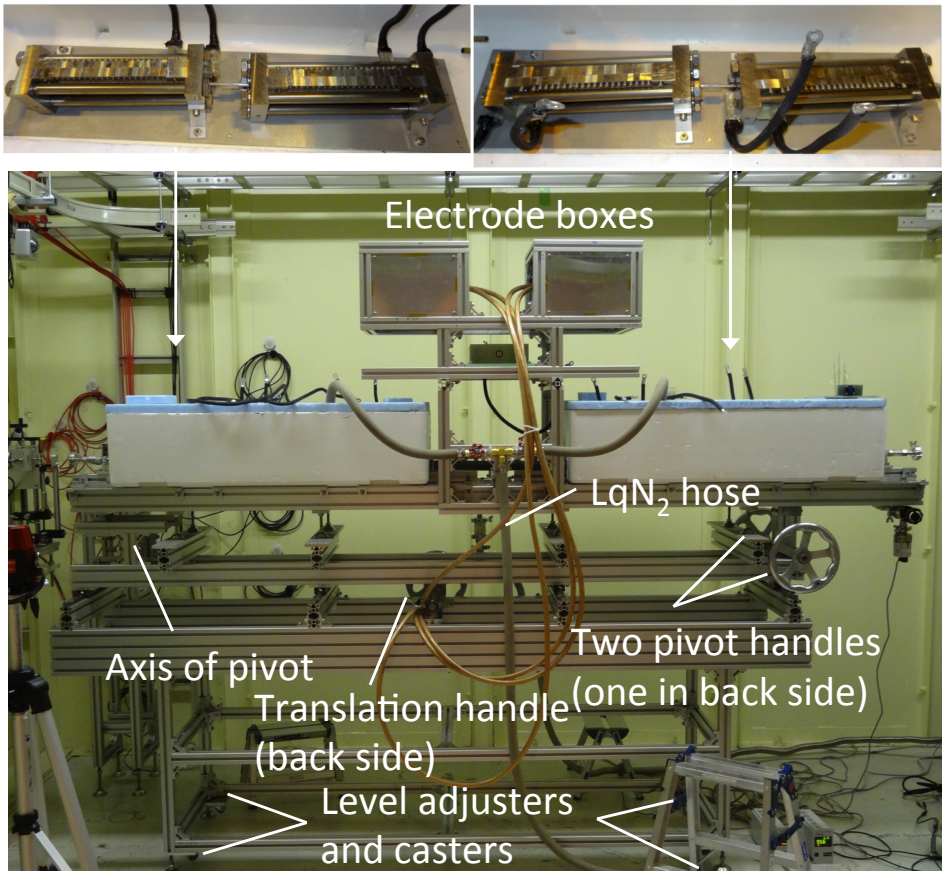

Figure 3.10: Base table of the magnets. It has five-axis alignment mechanism other than the translation along the beam direction. Three of them including the height is realized using level adjusters on its foot. Linear guide rails are used for another translation, which transversely crosses the beam axis. Swing of the base axis applies pivot mechanism.

crosses the beam axis. The rest degree of freedom, swing of the base axis, applies pivot mechanism. The pivot axis is placed at the head of the base, and its tail is moved with two handles.

A hose of liquid nitrogen is drawn from the outside of the hutch. It is divided with a tee branch and they go to the containers. The magnet containers are made of polystyrene boxes.

At the center of the base table, terminal electrodes and the CT is placed. They are shown in Fig. 3.11, which is seen from the back of the hutch. There are two terminal boxes and they are lined with polyimide sheets. Each of them has a high-voltage (HV) and a low-voltage (LV) electrode fixed with each other with insulators. Coaxial cables are drawn from the bank and connected to them. The two cables from each LV electrode go through the CT and are then connected to the inner

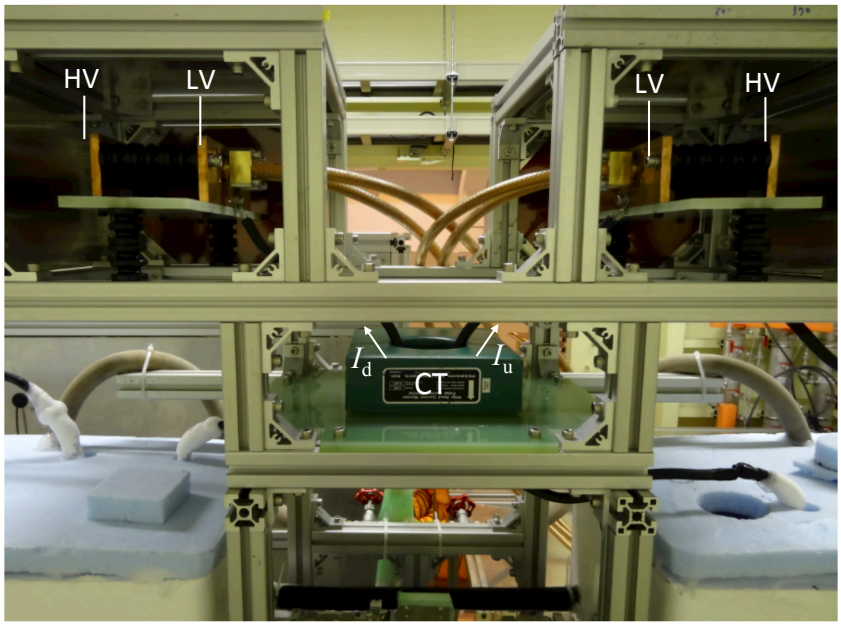

Figure 3.11: Terminal boxes seen from the back of the hutch. Each of them has a high-voltage (HV) and a low-voltage (LV) electrode fixed with each other with insulators. Coaxial cables are drawn from the bank and connected to them. The two cables from each LV electrode go through the CT and are then connected to the inner magnets. In this way, the sum of the two current (I_u and I_d) is read out with the CT.

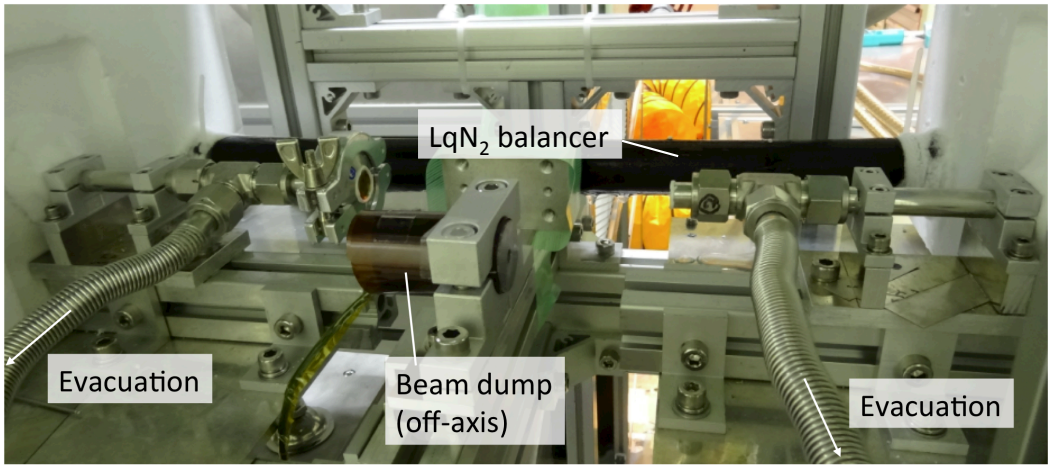

Figure 3.12: Central space below the CT. The beam dump is placed at the center. There are X-ray windows of polyimide with a thickness of 12.5 μm. The air of conversion regions is evacuated near these windows with a scroll pump. Behind these components, a surface level balancer for liquid nitrogen is placed.

magnets. On the other hand, the two cables from each HV electrode are connected to the outer magnets. The two magnets in the upstream or the downstream region is serially connected.

Figure 3.12 shows a picture of central space below the CT. At the center, the beam dump of lead is placed. It is fixed with a holder and slides on a rail. It is evacuated during alignment or intensity measurement in front of the detector. There are also X-ray windows of polyimide with a thickness of 12.5 μm. The air of conversion regions is evacuated near these windows with a scroll pump. Behind these components, a surface level balancer for liquid nitrogen is placed. It is composed of a brass pipe coated with an insulator and used to match the surface levels of both containers.

3.3.4 Alignment

The magnets and the detector are aligned on the beam axis. Procedure of this alignment is as follows. First, position of the X-ray beam is marked using a piece of photosensitive paper. Two positions in EH1, the most upstream and the most downstream positions near the wall, are marked in this way. X-ray spot on these papers is then pierced with a needle to create a pinhole.

To remember the beam axis, a laser diode with a center wavelength of 650 nm is used. The laser is placed at off-axis position near the most upstream of the hutch. A retractable mirror is also placed on the axis before the first paper. The laser is then directed to the mirror. The directions of the laser and of the mirror are adjusted until the laser light goes through the two pinholes.

After this alignment of the laser axis, the laser works as a reference of the X-ray beam and is hence referred to as a "reference laser". Power of the laser is measured with a laser power meter placed downstream of the hutch. The power meter is also retractable. Magnets are then aligned onto the laser so that the center of its pipe coincides with it. The alignment is carried out checking the power meter. Center of the detector placed in EH2 is also aligned onto the reference laser. Finally, all retractable components are slid to off-axis positions, and X-ray intensity is checked in front of the detector using a photodiode (PIN A), which will be described in a following section (Sec. 3.5.1).

3.3.5 Other devices and components

Liquid-nitrogen vessels

When data acquisition run is started, heat loss of the magnets (the total heating is about 2.5 kW) consumes liquid nitrogen. In addition to this, natural evaporation also lowers the surface level. Each container has a volume of 40 ℓ and they are filled every 1–2 hours. Figure 3.13 shows a picture of the vessels placed at the outside of EH1. The hose becomes frozen when the nitrogen is flowing. A pair of vessels is therefore used for a rapid switching. A 100-ℓ vessel is consumed every 1–2 hours, and 12 vessels are repeatedly filled by a supplier.

Figure 3.13: Vessels of liquid nitrogen placed at the outside of EH1. Left: a pair of vessels is used for a rapid switching. The hose goes through the duct. Right: 12 vessels are repeatedly filled by a supplier.

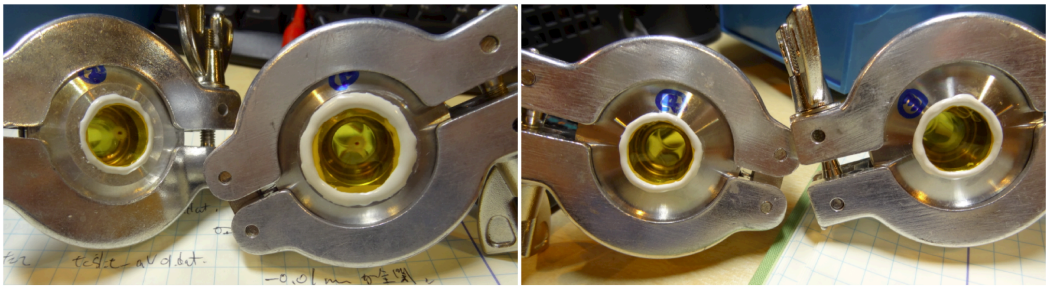

Figure 3.14: X-ray windows. Left: windows of the conversion region. X-ray beam of BL19LXU is so strong and there can be seen a burn spot on these center. Right: windows of the re-conversion region.

X-ray windows

A polyimide foil with a thickness of 12.5 μm is used for windows of the conversion and the re-conversion regions. Their pictures are shown in Fig. 3.14. The left figure shows the upstream windows. Since X-ray beams of BL19LXU is so strong, there can be seen a burn spot on the center of these windows. The beam is blocked at the central shield and therefore the spots do not appear on the downstream windows.

The other dielectric devices

Dielectric devices are used to control and monitor high-voltage environment of EH1. Two of them, the CT and optical fibers, are described so far. In addition to these, the other dielectric devices are explained below:

- current transformer: Pearson Model 14239, reads out the magnet current.
- optical fiber: Sumitomo Electric CCV-HC-20/07, transmits a signal to the trigger board.

- HV noise-cut transformer: Denkenseiki NCT-I4, 2 kV (DC) / 10 kV (impulse), provides AC100V to devices in EH1.
- isolation amplifier: NF Electronic Instruments 5325, amplifies the read-out voltage of the photodiode in the shield (PIN B).
- insulation flange: Cosmotec N40ISL12KV, protects the vacuum pump.

3.4 EH2: detection system

Detection system consists of a germanium detector, its radiation shield, and DAQ electronics. Performance of the detector is characterized by energy resolution, detection efficiency, time resolution, and background count rate. This section first summarizes them, and then each item is described in detail. Alignment of the detector on the beam axis is also explained.

3.4.1 Summary of detector performance

Table 3.2 shows a summary of the detector performance, which will be described in the following sub-sections.

Parameter	Value
Energy resolution	93 eV (σ) at 9.5 keV
Detection efficiency	89±1% at 9.5 keV
Time resolution	20–30 ns at 14.4 keV
BG count rate (typ.)	6×10^{-4} cps/0.5 keV at 9.5 keV

Table 3.2: Detector performance

3.4.2 Shield and alignment

Environmental radiation becomes background events of the signal. To reduce them, the detector is doubly shielded. The outer shield consists of lead blocks and is used to protect the detector from the environmental radiation. The inner shield is attached to the end cap of the detector. It shields X rays from a decay chain of ^{210}Pb contained in the outer shield. By using a flange shield, it also works to narrow its open angle and blocks X rays from the off-axis.

Figure 3.15 shows pictures and a schematic view of the inner shield. The left figure shows the bare end cap (aluminum) of a germanium detector (Canberra GL0210). The crystal has a diameter of 16 mm and a thickness of 10 mm. The detector window is composed of beryllium and its thickness is 500 μm. The right figure shows the inner shield covering the end cap. The end cap is covered with a brass cylinder on its side and with a stainless-steel plate on its face. To avoid the

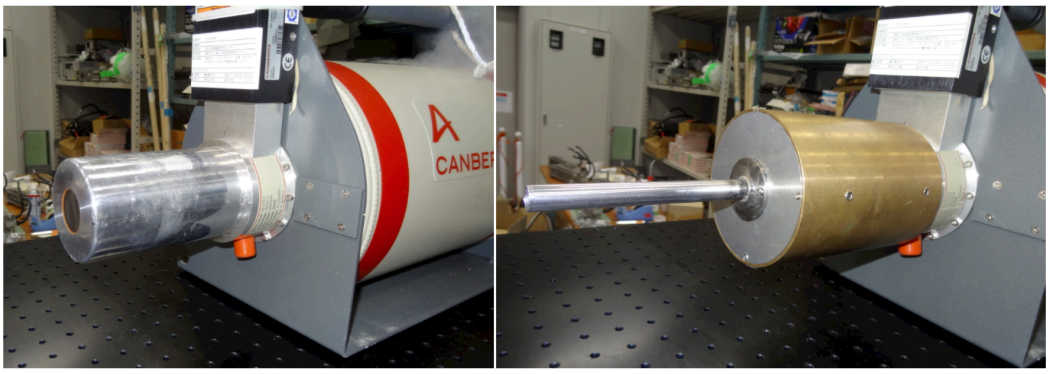

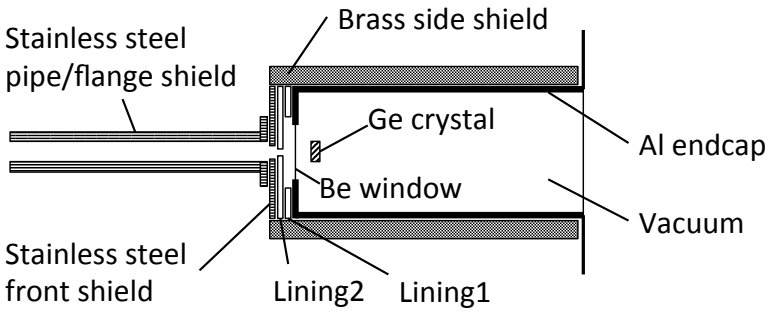

Figure 3.15: Germanium detector and its inner shield. Left: the bare end cap (aluminum) of a germanium detector (Canberra GL0210). Right: the inner shield covering the end cap. Bottom: the end cap is covered with a brass cylinder on its side and with a stainless-steel plate on its face. A stainless-steel pipe-flange shield is attached to the front shield to narrow the open angle.

direct contact of the plate on the detector window, two plastic linings are inserted between them. A stainless-steel pipe-flange shield is attached to the front shield to narrow the open angle.

Figure 3.16 shows pictures of the outer shield. As shown in the left figure, the detector is aligned to the beam axis. Using the reference laser described in the previous section. the alignment is first carried out without the pipe-flange shield and is then checked with X rays using a photosensitive paper. This check is carried out before and after the run to confirm that the detector has not moved. The right figure shows the outer shield. The solid angle other than the pipe-flange shield and the Dewar is covered with lead blocks with a thickness of more than 50 mm.

Figure 3.17 shows measured background energy spectra. The energy threshold is set around 3 keV. The black spectrum is obtained without the outer shield. The background rate is 8×10^{-3} cps/0.5 keV at 9.5 keV, which is the photon energy of the experiment. The red spectrum is obtained using the outer shield, and its rate is 6×10^{-4} cps/0.5 keV at 9.5 keV. The shield reduces the background rate by a factor of more than 10^{-1}.

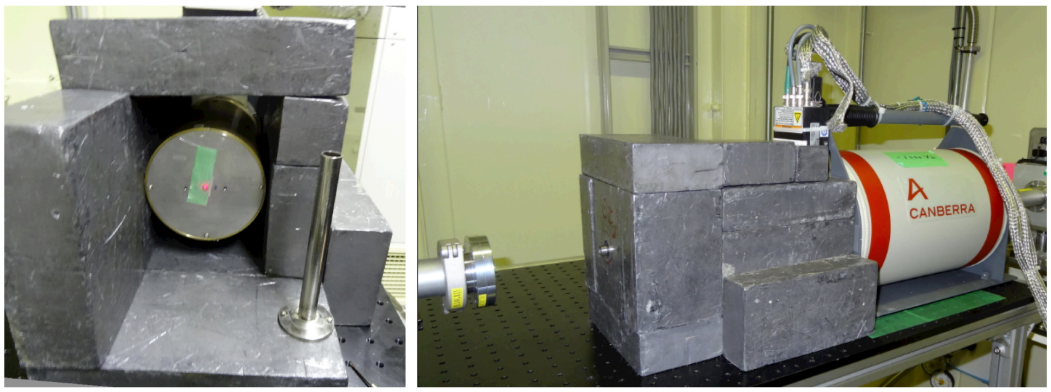

Figure 3.16: Outer shield of the detector. Left: the detector is aligned to the beam axis using a reference laser. Right: the outer shield. The solid angle other than the pipe-flange and the Dewar is covered with lead blocks with a thickness of more than 50 mm.

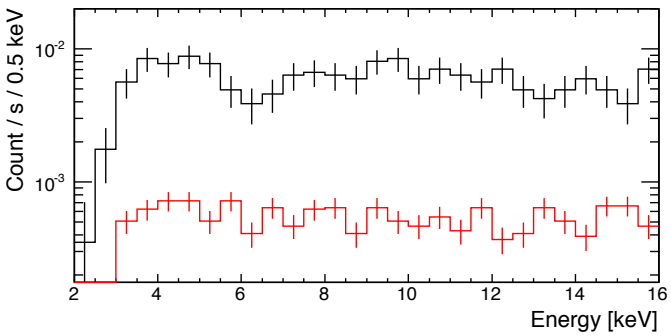

Figure 3.17: Measured background energy spectra. The energy threshold is set around 3 keV. The black/red spectrum is obtained without/with the outer shield, respectively. The shield reduces the background rate by a factor of more than 10^{-1}.

3.4.3 Energy resolution

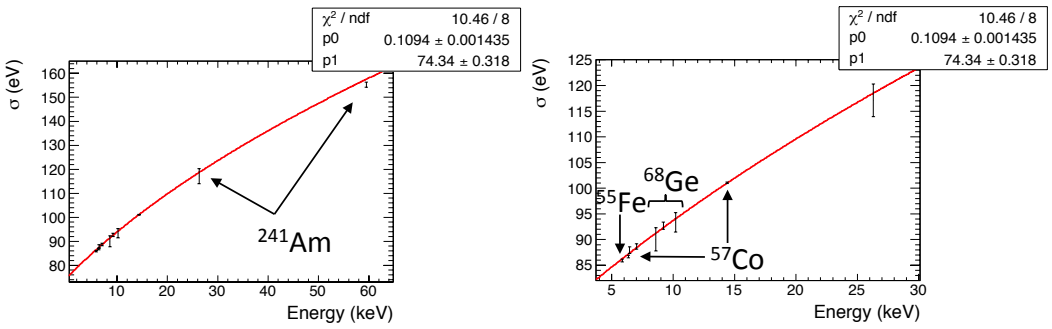

Figure 3.18: Measured resolution as a function of the energy. The data points are fitted with a function of $\sigma = \sqrt{F\,W\,E + \sigma_0^2}$ (see the text). The energy resolution at 9.5 keV is obtained as 93 eV.

In order to define energy region for the signal X rays, energy resolution of the detector is measured using several checking sources. Figure 3.18 shows the measured resolution expressed as the standard deviation. The data points are fitted with a function of

$$\sigma = \sqrt{F\,W\,E + \sigma_0^2}, \tag{3.5}$$

where F the Fano factor, W the W-value of the germanium of 2.95 eV, E the energy in keV, and σ_0 the constant offset from the electric noise. The Fano factor for the germanium detector is typically 0.05–0.13. The fitting is carried out by setting F and σ_0 as the fitting parameters. Their obtained values are shown in the box of the figure. The energy resolution at 9.5 keV, which is the photon energy, is thus calculated as 93 eV.

3.4.4 Detection efficiency

Detection efficiency including attenuation in the detector window is also measured with checking sources. Since the K-edge of germanium is 11 keV, thickness of dead layer on surface of the crystal decides the efficiency at low energies. The thickness is obtained with comparison of the data with GEANT4 simulation. A conventional way is to measure the efficiency as a function of energy. It is then compared with simulation, varying the thickness. The true thickness is estimated to be at the minimum of the χ^2 distribution.

For low-energy X rays around 10 keV, on the other hand, scattering and absorption in the source window or in the air gives not a small correction to the data. Moreover, each source (and each measurement) has a different window thickness, window material, and distance from the detector. To evaluate this precisely, simulations are carried out for each source and for each energy with corresponding geometry. Thus the thickness is obtained for each measurement and is shown in the left of Fig. 3.19. It is obtained to be 1.83 ± 0.48 μm, which is a reasonable

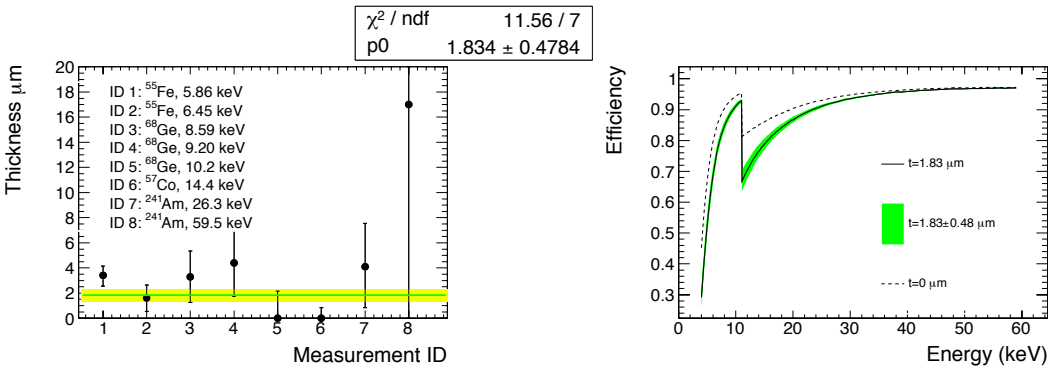

Figure 3.19: Measurement of the detection efficiency. Left: comparison of the thickness of the surface dead layer with data and simulation. Right: the detector efficiency obtained by GEANT4 simulation with the thickness of 1.83 ± 0.48 μm, including attenuation in the detector window. The dashed line shows the efficiency without the dead layer. Efficiency at low energies below 5 keV steeply decreases due to attenuation in the detector window.

value for this type of germanium detector. Using this value, the efficiency curve is finally obtained by a simulation. It is shown in the right figure and its value is 0.89 ± 0.01 at 9.5 keV. The dashed line shows efficiency without the dead layer ($t = 0$). Efficiency at low energies below 5 keV steeply decreases due to attenuation in the detector window.

3.4.5 Time resolution

Signal events are synchronized with the pulsed field. To cut the other unsynchronized events, time resolution of the detector is also measured. Figure 3.20 shows a picture of the measurement. The measurement applies a decay chain of the ^{57}Co source shown in the left of Fig. 3.21. First, a 5/2- state decays to a 3/2- state and emits a 122-keV γ ray. The state succeedingly decays to the ground state (1/2-) with time constant of 141.8 ns and emits a 14.4-keV γ ray. The 122-keV γ ray is detected with a $LaBr_3$ scintillator mounted on a PMT, and it defines the start time. The succeeding 14.4-keV γ ray is detected with the germanium detector.

As shown in the right of Fig. 3.21, the detector has a point-like back electrode. Travel time of an electron hence becomes smaller when the photon hits the center of the crystal. The photon from the outer edge, on the other hand, gives a large travel time. The top of Fig. 3.22 shows a calculation of this travel time. The blue line shows the electron travel time and the red line is an expected time spectrum obtained by decaying the blue line with a time constant of 141.8 ns. The middle figure shows a measured time spectrum. The decay curve is fitted with an exponential function, and it gives a decay constant of 142.9±1.2 ns in agreement with the expected time constant. The time resolution is red to be about 150 ns. The bottom figure shows a time spectrum measured with the inner shield as shown in

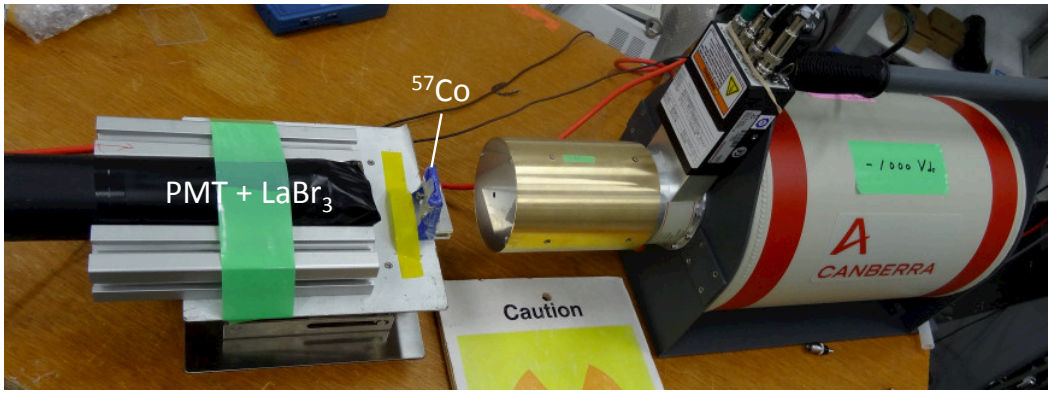

Figure 3.20: Measurement of time resolution.

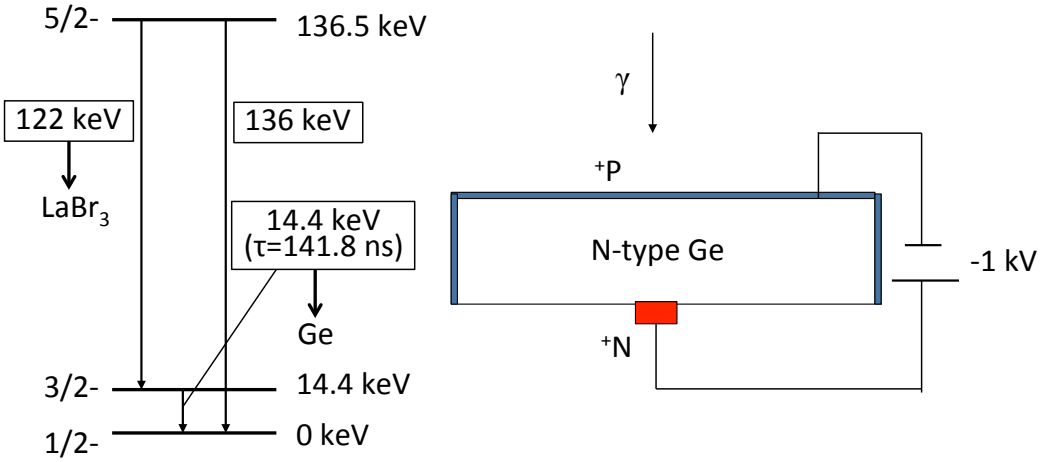

Figure 3.21: ^{57}Co level diagram and geometry of the crystal electrodes. Left: a 5/2- state decays to a 3/2- state and emits a 122-keV γ ray. The state succeedingly decays to the ground state (1/2-) with time constant of 141.8 ns and emits a 14.4-keV γ ray. The 122-keV γ ray is detected with a $LaBr_3$ scintillator mounted on a PMT whereas the succeeding 14.4-keV γ ray is detected with the germanium detector. Right: the detector has a point-like back electrode, and the electron travel time becomes smaller when the photon hits the center of the crystal.

Fig. 3.20. The stainless-steel face shield collimates the incident X rays with an aperture of 5 mm. The fitting gives a decay constant of 140.5±3.3 ns and a better time resolution of 20–30 ns is obtained.

3.5 Intensity measurement

This section describes measurements of beam intensity. Two PIN photodiodes, PIN A and PIN B, are used at different positions shown in Fig. 3.1. PIN A is used

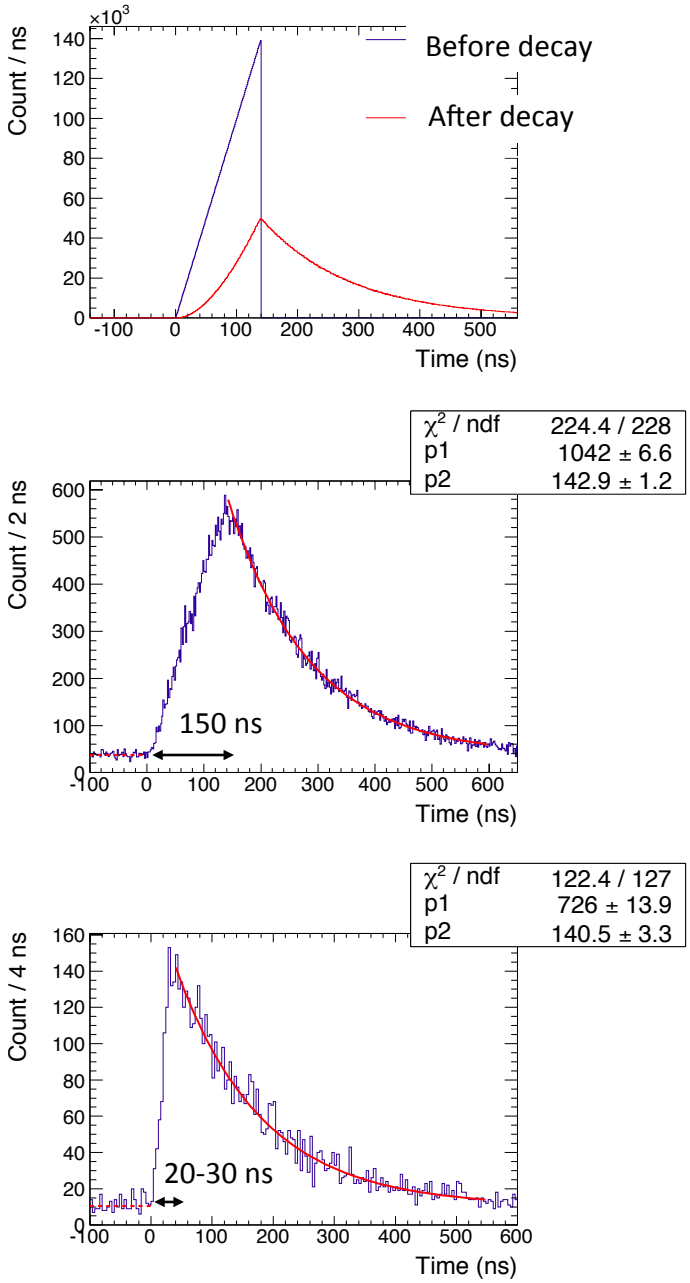

Figure 3.22: Calculation and measurements of the time spectra. Top:: calculated time spectra. The blue line shows the electron travel time and the red line is an expected time spectrum obtained by decaying the blue line with a time constant of 141.8 ns. Middle/bottom: measured time spectra without/with a face shield with an aperture of 5 mm, respectively. The start time is defined by the 122-keV γ ray detected by a $LaBr_3$ scintillator.

for intensity measurement in front of the germanium detector. The measurement is carried out at the occasion of change from one data set to the next one (see Sec. 4.3.1). During the run, it is evacuated to off-axis position. PIN B, on the other hand, is always located on the beam axis at central space of the base plate. It monitors the beam intensity during the run. When the beam intensity at the detector is measured with PIN A, PIN B is evacuated to the off-axis.

3.5.1 Intensity measurement between data sets: PIN A

Intensity of the X rays is measured with a silicon PIN photodiode (Hamamatsu, S3590-09). Figure 3.23 shows its picture. It has a depletion thickness of 300 μm. For the light shielding, the bare chip is contained in an aluminum case coated with nickel plating. A beryllium foil with a thickness of 150 μm is used as its window.

Output current I of the photodiode is directly read out using a resistor of 50 Ω. Beam intensity F is calculated from the current as

$$F = \frac{W_{\mathrm{Si}}\, I}{e} \times \frac{1}{\omega} \times \frac{1}{R_{\mathrm{abs}}\, R_{\mathrm{att}}}, \tag{3.6}$$

where W_{Si} the W-value of Si, which is 3.66 eV, e the elementary charge, ω the X-ray energy, R_{abs} the absorption rate of the detector including its window, and R_{att} an attenuation rate of an aluminum plate. Figure 3.24 shows its absorption rate as a function of energy. The black line shows the rate with the window and the blue line shows without it. Both are obtained with GEANT4 simulation. The red line is a calculation using NIST data, and agrees with the simulation. The X-ray beam of BL19LXU is so strong to cause saturation of the output current of the photodiode. An aluminum plate with a thickness of 301 ± 1 μm is therefore used to attenuate the beam. Its attenuation rate R_{att} is conservatively calculated with a plate thickness of 300 μm, and is 8.5% for 9.5-keV X rays. If the photodiode is inclined against the beam axis, effective thickness of the attenuation plate becomes larger, and X rays are more attenuated by a factor of $\cos\theta^{-1}$. A typical tilting angle of, for example, $\theta = 3^\circ$ changes the rate by 0.1%. Thus a measured value becomes always conservative and is used in the analysis without this correction.

3.5.2 Intensity monitor during the run: PIN B

Another photodiode is also used to monitor the beam intensity at the shield. Figure 3.25 shows its picture. The same type of a bare chip is embedded in a lead cylinder with a diameter of 30 mm. This photodiode in lead also uses an attenuation plate of aluminum with the same thickness of 300 μm as a light-shielding window. The edge of the plate is shielded with a tape. Another lead cylinder with an aperture of 6 mm is fixed on it. The seam is also shielded with the shielding tape and is wrapped around with lead sheet to avoid photon leakage. Electron beam of the storage ring is sometimes aborted due to machine troubles. Its intensity is thus always monitored to check whether the beam is on. The data taken during the beam off is cut by off-line analysis.

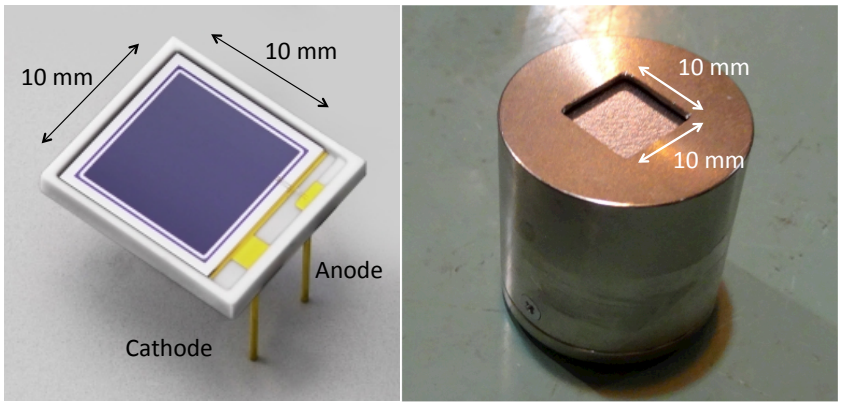

Figure 3.23: Silicon PIN photodiode. Left: the bare chip (Hamamatsu, S3590-09). Right: the bare chip is contained in an aluminum case coated with nickel plating for the light shielding (PIN A).

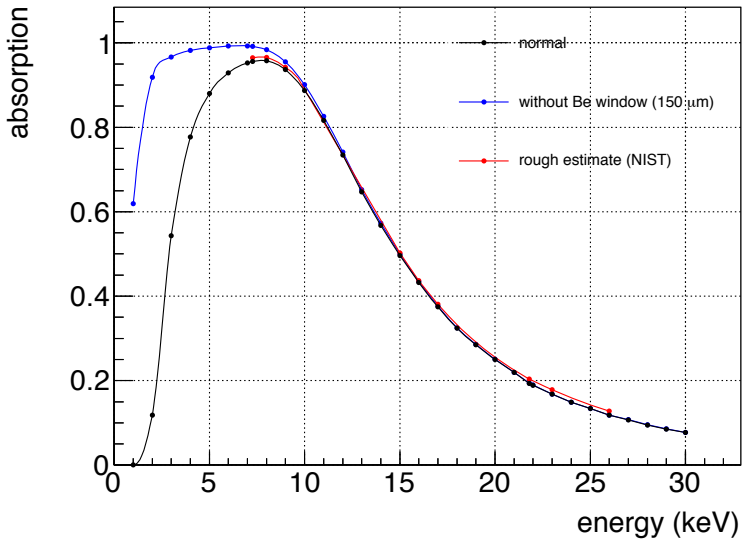

Figure 3.24: Absorption rate of the photodiode as a function of the X-ray energy. The black line shows the rate with the window and the blue line shows without it. Both are obtained with GEANT4 simulation. The red line is a calculation using NIST data.

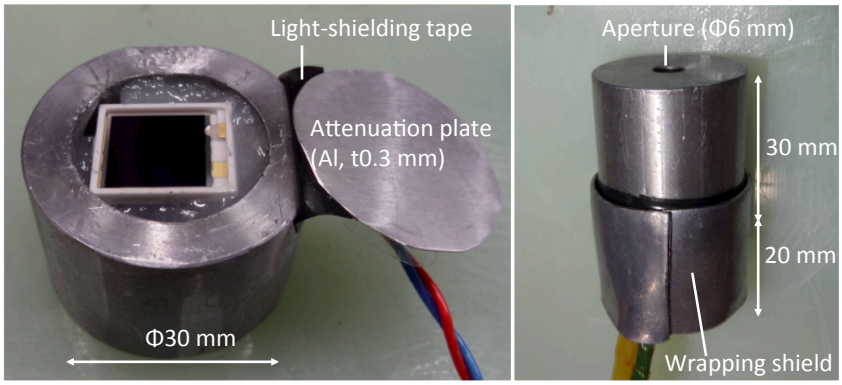

Figure 3.25: Another photodiode used to monitor the beam intensity at the shield (PIN B). The same type of a bare chip is embedded in a lead cylinder with a diameter of 30 mm. An aluminum plate with a thickness of 300 μm is used to attenuate the beam and to shield the light. Another lead cylinder with an aperture of 6 mm is fixed on it to avoid photon leakage.

Chapter 4

Run and analysis

In this chapter, data acquisition and its analysis is described. First, beamtime and procedure of the measurement is explained. Then the whole data is divided into sub-sets (data sets) and calculate the limit on $g_{a\gamma\gamma}$. Systematic uncertainties are also discussed.

4.1 Beamtime

Data acquisition run has been carried out at BL19LXU in SPring-8. Beamtime is assigned for a week from November 18 to 25 in 2015. The first two days of the beamtime are spent in preparation. It includes a setup of the magnets, the bank, and the detector, installing them into the hutch, and alignment of them on the beam axis. There are consecutive holidays in the middle of the beamtime. Delivery of the liquid nitrogen stopped for these days, and the period became a deadtime of the measurement. In order to release the hutch for the successive beamline user, our beamtime also includes a time for carry-out of the system from the hutch. After subtracting these non-measurable times, net time of the data acquisition becomes about two days.

4.2 Procedure of measurement

Procedure of the measurement is described as below.

- When surface level of liquid nitrogen becomes low, data acquisition and operation of the magnets are stopped.
- The hutch is opened and ventilated with large ventilators.
- The lead shield between the magnets (PIN B) is removed, and X-ray intensity is measured with a photodiode (PIN A) set in front of the detector.
- The shield (PIN B) is returned to its original position, and liquid nitrogen starts to be filled into the containers.

- When the surface level gets back to an operational level, operation of the magnets and data acquisition are started.
- When the surface level gets to the maximum height of the container, its filling is sopped.

4.3 Summary of run

4.3.1 Data set

Beam intensity is measured when the surface level of liquid nitrogen becomes lower. Once the nitrogen is filled up, it takes about 1–2 hours for the surface level to become lower again. The whole data is thus divided into sub-sets (data sets) on the occasion of the intensity measurement. A total of 35 data sets are obtained. Table 4.1 shows their summary.

Due to some malfunction of the trigger board, four fifth of the data is taken with a low charged voltage of 3.50 kV. The rest of the data is acquired with 3.75–4.00 kV operation. The $N_{\rm shot}$ is the number of shots during the data set. There are some data sets having a small number of shots. This is due to beam abort of the electron ring, which occasionally occurred during the measurement. The photon flux F has been converted from the current of PIN A described in the previous chapter. Intensity is measured between data sets. Thus each data set is sandwiched with two intensity measurements ($F_{\rm A}$ and $F_{\rm B}$). The center value and its uncertainty during the data set is calculated as $(F_{\rm A}+F_{\rm B})/2 \pm (F_{\rm A}-F_{\rm B})/2$. There can be seen a slight decrease fo the intensity over the whole measurements. The reason is considered to be a detune of the monochromator due to the continuous irradiation on its crystals for a week. The value of $I^4 t_{\rm tot} F$ represents a contribution to the sensitivity on the coupling constant $g_{a\gamma\gamma}$. It is again described in the following analysis. The value of $I^4 t_{\rm tot}/N_{\rm shot}$, on the other hand, represents its net contribution of the magnets per shot. It clearly shows an effectiveness of charging at a higher voltage. The total number of shots in the measurement is 13,838.

4.3.2 Field distribution

As a summary of the measurement, Fig. 4.1 shows field distribution of the most downstream magnet (magnet5) for the total 13,838 shots. The field is represented by a value at the center of the magnet. The first pulse is ranging from 8.1 T to 9.6 T, and the second pulse is from 5.5 T to 6.9 T. Due to heat loss of the first pulse, the second pulse is generated with a relatively smaller energy. This results in a decrease of the peak field of the second pulse.

As the field increase, the number of shots decreases for both the first and the second pulses. One reason for this is that 21% of the total shots is generated with a little higher voltage of 3.75–4.00 kV than 3.50 kV. This contribution is clearly seen as the gap of the first pulse around 8.5 T. On the other hand, both of the

Data set	V_c [kV]	N_{shot}	F [10^{13} photon/s]	$I^4\,t_{tot}\,F$ [10^{17} kA^4 photon]	$I^4\,t_{tot}/N_{shot}$ [10^1 kA^4 s]
1	3.50	239	3.48±0.16	1.35	1.62
2	3.50	73	3.32±0.00	0.40	1.63
3	3.50	330	3.33±0.01	1.80	1.64
4	3.50	431	3.29±0.04	2.31	1.62
5	3.50	505	3.27±0.02	2.67	1.62
6	3.50	305	3.29±0.01	1.61	1.60
7	3.50	506	3.28±0.03	2.69	1.62
8	3.50	562	3.18±0.07	2.91	1.63
9	3.50	526	3.10±0.02	2.65	1.62
10	3.50	390	3.14±0.03	1.99	1.63
11	3.50	456	3.08±0.03	2.28	1.62
12	3.50	336	3.07±0.02	1.73	1.67
13	3.50	523	3.08±0.02	2.63	1.64
14	3.50	398	3.04±0.02	1.98	1.63
15	3.50	481	2.85±0.17	2.28	1.66
16	3.50	36	2.54±0.15	0.15	1.67
17	3.50	249	3.04±0.01	1.25	1.65
18	3.50	356	3.05±0.01	1.77	1.63
19	3.50	397	3.05±0.01	1.96	1.62
20	3.50	504	3.04±0.01	2.46	1.61
21	3.50	325	3.02±0.01	1.58	1.61
22	3.50	184	3.06±0.05	0.91	1.62
23	3.50	381	3.13±0.02	1.94	1.63
24	3.50	592	3.14±0.00	3.09	1.66
25	3.50	464	3.02±0.12	2.38	1.70
26	3.50	368	2.98±0.08	1.88	1.71
27	3.50	317	3.10±0.04	1.68	1.71
28	3.50	705	2.62±0.01	3.51	1.90
29	3.75–4.00	298	2.72±0.09	1.70	2.09
30	3.75	418	2.75±0.06	2.34	2.04
31	3.75	471	2.58±0.11	2.26	1.86
32	3.75	483	2.35±0.12	2.11	1.86
33	3.75	428	2.86±0.01	2.29	1.87
34	3.75	444	2.84±0.01	2.37	1.89
35	3.75	357	2.83±0.00	1.90	1.88
Total		13,838		70.8±0.3	

Table 4.1: Data sets

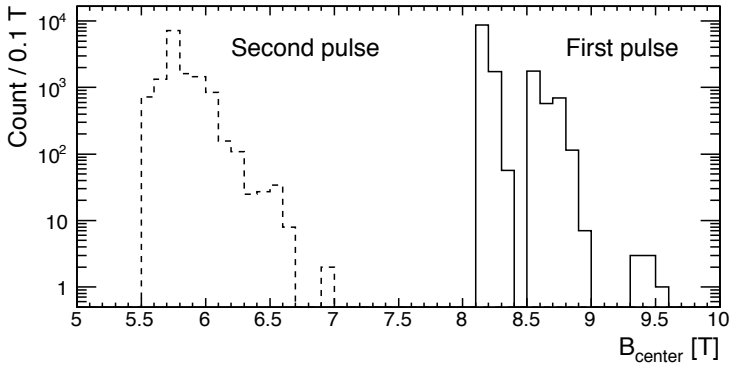

Figure 4.1: Field distribution of the most downstream magnet for the total 13,838 shots. The field is represented by a value at the center of the magnet. The first pulse is ranging from 8.1 T to 9.6 T, and the second pulse is from 5.5 T to 6.9 T. Due to heat loss of the first pulse, the second pulse is generated with a relatively smaller energy. This results in a decrease of the peak field of the second pulse.

separated distributions of the first pulse still show the falling behavior with respect to an increase of the field. This is due to a transient phenomenon, which lasts until the coil temperature reaches a thermal equilibrium. As an example, Fig. 4.2 shows change of the field measured at the beginning of the 29th data set. The first shot generates 9.4 T, and then the field decays exponentially. The decay lasts until it reaches a thermal equilibrium around 8.7 T. Fitting of the data points other than the first shot gives its time constant to be 2.3 shots. Since the shot repetition of this data set is about 0.09 Hz, it corresponds to a time constant of 26 s. This seems to be contrary to the time constant shown in Chapter 2. The reason is, however, clear since most of the temperature increase is completed at the first shot. This can also be seen as an isolated structure in Fig. 4.1 around 9.5 T for the first pulse and around 7 T for the second pulse.

4.4 Event timing

Timing information of an event at the detector is recorded and expressed as an elapsed time from the latest shot. Figure 4.3 shows the time spectrum of all events. The top figure shows its long time view. The counts decrease rapidly at about 10 s. This is consistent with the fact that most of the data sets are operated with a shot repetition of about 0.1 Hz. The first several data sets are operated with a relatively slow shot repetition of $\sim$0.07 Hz for conditioning. These data give the

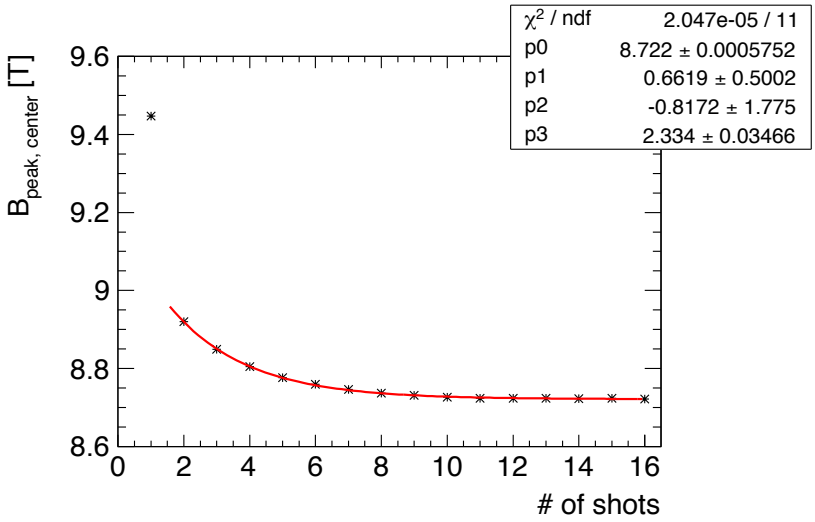

Figure 4.2: Change of field of the most downstream magnet, measured at the beginning of the 29th data set. The field is represented by a value at the center of the magnet. The first shot generates 9.4 T, and then, the field decays exponentially. The decay lasts until it reaches a thermal equilibrium around 8.7 T.

counts around 13±3 s. Events hitting the detector during the field can be signal candidates, and the rest of unsynchronized events are cut off. The bottom figure shows a magnified view around the first 100 ms. The duration of a shot is about 2 ms. This corresponds to the leftmost bin in the figure. It contains one event, which hit the detector at 1.8 ms, the end of the second pulse. The other events spread uniformly and do not show any peculiar structure.

4.5 Energy spectrum

Figure 4.4 shows a measured energy spectrum of all events. Energy threshold is set around 3 keV. The black spectrum shows unsynchronized events which occurred in 8 s from the latest shot. The red one shows the synchronized event, and its energy is 4.8 keV. Since these two spectra are normalized with time, the large time difference between the signal (∼2 ms) and the background (8 s) makes any synchronized event out of the figure. Therefore, signal strength of synchronized events is taken to be 1/100 for visibility. The second event hits the detector at 8.3 ms and the total number of unsynchronized events are 1,521 from 0 keV to 16 keV. These give an estimated count to be observed from 1.8 ms to 8.3 ms. The count is 0.96 ± 0.62 and is self-consistent with the observed one event.

Energy resolution of the detector is 93 eV (σ) at the beam energy of 9.5 keV

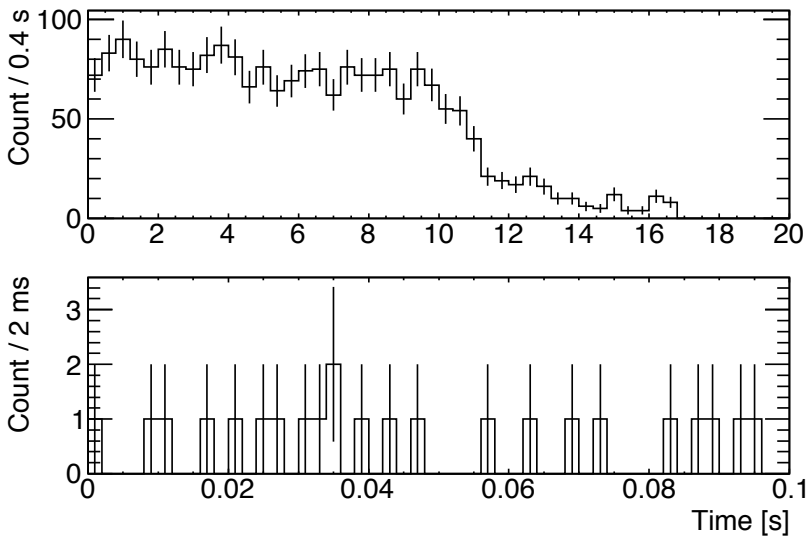

Figure 4.3: Time spectrum of all events. The origin of the time is defined by the latest shot. Top: the long time view. The counts decrease rapidly at about 10 s since most of the data sets are acquired with a shot repetition of about 0.1 Hz. Bottom: the magnified view around the first 100 ms. The duration of a shot is about 2 ms. This corresponds to the leftmost bin in the figure. It contains one event, which hit the detector at 1.8 ms, the end of the second pulse.

(Fig. 3.18). This gives a signal region of $\pm 2\sigma$ to be 9.5 ± 0.2 keV, which is also shown in the figure. Any candidate is not observed in the region.

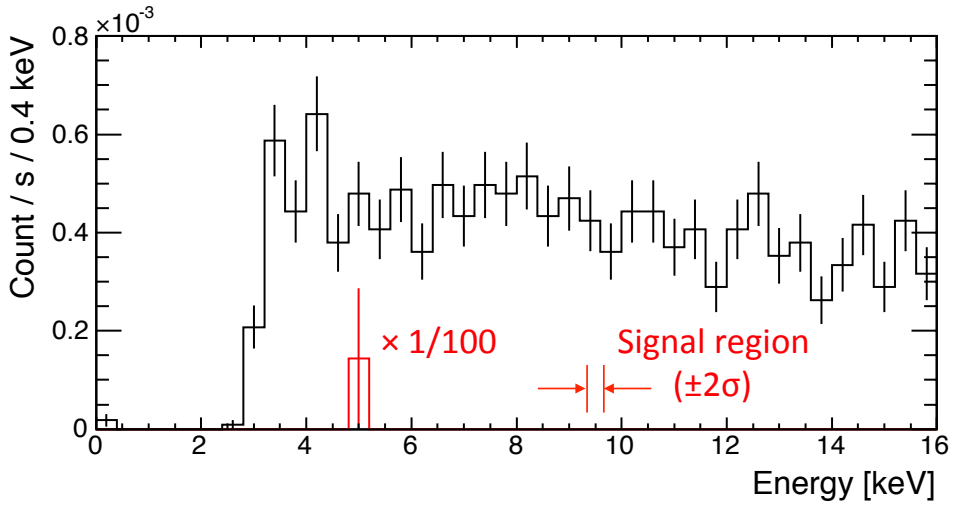

Figure 4.4: Measured energy spectrum of all events. Energy threshold is set around 3 keV. The black spectrum shows unsynchronized events which occurred in 8 s from the latest shot. The red one shows the synchronized event, and its energy is 4.8 keV. The two spectra are normalized with time, and signal strength of synchronized events is taken to be 1/100 for visibility.

4.6 Constraining the coupling constant

Since the field (and its current) changes with time (Fig. 4.5), the conversion probability also depends on time. Equation (1.11) is thus rewritten as

$$N = \eta \int_0^{t_{\rm tot}} P_{\gamma\to a}(t)\, P_{a\to\gamma}(t)\, F\, dt, \tag{4.1}$$

where $P_{\gamma\to a}(t)$ the conversion probability of upstream region, $P_{a\to\gamma}(t)$ that of downstream region, F the photon flux in s^{-1}, and $t_{\rm tot}$ the total pulse duration summed up over all shots. Correspondingly, the conversion probability of Eq. (1.12) is rewritten as

$$P_{\gamma\to a}(t) = P_{a\to\gamma}(t) = \frac{g_{a\gamma\gamma}^2}{4} \frac{\omega}{\sqrt{\omega^2 - m_a^2}} \left| \int B(z,t)\, e^{iqz}\, dz \right|^2 \tag{4.2}$$

with $B(z,t)$ as a function of space and time.

Here the beam energy is 9.5 keV. Detection efficiency at the energy is obtained to be $89 \pm 1\%$ from Fig. 3.19. The photon flux and total pulse duration are listed in Tab. 4.1. The air in the beam pipe is evacuated, and the pressure is monitored

during the run. It is better than 10 Pa. From Eq. (1.14), this gives an effective photon mass of 7 meV. The null observation gives the number of signal events to be 2.96 at 95% confidence level ($N_{95\mathrm{CL}}$). Both conversion probabilities depend on the field maps. They are scaled from Fig. 2.11 using field-current ratio at high voltages shown in Fig. 2.7. The resulting maps are shown in Fig. 4.6 with the pictures. Their spacing is 417 ± 1 mm. These values are listed in Tab. 4.2.

Although these magnets have slightly different maps with each other, their input current is common since they are serially connected with cables. The current transformer reads the sum of the upstream and the downstream currents ($I_{\mathrm{sum}} = I_{\mathrm{u}} + I_{\mathrm{d}}$). The ratio of the two currents (I_{u} and I_{d}) are measured by passing each cable through the hole. Figure 4.7 shows the measured currents and their difference with respect to a charged voltage. Each current is almost exactly half of the total current and their difference is less than 1%.

Parameter	Value
Photon energy ω	9.5 keV
Detection efficiency η	0.89 ± 0.1
Effective photon mass m_γ	7 meV
Signal events at 95% C.L. $N_{95\mathrm{CL}}$	2.96
Photon flux F	see Tab. 4.1
Total pulse duration t_{tot}	see Tab. 4.1
Field $B(z,t)$	see Fig. 4.6 and Fig. 4.5

Table 4.2: Parameters used to calculate the limit

Since the t and z are integrated independently, right side of Eq. (4.1) can be rewritten as

$$\eta \frac{g_{a\gamma\gamma}^4}{16} \frac{\omega^2}{\omega^2 - m_a^2} \int_0^{t_{\mathrm{tot}}} \left(\frac{I_{\mathrm{sum}}(t)}{2}\right)^4 F\, dt \left| \int (B/I)_{\mathrm{u}}(z)\, e^{iqz}\, dz \right|^2 \left| \int (B/I)_{\mathrm{d}}(z)\, e^{iqz}\, dz \right|^2 . \tag{4.3}$$

The first integral is calculated by using a sum of the two currents ($I_{\mathrm{sum}}(t)$) recorded by each shot. It has already been listed as $I^4 t_{\mathrm{tot}} F$ for each data set in Tab. 4.1. The second and the third integral are calculated from the maps of the upstream and downstream region ($(B/I)_{\mathrm{u}}(z)$ and $(B/I)_{\mathrm{d}}(z)$, Fig. 4.6).

4.7 Systematic uncertainties

Before the limit is calculated, various sources of systematic uncertainties are studied here. They are calculated as the change of $g_{a\gamma\gamma}$ in its flat region below $\simeq$0.1 eV. They are summarized in Tab. 4.4

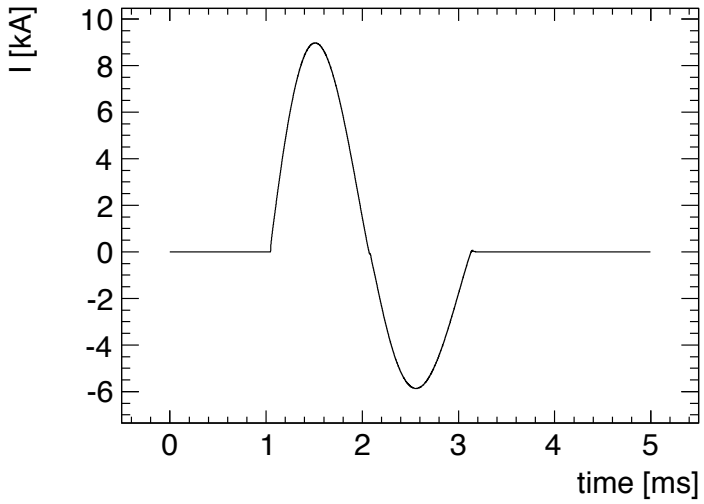

Figure 4.5: Current shape of a shot with four magnets ($I_{\mathrm{sum}}(t)$) operated with a charged voltage of 3.75 kV. NOTE that the vertical value has been attenuated with an attenuator of -10 dB.

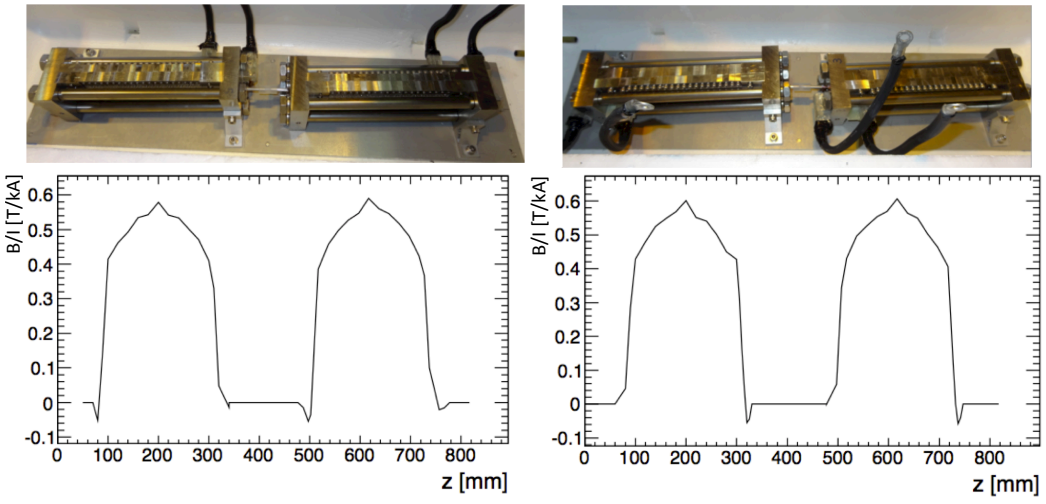

Figure 4.6: Field maps of the upstream (I_{u}, left) and the downstream (I_{d}, right) regions. The spacing between the two magnets is 417 ± 1 mm. The maps are scaled from Fig. 2.11 using field-current ratio at high voltages shown in Fig. 2.7.

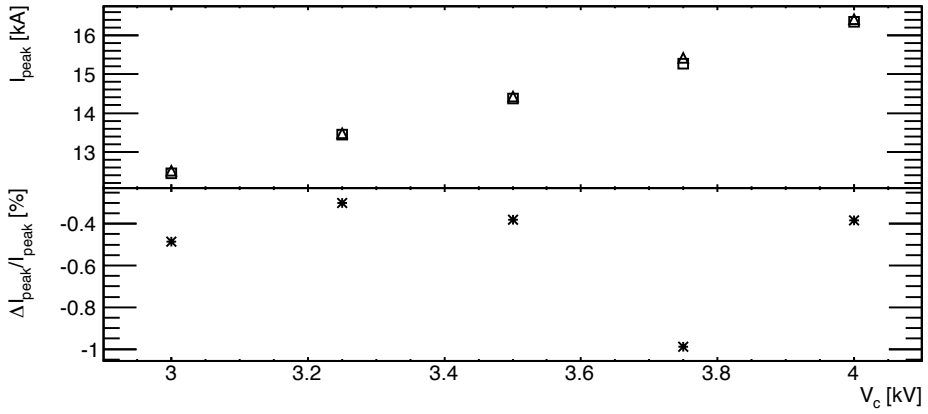

Figure 4.7: Ratio of the two currents ($I_\mathrm{u}/I_\mathrm{d}$) as a function of charged voltage. Top: the measured currents of the upstream (triangle) and the downstream (box) magnets. Bottom: the difference of the two currents. Their difference is less than 1%.

4.7.1 Small uncertainties

Uncertainty of the photon flux is estimated from the different two measurements between before and after the data set, and is shown in Tab. 4.1. Its contribution is included in the calculation of $I^4 t_\mathrm{tot} F$. Since measurements of each data set are independent, their quadrature sum gives $(70.8 \pm 0.3) \times 10^{17}\,\mathrm{kA}^4$ photon. $g_{a\gamma\gamma}$ depends on the fourth root of $I^4 t_\mathrm{tot} F$, and its uncertainty becomes 0.1%.

Another systematic error comes from the detection efficiency. It arises from uncertainty of the thickness of the surface dead layer shown in Fig. 3.19. The detection efficiency is found to be 89 ± 1%. Since $g_{a\gamma\gamma}$ depends on the fourth root of the efficiency, its uncertainty becomes 0.4%.

The field-current ratio slightly changes with its charged voltage. The uncertainty of each magnet is shown in Fig. 2.7. Since $g_{a\gamma\gamma}$ linearly depends on this, their quadrature sum gives the second largest uncertainty of 1.2%.

Accuracy of map measurements also affects $g_{a\gamma\gamma}$. Since the flat region of $g_{a\gamma\gamma}$ linearly depends on the field-length product, a value obtained by the space integral of the map is concerned. Integrals of two measured maps in Fig. 2.9 give their difference to be ± 0.9%.

Contributions from the magnet spacing (Fig. 4.6, 417 ± 1 mm) and current ratio (<1%) are evaluated by changing the parameters of the $g_{a\gamma\gamma}$ calculation. Although phase of the conversion probability changes with respect to the magnet spacing, contribution from that appears at extremely high mass region of $g_{a\gamma\gamma}$. Any changes are thus not observed for the low mass region. Significant contribution from a slight change of the current ratio is also not confirmed. The reason for this is that if the current of one side increases, that of the other side decreases. $g_{a\gamma\gamma}$ depends on the

product of both probabilities, and the resulting changes becomes so small.

4.7.2 Temperature increase at thermal equilibrium

During repetitive operation, temperature of the coil becomes higher than a liquid-nitrogen temperature of 77 K and reaches an equilibrium temperature. Temperature dependence of parameters are described here.

Temperature increase of the coil causes i) an increase of field length along the beam axis, ii) an increase of the inductance, and iii) an increase of the resistance of the coil. i) and ii) are caused by the geometrical deformation of the coil due to the thermal expansion. iii) is caused by the temperature dependence of the resistivity of copper.

Expansion of the field length

The temperature increase of the coil is estimated from the current shape. The resistance component of the magnet changes a sinusoidal shape of ideal LC oscillation into a LCR dumpling oscillation. Its shape is written as

$$I(t) = I_0 \, \frac{\omega_0}{\omega} \, \exp\left(-\frac{R}{2L} \, t\right) \sin\omega \, t, \tag{4.4}$$

where $I_0 = V_0\sqrt{C/L}$, $\omega_0 = 1/\sqrt{LC}$, and $\omega = \omega_0\sqrt{1-\gamma^2}$ ($\gamma = R/2\sqrt{C/L}$). Fitting is carried out for a current shape at thermal equilibrium of 3.75 kV and 0.12 Hz operation, which gives a heating of about 0.5 kW. The resistance of one magnet is obtained to be 25 mΩ. Coil temperature at the thermal equilibrium is calculated from the temperature dependence of resistivity of copper

$$\rho(T) = -3.14 \times 10^{-9} + 7.2 \times 10^{-11} \times (T \text{ [K]}). \tag{4.5}$$

The resistance corresponds to $T \equiv T_0 + \Delta T = (77 + 115)$ K.

Although thermal expansion of the coil is suppressed by its backup metals, expansion of a free coil (i.e. without backup metals) is assumed here. Expansion of a free coil is calculated from the coefficient of thermal expansion of copper, which is 16.8×10^{-6} K^{-1}. This increases the longitudinal length of the coil (200 mm) by 0.2%. The increase of the field volume causes an increase of the inductance and therefore decreases the current. Its contribution to $g_{a\gamma\gamma}$ is included in the calculation of measured current shapes at thermal equilibrium and is described in the next sub-section. The field-current ratio, on the other hand, does not change with this longitudinal expansion. The product of the field-current ratio and the coil length, which linearly affects $g_{a\gamma\gamma}$, thus increases by 2%. The extreme assumption of a free coil gives better result on $g_{a\gamma\gamma}$ and here this contribution is conservatively neglected.

Difference of the two currents

The two cases of (ii) and (iii) are the change of circuit parameters, R and L. If these values at thermal equilibrium are different between upstream and downstream magnets, they give different shapes of current ($I_{\rm u}(t) \neq I_{\rm d(}t{\rm)}$). Here two changes are conceivable; current ratio and time scale. The ratio of the two currents becomes unbalanced when there is abnormal temperature rise in either upstream or downstream magnets. This is caused by the difference between the two resistance components ($R_{\rm u}$ and $R_{\rm d}$). Change of the time scale between the two currents, on the other hand, is caused by the difference between the two inductance components ($L_{\rm u}$ and $L_{\rm d}$).

Since only the sum of the two currents are read out and used in the analysis, additional measurements are carried out to measure $I_{\rm u}(t)$ and $I_{\rm d}(t)$ separately. Each of them at thermal equilibrium are read out one by one with the same setup of the run. The magnets are operated with 3.75 kV and 0.12 Hz, which gives the largest heating among all the data sets and therefore would give the largest changes. $I_{\rm u}(t)$ and $I_{\rm d}(t)$ are compared with a half of $I_{\rm sum}(t)/2$, which has been measured during the run. The results are summarized in Tab. 4.3. Circuit parameters obtained from the fitting of current shapes using Eq. (4.4) show good agreements other than a slight difference of resistance component of the downstream ($R_{\rm d}$).

Both contributions from the changes of magnitude and time scale of the two currents are directly calculated with an integral of $I_{\rm u}$ and $I_{\rm d}$. The contribution from the difference between the two currents, which linearly affects $g_{a\gamma\gamma}$, is obtained as

$$1 - \left(\frac{\int_0^{t_1} I_{\rm u}(t)^2 \, I_{\rm d}(t)^2 \, {\rm dt}}{\int_0^{t_1} \left(\frac{I_{\rm sum}(t)}{2} \right)^4 \, {\rm dt}} \right)^{1/4} = 0.3\%, \tag{4.6}$$

where t_1 a period of one shot.

Current	R [mΩ]	L [μH]	$I_{\rm max}$ [kA]
$I_{\rm sum}/2$	51.2	69.9	14.6
$I_{\rm u}$	51.4	69.8	14.6
$I_{\rm d}$	49.8	69.9	14.7
$(I_{\rm u} - I_{\rm sum}/2)/(I_{\rm sum}/2)$	+0.3%	−0.1%	0.0%
$(I_{\rm d} - I_{\rm sum}/2)/(I_{\rm sum}/2)$	−2.8%	0.0%	+0.4%

Table 4.3: Circuit parameters obtained by fitting the current shapes (Eq. (4.4)).

4.7.3 Alignment of the magnets

The largest systematic error comes from the uncertainty of beam path. Although it has been assumed until now that the beam path coincides with the center path,

the beam path can be different from the center path. In this case, the field *at the beam* also becomes different. This contribution is estimated with the worst case, in which the path gives the lowest field-length product. The inner diameter of the 1/4-inch-pipe is 5.35 mm. On the other hand, during the run, the margin of alignment has been checked by shifting the height or the translation of the four magnets until the beam intensity starts to decrease. In this way, the beam margin is measured to be ±0.45 mm. Taking the beam size of ∼1.0 mm (Fig. 3.7) into account, conceivable deviation of the *beam center* from the *pipe center* is 1.7 mm. Since most of the photons are contained in ±0.3 mm region from the beam center (see again Fig. 3.7), estimation of the largest deviation is taken as 2.0 mm. The field map of the transverse direction along the X-ray polarization is calculated with 3D finite element simulation and is shown in Fig. 4.8 at the central cross section of the magnet. The 30 boxes are the cross section of the Cu wire with its height of 3.0 mm. The bottom of the figure shows the field along the x direction. Its horizontal scale corresponds to the actual length of the top figure. The central region of -4 mm $< x < +4$ mm is the field volume between the innermost wires. The field at $x = 0$ is the lowest since this point is the farthest from the innermost wires. Deviation in this direction thus receives the stronger field. On the other hand, deviation in the y direction contributes to decrease of the field when it goes beyond the uniform region (yellow). The worst path can be found on the symmetrical plane, which divides the left and the right of the figure, since the farthest points from the innermost wires are located on this plane. The path goes into the pipe with a deviation of +2.0 mm from the pipe center along the y direction, passes through the center, and goes out with a deviation of −2.0 mm. Figure 4.9 shows maps of the path through the pipe center (red) and the above worst path (blue). These two integrals (i.e. the field-length products) give their difference of 6.4%.

Parameter	Value
Photon flux (Tab. 4.1)	±0.1%
Detection efficiency (Tab. 3.19)	±0.4%
Field-current ratio vs V_c (Fig. 2.7)	±1.2%
Map measurement (Fig. 2.9)	±0.9%
Magnet spacing (Fig. 4.6)	< ±0.1%
Current ratio vs V_c (Fig. 4.7)	< ±0.1%
Thermal expansion of coils	< ±0.1%
Difference between I_u and I_d at T_{eq} (Eq. (4.6))	±0.3%
Deviation of beam path (Fig. 4.9)	+6.4%
Total	$^{+6.5\%}_{-1.6\%}$

Table 4.4: Systematic uncertainties

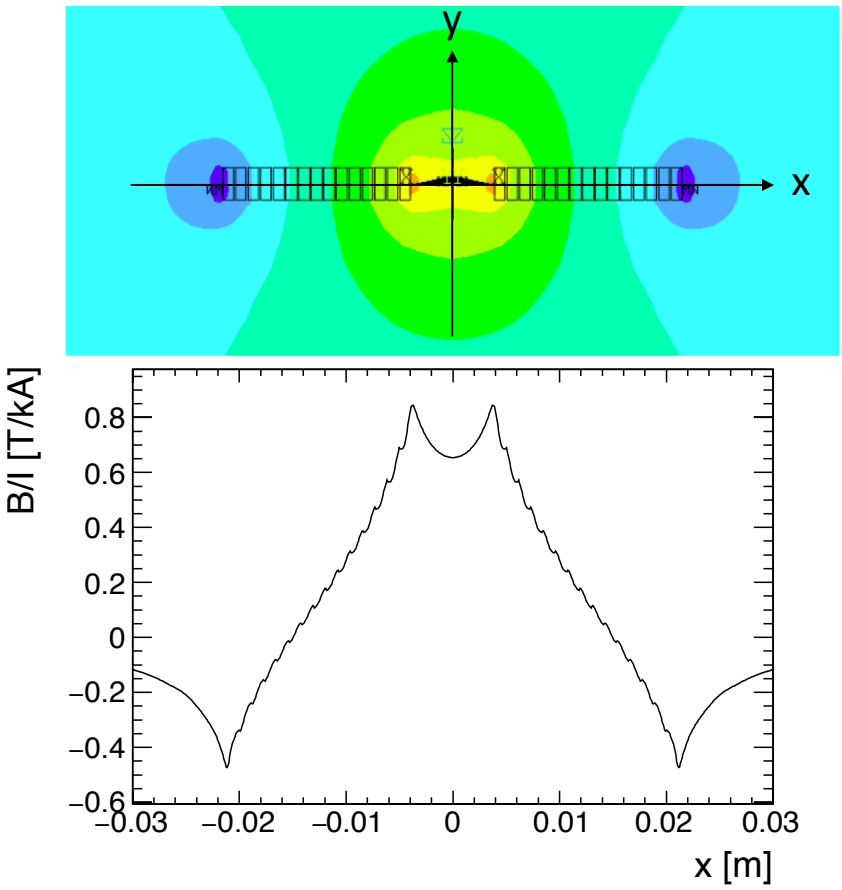

Figure 4.8: Top: the field map of the transverse direction along the X-ray polarization at the central cross section of the magnet (simulation). The 30 boxes are the cross section of the Cu wire. The height of the wire is 3.0 mm, and the center region (yellow) has a good uniformity of the field. Bottom: field along the x direction. Its horizontal scale corresponds to the actual length of the top figure. The central region of -4 mm $< x < +4$ mm is the field volume between the innermost wires.

4.8 Limit

The limit on $g_{a\gamma\gamma}$ obtained from this experiment is shown in Fig. 4.10 as a red line. The black lines are limits from previous searches. For the high mass region, two structures are observed; oscillation and dumping. The oscillation of the sensitivity is caused by a short oscillation length ($= q^{-1}$) compared with the field length ($\sim$20 cm). The dumping of the sensitivity comes from the momentum mismatch between an incident or an outgoing photon and ALP. Although they give different structures, they have the same origin; a large m_a. Such oscillation or momentum mismatch, on the other hand, do not occur for the low mass region below 0.1 eV. Therefore, the sensitivity for this region becomes flat.

The result is represented for the flat region below $\simeq$0.1 eV as

$$g_{a\gamma\gamma} < (2.36\,^{+0.15}_{-0.04}(\text{sys.})) \times 10^{-4}\ \text{GeV}^{-1} \tag{4.7}$$

In Eq. (4.7), taking 2.96 events from the null result is already quite conservative. Therefore, a value one-standard-deviation-smaller than the central value is used as the 95% C.L. result including the systematic uncertainties,

$$g_{a\gamma\gamma} < 2.51 \times 10^{-4}\ \text{GeV}^{-1},\ 95\%\,\text{C.L.} \tag{4.8}$$

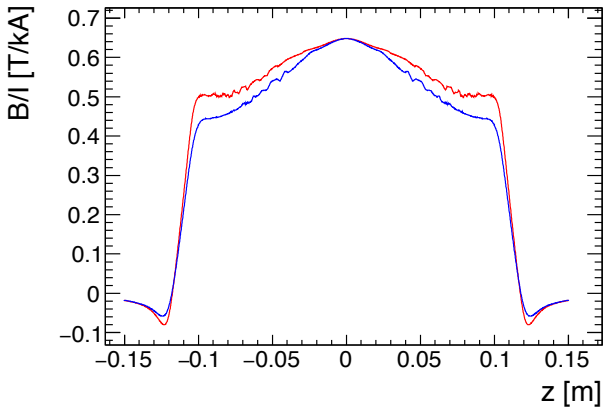

Figure 4.9: Uncertainty from the deviation of the beam path. Maps of the path through the pipe center (red) and the worst path (blue), which deviates from the path through the pipe center by 2.0 mm. These two integrals give their difference of 6.4%.

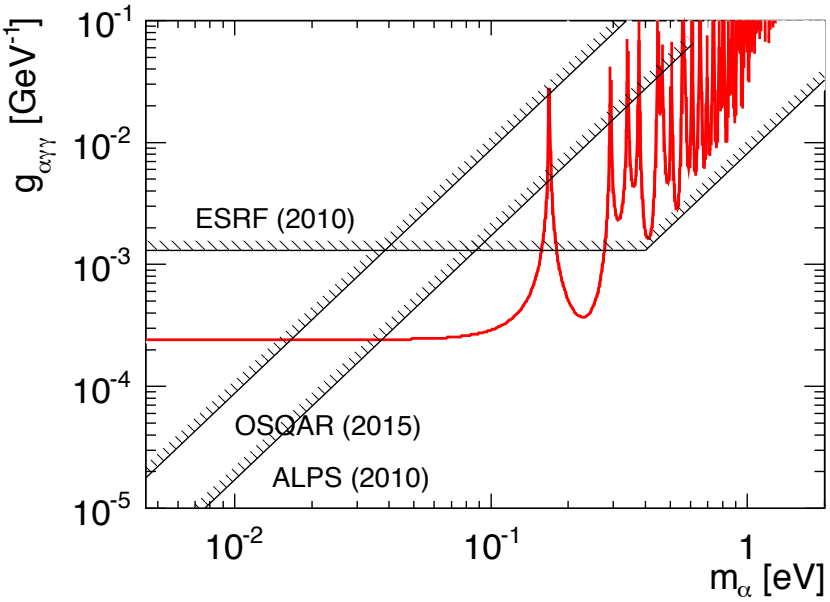

Figure 4.10: Limit on $g_{a\gamma\gamma}$ at 95% C.L. obtained by this search (red). The black lines are limits from previous searches. ALPS and OSQAR are LSW experiments using an optical laser and long dipole magnets. ESRF is a search carried out at an European Synchrotron Radiation Facility using two superconducting solenoids with their maximum field of 3 T.

Chapter 5

Discussion and prospect

In the first section of this chapter, the limit obtained in the previous chapter is compared with the other limits. The physical significance of the result is then described. In the third section, upgrades of the magnets and of the LSW limit are described.

5.1 Comparison with previous LSW limits

The previous limits are shown in Fig. 4.10 as black lines. They are compared with the limit obtained in the previous chapter.

5.1.1 Laser LSW limits

ALPS [37] and OSQAR [38] are LSW experiments using an optical laser as their light source. The OSQAR limit was recently published in 2015. It is more stringent by $\sim$2 times than that of the ALPS for the flat region below 0.2 meV. Since they used two long dipoles with each length of 14.3 m, their sensitivity for higher mass is surpassed by that of ALPS using one dipole of 8.8 m with a shield placed in the middle. The ALPS experiment builds up the laser intensity of the $\gamma \to a$ conversion region by using a Fabry Perot cavity. The build-up factor is 300. Thus using a relatively shorter magnet than those of the OSQAR, they achieved a high sensitivity.

On the other hand, their laser wavelength gives the photon energy of 2.3 eV. From Eq. (1.13), ALP mass searched by the LSW experiment is proportional to the square root of the photon energy. Since the photon energy is 9.5 keV, the search has sensitivity for the 64 times heavier mass region from only this energy relation. Although the world's strongest X-ray beam is used in this experiment, the photon flux itself is smaller by many orders of magnitude than those laser search. This is one of the reasons which make the sensitivity to $g_{a\gamma\gamma}$ relatively weaker.

The present limit crosses these laser limits around 30 meV. This region corresponds to an extremely high mass region for the two limits, and dumping oscilla-

tion makes unsure about the validity of their sensitivities for this region. Thus the present limit is also considered to hold a significance below ∼0.03 eV.

5.1.2 An X-ray LSW limit

In addition to these optical searches, experiments with other light sources have recently been carried out to cover the wider range of the ALP mass. A pioneering search using X-ray beams has been carried by *Battesti et al.* [40] as the BMV project. They used 50.2 keV and 90.7 keV X-ray beams of synchrotron radiation at ESRF (European Synchrotron Radiation Facility). Two superconducting solenoids are used at their maximum field of 3 T. It is the first LSW search using X rays as a light source.

As a comparison with the same X-ray LSW search, our result improves their limit by factor 5.2 at the masses below ∼0.1 eV. Most of the gain comes from the field-length product of the magnets.

5.1.3 Another terrestrial search

As an ALP search, the NOMAD collaboration also published a similar result below ∼0.1 eV in 2000 [74]. The main target of the NOMAD experiment is to detect tau neutrino appearance. They re-analyzed the data collected in 1996 and obtained the limit. This is a pioneering work to search for ALPs using a high energy accelerator. However, some uncertainties seem not to be taken into the consideration. They are:

- uncertainties of the γ-ray flux, which come from i) the measurement of the absolute flux, ii) effect of the energy spectrum at the low energies, and iii) direction of the ALP flux,
- background estimation at low energies and signal excess of 1.6σ,
- material effect of $\gamma \to a$ conversion region in the target drift chamber.

Thus the direct comparison of limits is restricted only to the dedicated LSW experiments to avoid confusion.

5.2 Physical significance of the result

This section describes the physical significance of the present result with respect to the each motivation shown in the introduction (Chapter 1).

5.2.1 Significance to the general motivation

Since the mass and the coupling of ALPs are not bound, a search for new parameter space in the mass-coupling place has importance. The present result newly excludes the possibility of $g_{a\gamma\gamma}$ stronger than 2.5×10^{-4} GeV^{-1} below ∼0.1 eV for the first time as an LSW search. It confirms that there are no new physics with 95% C.L.

5.2.2 Significance to the interests of X-ray terrestrial experiments

Powerful X-ray sources can be found in the Sun or in a synchrotron radiation facility. Thus the two have a good complementary relation. In terms of the possible solutions to some solar problems with ALP mass of 10–20 meV, the region has been covered with spikes of oscillations of the optical limits before the present result. The present limit excludes this possibility up to $g_{a\gamma\gamma} = 2.4 \times 10^{-4}$ GeV^{-1} at 95% C.L.

Astrophysical bounds are valid only if the ALPs escape from the Sun without any further interaction. Their mean free path λ_a of the Primakoff conversion is given by [75]

$$\lambda_a = \Gamma_{\gamma\to a}^{-1} \tag{5.1}$$

$$\Gamma_{\gamma\to a} = \frac{g_{a\gamma\gamma}^2 T \kappa_s^2}{32\pi}\left[\left(1+\frac{\kappa_s^2}{4E^2}\right)\ln\left(1+\frac{4E^2}{\kappa_s^2}\right)-1\right], \tag{5.2}$$

where T the temperature, κ_s the screening scale [75], and E the photon energy. For 4 keV ALPs with $T \approx 1.3$ keV and $\kappa_s \approx 9$ keV at the solar center, it becomes $\lambda_a \approx g_{a\gamma\gamma}^{-2}\, 8 \times 10^{-7}\, R_\odot$ [65]. This corresponds to

$$0.9 \times 10^{-3}\ \text{GeV}^{-1} < g_{a\gamma\gamma} < 1.3 \times 10^{-3}\ \text{GeV}^{-1} \tag{5.3}$$

for $R_\odot/2 < \lambda_a < R_\odot$. This assumes the environment of the solar center for the entire volume of the Sun, and thus Eq. (5.3) is relatively conservative. The region has not been ruled out by the previous X-ray LSW search. The present limit *experimentally* excludes this possibility up to ∼0.1 eV. This would provide a good cornerstone for the previous astrophysical bounds.

5.3 Upgrades

Feasibility of using pulsed magnets for an X-ray LSW experiment has been demonstrated in this thesis. This section describes the original goal of this experiment, which uses pulsed beam from SACLA. Some improvements of magnet operation are explained from the experience of the present experiment. The expected sensitivity is then calculated.

5.3.1 Improvements of magnet operation

The number of magnets

The current capacity of the present bank is designed to operate eight magnets. As shown in Tab. 2.1, each magnet has a body length of 350 mm, and the total length of eight magnets becomes 2.8 m. An experimental hutch in SACLA has an inner width of about 4 m. Thus it is possible to place eight magnets in a hutch.

The present experiment uses four magnets. Since $g_{a\gamma\gamma}$ linearly depends on field length, eight magnets give a gain on $g_{a\gamma\gamma}$ by a factor of two.

Charged voltage

Repetition field is confirmed to be safe up to 9.5 T as described in Sec. 2.3.6. The durability test has been carried out with a charged voltage of 4.0 kV. On the other hand, most of the present magnets have been operated with a field around 8.3 T for the first pulse as shown in Fig. 4.1. This is because most of the data set have been operated with a lower charged voltage of 3.5 kV (Tab. 4.1), due to malfunction of the trigger board, which appeared at 3.75–4.0 kV. This trouble is considered to originate from a different noise environment between the durability test and the present experiment at SPring-8. If the trouble is fixed, magnets are operated with 4.0 kV as planned. The field gain thus becomes a factor of 1.14. Since $g_{a\gamma\gamma}$ linearly depends on field, it gives a gain on $g_{a\gamma\gamma}$ by the same factor.

Connection of magnets

Left of Fig. 5.1 shows the present serial connection of two magnet. The total inductance becomes double, and the pulse width becomes larger by a factor of $\sqrt{2}$ when it is compared with one magnet. Since the heat loss scales to the pulse width, this results in a smaller repetition by the same factor. Instead, the serial connection reduces the voltage on each magnet by half and hence does not require a high withstand voltage to the magnets.

If two magnets are connected in parallel, the opposite results are obtained (right of the Fig. 5.1); the total inductance becomes half and the heat loss decreases whereas the withstand voltage of each magnet is required to be double. The present magnets are designed to have a withstand voltage of 4.9 kV, and can be operated with parallel connection at 4 kV. It results in an increase of repetition by a factor of two when it is compared with the present serial connection. Since $g_{a\gamma\gamma}$ depends on the fourth root of repetition, it gives a gain on $g_{a\gamma\gamma}$ by a factor of 1.19.

5.3.2 XFEL SACLA

The present LSW setup uses pulsed magnets and DC X rays at SPring-8. If pulsed X rays from SACLA is used, a better sensitivity on $g_{a\gamma\gamma}$ is obtained. Light source performance of SACLA is summarized in Tab. 5.1. If the same run time as the present experiment of two days is assumed, the gain factor on $g_{a\gamma\gamma}$ from using SACLA is expressed as

$$\left(\frac{N_{\mathrm{SACLA}}}{\frac{3}{8}\, F_{\mathrm{BL19}}\, \Delta t} \right)^{1/4} = 2.05, \tag{5.4}$$

where 3/8 a DC factor, which comes from the time integral of fourth power of the sinusoidal field shape, $F_{\mathrm{BL19}} = 3 \times 10^{13}$ photon/s the X-ray flux at BL19LXU (Tab. 4.1), $\Delta t = 2$ ms the pulse width of the field, and $N_{\mathrm{SACLA}} = 4 \times 10^{11}$ photon/pulse the number of photons contained in a pulse.

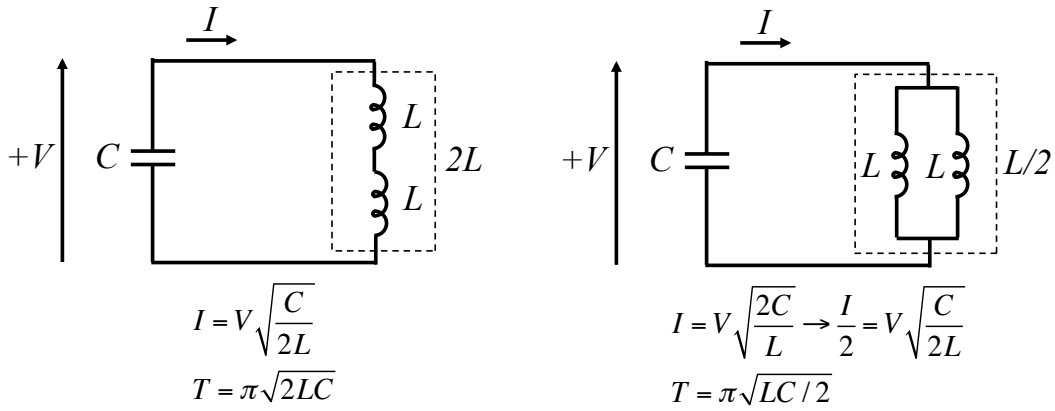

Figure 5.1: Difference of the connection between series and parallel. Left: the present serial connection of two magnets. Right: parallel connection of two magnets. Both connections give the same current for each magnet. The withstand voltage of the parallel magents is required to be double than that of the serial magnets. Instead, the pulse width T is smaller by a factor of two, reducing the heat loss and increase the repetition by the same factor.

Parameter	value
Energy	$\sim$10 keV (variable)
Intensity (max)	4×10^{11} photon/pulse
Beam size	$\sim$100 μm
Pulse width	< 10 fs
Repetition	30 Hz

Table 5.1: Light source parameter of SACLA.

5.3.3 Expected total gain on $g_{a\gamma\gamma}$

Gain factors of the future experiment at SACLA is summarized in Tab. 5.2. The total gain on $g_{a\gamma\gamma}$ is expected to be the product of them. This gives an improvement by a factor of 5.57 from the present limit of Eq. (4.8).

Parameter	gain on $g_{a\gamma\gamma}$
Total field length	2.00
Repetition field	1.14
Repetition	1.19
SACLA	2.05
Total	5.57

Table 5.2: Expected gain factors of the future experiment at SACLA

Chapter 6

Conclusion

The first X-ray LSW search for axion-like particles (ALPs) using strong pulsed magnets has been reported in this thesis. A transportable magnet system for high-repetition use has dedicatedly been developed. The experiment has been carried out at the BL19LXU beamline of SPring-8, which produces the world's strongest DC X-ray beams. During two days of net run time, four magnets are operated at a mean peak field of 8.3 T and 5.7 T (the first and the second pulse, respectively) with a pulse repetition of about 0.2 Hz. After a total of 27,676 pulses, no signal events are observed. A new limit on ALP-two-photon coupling constant $g_{a\gamma\gamma}$ is obtained as

$$g_{a\gamma\gamma} < 2.51 \times 10^{-4}\ \mathrm{GeV}^{-1}$$

below$\sim$ 0.1 eV at 95% C.L. This is the most stringent LSW limit around 0.1 eV. This experiment also demonstrates the feasibility of using pulsed magnets for X-ray LSW search. With the combination of strong pulsed beam from XFEL SACLA, the sensitivity on $g_{a\gamma\gamma}$ will be further improved in the future experiment.

Acknowledgements

First, I would like to express my sincere gratitude to my supervisor Prof. Shoji Asai (The University of Tokyo) and my former supervisor Prof. Tomio Kobayashi (KEK) for providing me with opportunity of this work. I was supported by their continuous encouragement.

I also wish to express my great appreciation to Prof. Toshio Namba (ICEPP, The University of Tokyo) for guiding this work in the right direction with his experience. His outstanding suggestions and technical advice supported me and this work from the beginning.

My special thanks go to Dr Takayuki Yamazaki (ICEPP, The University of Tokyo). It would not have been possible to perform this work without his support. Most of this work has been carried out with his excellent cooperation.

I would also like to thank Mr. Tomohiro Yamaji for his support at the experiment.

The range of this work spreads to many regions other than particle physics. We would like to express our gratitude to Prof. Koichi Kindo, Dr. Akira Matsuo, and Dr. Takashi Kawaguchi (ISSP, The University of Tokyo) for providing technical advice on the fabrication of magnets. We also wish to express our great appreciation to Prof. Hiroyuki Nojiri and Prof. Yasuo Narumi (IMR, Tohoku University) for guiding the design of the capacitor bank.

Our special thanks go to the BL19LXU beamline manager Prof. Kenji Tamasaku (RIKEN, SPring-8) and the former beamline manager Prof. Yoshihito Tanaka (University of Hyogo) for their technical support. We would also like to express our gratitude to Prof. Yuichi Inubushi, Prof. Kei Sawada, Prof. Makina Yabashi, and Prof. Tetsuya Ishikawa for their useful discussions.

At this point, I would like to thank all the staffs and students of International Center for Elementary Particle Physics (ICEPP) at The University of Tokyo.

Finally, I would like to thank my family, who always support me behind the scenes.

Bibliography

[1] C. A. Baker et al., Phys. Rev. Lett. **97**, 131801 (2006).

[2] S. Weinberg, Phys. Rev. Lett. **40**, 223 (1978).

[3] F. Wilczek, Phys. Rev. Lett. **40**, 279 (1978).

[4] R. D. Peccei and H. R. Quinn, Phys. Rev. Lett. **38**, 1440 (1977).

[5] R. D. Peccei and H. R. Quinn, Phys. Rev. D **16**, 1791 (1977).

[6] W. A. Bardeen et al., Phys. Lett. B **76**, 580 (1978).

[7] W. A. Bardeen et al., Nucl. Phys. B **279**, 401 (1987).

[8] J. E. Kim, Phys. Rev. Lett. **43**, 103 (1979).

[9] M. A. Shifman et al., Nucl. Phys. B **166**, 493 (1980).

[10] M. Dine et al., Phys. Lett. B **104**, 199 (1981).

[11] A. R. Zhitnitsky, Sov. J Nucl. Phys. **31**, 260 (1980).

[12] L. Covi et al., Phys. Rev. Lett **82**, 4180 (1999).

[13] P. Svrcek and E. Witten, J. High Energy Phys. **06**, 051 (2006).

[14] M. Cicoli et al., J. High Energy Phys. **12**, 146 (2012).

[15] K. A. Meissner and H. Nicolai, Phys. Lett. B **660**, 200 (2000).

[16] P. Sikivie, Phys. Rev. Lett. **51**, 1415 (1983).

[17] D. M. Lazarus et al., Phys. Rev. Lett. **69**, 2333 (1992).

[18] Y. Inoue et al., Phys. Lett. B **536**, 18 (2002).

[19] M. Arik et al., Phys. Rev. Lett. **112**, 091302 (2014).

[20] M. Arik et al., J. Cosmol. Astropart. Phys. **02**, 008 (2009).

[21] I. Avignone et al., Phys. Rev. Lett. **81**, 5068 (1998).

[22] A. Morales et al., Astropart. Phys. **16**, 325 (2002).

[23] R. Bernabei et al., Phys. Lett. B **515**, 6 (2001).

[24] Z. Ahmed et al., Phys. Rev. Lett. **103**, 141802 (2009).

[25] E. Armengaud et al., JCAP **11**, 067 (2013).

[26] S. DePanfilis et al., Phys. Rev. Lett. **59**, 839 (1987).

[27] S. J. Asztalos et al., Phys. Rev. Lett. **104**, 041301 (2010).

[28] W. U. Wuensch et al., Phys. Rev. D **40**, 3153 (1989).

[29] C. Hagmann et al., Phys. Rev. D **42**, 1297 (1990).

[30] L. B. Okun et al., Sov. Phys. JETP **56**, 502 (1982).

[31] J. Redondo and A. Ringwald, Comtemp. Phys. **52**, 211 (2011).

[32] G. Raffelt and L. Stodolsky, Phys. Rev. D **37**, 1237 (1988).

[33] S. A. Adler et al., Ann. Phys. **323**, 2851 (2008).

[34] P. Arias et al., Phys. Rev. D **82**, 115018 (2010).

[35] A. A. Anselm et al., Yad. Fiz. **42**, 1480 (1985).

[36] K. Van Bibber et al., Phys, Rev. Lett **59**, 759 (1987).

[37] K. Ehret et al., Phys. Lett. B **689**, 149 (2010).

[38] R. Ballou et al., Phys. Rev. D **92**, 092002 (2015).

[39] M. Betz et al., Phys. Rev. D **88**, 075014 (2013).

[40] R. Battesti et al., Phys. Rev. Lett. **105**, 250405 (2010).

[41] G. Ruoso et al., Z. Phys. C **56**, 505 (1992).

[42] R. Cameron et al., Phys, Rev. D **47**, 3707 (1993).

[43] C. Robilliard et al., Phys, Rev. Lett. **99**, 190403 (2007).

[44] M. Fouche et al., Phys, Rev. D **78**, 032013 (2008).

[45] A. S. Chou et al., Phys, Rev. Lett. **100**, 080402 (2008).

[46] A. Afanasev et al., Phys, Rev. Lett. **101**, 120401 (2008).

[47] A. Afanasev et al., Phys, Lett. B **679**, 317 (2009).

[48] K. Ehret et al., Mucl. Instrum. Meth. A **612**, 83 (2009).

[49] P. Pugnat et al., Phys. Rev. D **78**, 092003 (2008).

[50] P. Arias et al., J. Cosmol. Astropart. Phys. **06**, 013 (2012).

[51] A. Ringwald et al., Phys. Dark. Univ. **1**, 116 (2012).

[52] M. Meyer et al., Phys. Rev. D **87**, 035027 (2013).

[53] M. M. M. Bertolami et al., J. Cosmol. Astropart. Phys. **10**, 069 (2014).

[54] M. Cicoli et al., Phys. Rev. D **10**, 023540 (2014).

[55] R. Holman et al., Phys. Lett. B **282**, 132 (1992).

[56] M. Kamionkowski and J. March-Russell, Phys. Lett. B **282**, 137 (1992).

[57] S. M. Barr and D. Seckel, Phys. Rev. D **46**, 539 (1992).

[58] E. Masso and J. Redondo, JCAP **0509**, 015 (2005).

[59] P. Jain and S. Mandal, Int.J.Mod.Phys.D **15**, 2005 (2006).

[60] E. Masso and J. Redondo, Phys. Rev. Lett. **97**, 051802 (2006).

[61] L. B. Okun, Sov. Phys. JTEP **56**, 502 (1982).

[62] B. Holdom, Phys. Lett. B **166**, 196 (1986).

[63] E. Zavattini et al., Phys. Rev. Lett. **96**, 110406 (2006).

[64] K. Zoutas et al., arXiv:1003.2181 (2010).

[65] G. G. Raffelt, Lect. Notes Phys. **741**, 51 (2008).

[66] H. Schlattl et al., Astropart. Phys. **10**, 353 (1999).

[67] R. Rabadan et al., Phys. Rev. Lett. **96**, 110407 (2006).

[68] A. G. Dias and G. Lugones, Phys. Lett. B **673**, 101 (2009).

[69] IMSL web page, `https://www.issp.u-tokyo.ac.jp/maincontents/organization/labs/kindo_group_en.html`.

[70] R. Bahre et al., JINST **8**, T09001 (2013).

[71] F. Herlach, Rep. Prog. Phys. **62**, 859 (1999).

[72] Kindo's laboratory, `http://kindo.issp.u-tokyo.ac.jp/e/index.htm`.

[73] S. Batut et al., IEEE Trans. Appl. Supercond. **18**, 600 (2008).

[74] P. Astier et al., Phys. Lett. B **479**, 371 (2000).

[75] G. G. Raffelt, Phys. Rev. D **37**, 1356 (1988).